# Shortcut Model to Evaluate the Performance of Preferential Crystallization for Conglomerates Forming Chiral Systems

**Dissertation**
zur Erlangung des akademischen Grades

**Doktoringenieur**
**(Dr.-Ing.)**

von M.Sc., Shashank Bhandari
geb. am 12 September 1989 in Mumbai

genehmigt durch die Fakultät für Verfahrens- und Systemtechnik der Otto-von-Guericke-Universität Magdeburg

Gutachter:

Prof. Dr.-Ing. Andreas Seidel-Morgenstern

Prof. Dr.-Ing. Achim Kienle

Prof. Dr. Joop Ter Horst

Promotionskolloquium am 26 July 2024

# Abstract

Preferential Crystallization (PC) is an important method for separating enantiomers of chiral molecules that form conglomerates. The process operates within narrow metastable zone of the specific phase diagrams. One of the challenges is the lack of straightforward models to estimate the productivity of PC and compare it with other resolution techniques. Addressing this gap, we introduce a simple effective shortcut model (SCM) designed to depict the key characteristics of batch-operated PC. This model utilizes simple ordinary differential equations derived from the mass balances of the two enantiomers and the solvent for both liquid and solid phases. A notable distinction of the SCM from more detailed population balance models is the assumption of uniform crystal sizes for the two enantiomers, which grow uniformly starting from prespecified initial values. The primary aim of the SCM is to accurately represent the exploitable production phase of the PC process characterized by very high product purity. Beyond this phase, the reliability of the model rapidly decreases.

To demonstrate the parameterization and application of the SCM, we initially analyse theoretical transients generated from the more comprehensive detailed Population Balance Model (PBM) for the separation of DL-threonine enantiomers. This is followed by exploiting data gained in an independent experimental study for the enantiomers of asparagine monohydrate. The SCM is found to be a novel and valuable tool for rapidly assessing the productivity of PC in order to resolve enantiomers of conglomerate forming chiral systems.

Subsequently the SCM is reformulated in a dimensionless form and extended to describe continuous PC operations. Characteristic dimensionless quantities such as Damköhler and Bodenstein number are used to evaluate the effects of specific thermodynamic and kinetic parameters, and to identify optimal operating conditions. The sensitivity of the key model parameters for continuous PC process is explored through systematic simulation studies, which provide valuable insight and support process optimization.

Finally, we also address a significant limitation of PC, namely that the maximum yield is restricted to 50%. By incorporating a racemization reaction and a recycling step into the crystallization process, we explore ways to utilize the counter enantiomer as well. The SCM is extended to include a kinetic model for enzymatically catalysed racemization reactions, using parameters characterizing the resolution of asparagine monohydrate enantiomers and the racemization rate facilitated by an amino acid racemase. This theoretical study emphasizes the importance of optimizing the introduced characteristic stop time to maximize process productivity.

This work not only introduces a simple and practical tool for describing PC processes. By contributing to an improved understanding of continuous operations and other novel variants of PC, it offers pathways for more efficient and productive separation of chiral enantiomers.

# Kurzfassung

Die „Bevorzugte Kristallisation (englisch: Preferential Crystallization, PC)“ ist eine wichtige Methode zur Trennung von Enantiomeren chiraler Moleküle, die Konglomerate bilden. Der Prozess arbeitet innerhalb einer engen metastabilen Zone der spezifischen Phasendiagramme. Eine der Herausforderungen auf diesem Gebiet ist der Mangel an einfachen Modellen zur Abschätzung der Produktivität der PC zum Vergleich mit anderen Trennverfahren. Um diese Lücke zu schließen, stellen wir ein einfaches, aber effektives Shortcut Model (SCM) vor, das zunächst die wichtigsten Merkmale der im Batch-Betrieb durchgeführten PC abbildet. Dieses Modell verwendet gewöhnliche Differentialgleichungen, die sich aus der Massenbilanzen der Enantiomeren und des Lösungsmittels sowohl in der flüssigen als auch in der festen Phase ergeben. Ein wesentlicher Unterschied zwischen dem SCM und detaillierteren Populationsbilanzmodellen ist die Annahme einer einheitlichen Kristallgröße für jedes Enantiomer, die ausgehend von vordefinierten Anfangswerten gleichmäßig wächst. Das Hauptziel des SCM besteht darin, die Produktionsphase des Batch-Prozesses genau zu beschreiben und sicherzustellen, dass hohe Produktreinheit erzielt werden. Es ist bekannt, dass die Genauigkeit der Vorhersagen des Modells nach dieser Phase abnehmen kann.

Um die praktische Anwendung und Parametrisierung des SCM zu demonstrieren, analysieren wir zunächst theoretische Transienten, die mit dem umfassenderen Modell der Populationsgleichgewichtsgleichung (PBE) generiert wurden, und konzentrieren uns dabei auf die Trennung von DL-Threonin-Enantiomeren. Es folgt eine experimentelle Studie zu den Enantiomeren von Asparaginmonohydrat, die die Anwendbarkeit des SCM weiter validiert. Das SCM erweist sich als neuartiges und wertvolles Werkzeug zur schnellen Bewertung der Produktivität vder PC und verbessert die Möglichkeit der Trennung von Enantiomeren in chiralen Systemen, die Konglomerate bilden.

ImAnschluss wird das SCM in einer dimensionslosen Format erneut formuliert und seine Anwendung auf kontinuierliche PC-Operationen erweitert. Charakteristische dimensionslose Parameter wie die Damköhler- und die Bodenstein-Zahl werden verwendet, um die Auswirkungen bestimmter thermodynamischer und kinetischer Parameter zu bewerten und optimale Betriebsbedingungen zu ermitteln. Die Empfindlichkeit des kontinuierlichen PC-Prozesses gegenüber den wichtigsten Modellparametern wird mittels systematischer Simulationsstudien untersucht. Die erzielten Erkenntnisse sind wertvoll für eine Prozessoptimierung.

Diese Arbeit befasst sich abschliessend auch mit einer wichtigen Einschränkung der PC, nämlich der Beschränkung der maximalen Ausbeute auf 50 %. Durch die Einbeziehung einer Racemisierungsreaktion und eines Recycling-Schrittes besteht die Möglichkeiten zur

vollständigen Ausnutzung des Gegen-Enantiomers. Das SCM wird deshalb um ein kinetisches Modell für die enzymatisch katalysierte Racemisierungsreaktion erweitert, wobei Parameter verwendet werden, die die Auflösung von Asparaginmonohydrat-Enantiomeren und die durch eine Aminosäure-Racemase geförderte Racemisierung charakterisieren. Diese theoretische Studie unterstreicht auch die Bedeutung der Optimierung der eingeführten charaketistischen Stoppzeit für die Maximierung der Prozessproduktivität.

Diese Arbeit stellt ein praktisches Werkzeug für dies Auslegung von PC-Prozessen vorträgt zu einem verbesserten Verständnis von kontinuierlichen Operationen und anderen neuen Varianten der PC bei und bietet zeigt neue Weg für eine effizientere und produktivere Trennung chiraler Enantiomere auf.

# Collaborations and research publications

This Ph.D. project was embedded in a larger research project on Continuous Resolution (CORE) and Deracemization of Chiral Compounds by Crystallization within the group for Physical and Chemical Foundations of Process Engineering research at the Max Planck Institute for Dynamics of Complex Technical Systems Magdeburg. Funded by the European Union a Marie Skłodowska-Curie Innovative Training Network (ITN) brought together 8 beneficiary partners and 6 associate partners from 6 European countries. The research objective of the "CORE Network" was to jointly construct an Industrial Toolbox on Continuous Resolution that provides next generation tools, approaches and methods to industry for the development of continuous resolution processes.

This thesis work is of theoretical nature. The kinetic and thermodynamic data, essential for developing the model described in this thesis, were available from preliminary research conducted at MPI Magdeburg by Matthias Eicke (Eicke 2016). Further preliminary experiments were performed by Thiane Carnero (Carneiro 2021) to estimate model parameters for a second system and operating regime.

This Ph.D. thesis was further supported by the International Max Planck Research School for Advanced Methods in Process Systems Engineering (IMPRS ProEng).

A summary of the outcome of this research work is:

**Journal Publications:**

1. Carneiro, Thiane, Shashank Bhandari, Erik Temmel, Heike Lorenz, and Andreas Seidel-Morgenstern. 2019. "Shortcut Model for Describing Isothermal Batch Preferential Crystallization of Conglomerates and Estimating the Productivity." *Crystal Growth & Design* 19 (9): 5189–5203. https://doi.org/10.1021/acs.cgd.9b00592.

2. Bhandari, Shashank, Thiane Carneiro, Heike Lorenz, and Andreas Seidel-Morgenstern. 2022. "Shortcut Model for Batch Preferential Crystallization Coupled with Racemization for Conglomerate-Forming Chiral Systems." *Crystal Growth and Design* 22 (7): 4094–4104.https://doi.org/10.1021/acs.cgd.1c01473/asset/images/large/cg1c01473_0010.

3. Bhandari, S., Lorenz, H., & Seidel-Morgenstern, A. (2024). Shortcut model to evaluate the performance of continuous preferential crystallization for conglomerates forming chiral systems. Chemical Engineering Science, 299, 120539. https://doi.org/10.1016/j.ces.2024.120539

**Conferences**

1. Bhandari, Shashank, T. Carneiro, E. Temmel, H. Lorenz, A. Seidel-Morgenstern (2019) Modeling Batch Preferential Crystallization for Conglomerates Forming Systems using Shortcut Models. 12th European Congress of Chemical Engineering (ECCE12), 15-19 September 2019, Florence, Italy (Oral Presentation)

2. Bhandari, S., Cascella, F., Lorenz, H., & Seidel-Morgenstern, A. (2020). Preferential Crystallization for Conglomerate Forming Systems: Experiments and Modelling. Poster presented at 4th Indo-German workshop on "Advances in Materials, Reactions & Separation Processes". Berlin, Germany. 24.-26.2.2020. (Oral Presentation)

3. Bhandari, S., Carneiro, T., Lorenz, H., & Seidel-Morgenstern, A. (2020). Modeling, Simulation and design strategies to efficiently apply preferential crystallization in a continuous process. Talk presented at 2020 Virtual AIChE Annual Meeting, virtually. 16.-20.11.2020. (Oral Presentation)

4. Bhandari, Shashank, H. Lorenz, A. Seidel-Morgenstern (2021). Modeling and Simulation for Continuous Preferential Crystallization Using Dimensionless Shortcut Model. 21st International Symposium in Industrial Crystallization (ISIC 21), virtually, 30 Aug - 2 September 2021. (Oral Presentation)

5. Bhandari, Shashank , A. Seidel-Morgerstern (2017). Continuous Crystallization Process Design Strategies Summer School on Chiral Crystallization, Resolution & Deracemization, Nijmegen, The Netherlands, July 3-6, 2017 (Poster)

6. Bhandari, Shashank , S. Qamar, A. Seidel-Morgenstern (2018). Cyclic Batch Preferential Crystallization for Conglomerates and Racemic Compounds. 25th International Workshop on Industrial Crystallization (BIWIC), 6-7 September 2018, University of Rouen, France (Poster)

7. Bhandari, Shashank , S. Qamar, A. Seidel-Morgenstern (2018). Cyclic Batch Preferential Crystallization for Conglomerates and Racemic Compounds. 25th International Workshop on Industrial Crystallization (BIWIC), 6-7 September 2018, University of Rouen, France (Poster)

# Table of Contents

# 1. Introduction

## 1.1. Importance of enantiomers: relevance to life sciences

The question of the homochirality in biological molecules has intrigued the scientific community for centuries. It is still arguable as to why nature has a tendency to favor one of the spatial arrangements as a building block to create life on earth (Blackmond 2010; Cintas 2002). Ever since Pasteur's meticulous separation of the two enantiomeric crystals of tartaric acid salt in 1848, chirality has been considered an essential criterion to explain the origin of life (Meierhenrich 2008b, 2008a; Pasteur 1848).

Enantiomers are a pair of stereoisomers that are chiral and form a non-superimposable mirror image of each other. The two enantiomers of the same chiral compound exhibit identical physical and chemical properties. To distinguish between them, a plane-polarized light is passed to a solution of a chiral molecule and as a result, the plane of polarization of the emerging light is rotated comparative to the initial plane of the light. The classical notation to identify the enantiomer that rotates the light clockwise is by d or (+) (dextrorotary) and the enantiomer that rotates anticlockwise is by l or (-) (levorotary). A 50:50 mixture of both the enantiomers does not rotate the light plane and are called a racemate or racemic mixture (Coquerel 2007; Jacques, Collet, and Wilen 1994).

The two enantiomers of the same chiral molecule often demonstrate different effects when it interacts with the same biological environments. It is evident that in many cases only one enantiomer shows the desired physiological effect whereas the other enantiomer has no or may exhibit side-effects (Beckett 1991). A well-known example of enantiomer related toxicity is the R- and S- enantiomers of Penicillamine. The S-enantiomer of Penicillamine is used as an anti-arthritic while R-enantiomer is toxic. Another example is Ibuprofen as a pain killer in its R-enantiomer and S-enantiomer is inactive (J.K. Aronson 2010; Mwamwitwa et al. 2020). Due to the different effects of R- and S- forms, it becomes important to separate the desired enantiomer from its racemate before using it as a medicine. This led to a significant increase in the demand for the production of single enantiomers. According to a report published in 2004, worldwide annual distribution of enantiopure drug have increased from 26% in 1983 to 55% in 2002, for racemates it has been decreased form 37% in 1983 to around 6% in 2002 and for achiral it has been around the same from 37% in 1983 to 39% in 2002 (Caner et al. 2004). Regulatory control on the investigation of the chiral active substance during the development of new stereoisomeric drugs began in the US by FDA in 1992 followed by European Union in 1994 (Bonner 1995; Caner et al. 2004).

Nowadays, most of the chiral drugs are sold in their enantiopure form (Caner et al. 2004). However, efficient production of them is often a critical task and can either be manufactured by asymmetric synthesis of only one enantiomer or by resolution of a racemic mixture using various separation techniques that are discussed in the next section. Despite major breakthroughs in asymmetric synthesis, it is still a challenge for the chemists to synthesize an enantiopure drug. Thus, preparation of a racemic mixture followed by a resolution technique is widely used in the process industries (Mullin 2001).

## 1.2. Enantiomer separation techniques

A variety of separation techniques are used in the industries for the resolution of racemates such as chromatography (Juza, Mazzotti, and Morbidelli 2000; Lorenz, Sheehan, and Seidel-Morgenstern 2001; Wrzosek et al. 2016), membrane processes (Afonso and Crespo 2004; Xie, Chu, and Deng 2008) and numerous variants of crystallization (Coquerel 2007; ter Horst, Schmidt, and Ulrich 2015; Lorenz and Seidel-Morgenstern 2014; Majumder and Nagy 2017). In the last couple of decades, there have been tremendous advances in each of these processes for the resolution of racemic mixture. Each process has its own merits and demerits based on the compound of interest.

### 1.2.1. Enantioselective chromatography

One of the most efficient techniques for the resolution is column chromatography with a solid stationary phase (Bhushan and Martens 2010). It provides a wide potential to regulate both the liquid mobile phase and the solid stationary phase to fit the demands of the separation process. An important question using chromatography for enantioselective separation is which of the two phases should be chiral. Numerous studies have been made for the development of the chiral mobile phases and revealed that the chiral agents are not easy to recycle, recover and have relatively lower capacities of chromatography column than the chiral stationary phase (CSP). Therefore, chiral mobile phase is not a suitable candidate for enantioselective liquid chromatography (Subramanian 2007). Nowadays, there are a large amount of commercially available CSPs in the market that can resolve a spectrum of racemic mixtures.

Nowadays, enantioselective chromatography is extensively used in industries for the resolution of racemates (Cox 2005). However, chromatographic processes on a large scale are very expensive. Therefore, it often requires efficient process design and optimization to ensure high productivities. In the last couple of decades, one of the major advances was the development of the simulated moving bed process. It provides a significant improvement in productivities (Negawa and Shoji 1992). Although chromatographic processes are versatile and are capable of resolving any complex separation process, it requires additional steps for enrichment. In other separation techniques such as membrane processes, the product is

obtained in the liquid phase which also requires additional steps for purification (Afonso and Crespo 2004; Xie et al. 2008; Yoshikawa and Higuchi 2013).

### 1.2.2. Purification of enantiomers via crystallization

An impressive more recent advancement in chiral purification is deracemization through Viedma ripening (Viedma 2005). In this process, a racemate of enantiomeric crystals are continuously grinded while in contact with a saturated solution resulting in a single enantiomeric form of solids. The two prerequisites of this process are that the compound should crystallize as conglomerates and the compound should be racializable in the liquid phase without forming any by-products. The deracemization rate is governed by growth, dissolution and racemization rates. It's a simple process and received a lot of attention because of its capability to achieve 100% yield. However, the process time for this technique is relatively very slow compare to the other resolution techniques for enantiomers and therefore not well-suited for large scale production. In the last few years, many applications of Viedma ripening have been developed to enable it to be used on a large industrial production. For example, "deracemization via temperature cycling" is an application of Viedma ripening in which full deracemization of the solid phase is attained using heating-cooling cycles instead of continuous grinding of the suspension (Intaraboonrod, Lerdwiriyanupap, et al. 2020; Li et al. 2016; Sögütoglu et al. 2015; Steendam and Ter Horst 2018; Suwannasang et al. 2013; Xiouras et al. 2017). The faster rate of temperature cycles corresponds to shorter process times.

Enantioselective crystallization is an easy, robust and a powerful separation technique for the resolution of racemates. The product is directly separated in a solid phase which eliminates the requirement of additional enrichment steps. One of the widely used crystallization-based resolution techniques is known as classical resolution (Murakami 2006). In this method, enantiomers are chemically reacted with an enantiopure resolving agent to form diastereomeric salts. The two resulting salts possess different solubility and thus can be easily separated by a crystallization process. The challenge in this method is to identify a suitable chiral resolving agent for the reaction (Simon et al. 2019).

Another crystallization technique that is used in industries to resolve racemates is preferential crystallization (PC) (Coquerel 2007). PC will be in the focus of this work. It is a kinetically driven process suitable to separate conglomerates (see chapter 2). It only requires enantiopure crystals of the desired enantiomer to preferentially crystallize the product from the solution of a racemic mixture. However, this method has a serious limitation of the spontaneous nucleation of the counter enantiomer. This may happen due to prolonged batch times where the supersaturation of the counter enantiomer in the solution is more than that of preferred enantiomer (Jacques et al. 1994; Levilain and Coquerel 2010). To overcome this problem, several researches have been conducted. For instance, using coupled preferential

crystallization (Elsner, Ziomek, and Seidel-Morgenstern 2007), by integrating racemization of liquid phase to PC (Oketani et al. 2019a) or by changing the mode from batch to continuous (Galan et al. 2015). An important challenge of the crystallization-based separation of the enantiomers is also due to different solid-liquid equilibria of the ternary system including the two enantiomers and a solvent. Majority of the ternary systems belong to racemic compound forming system which does not allow direct separation of the enantiomers by crystallization (Levilain and Coquerel 2010).

## 1.3. Objective and outline

The objective of this work is to develop a simple Shortcut Model (SCM) for the quick estimation of the key performance indicators (KPIs) of PC process, such as, productivity, yield and purity of the preferential crystallization process. It involves a systematic theoretical investigation of process strategies to obtain pure crystals of target enantiomer from its racemate. Alternative to the detailed models such as population balance equations, there is a requirement of the simpler tools to rapidly access the KPIs. In this study, the evolution of the model from batch towards continuous process is demonstrated and an analogy of chemical reaction engineering and crystallization process is discussed to describe the dimensionless form of shortcut model. Building upon the foundations, integration of racemization step with PC process has also been investigated using SCM.

The structure of the following sections of this study is systematically arranged as follow:

In **chapter 2**, we explore into the basic elements of crystallization. It provides a general discussion on the thermodynamic and kinetic aspects of crystallization, which are fundamental to understanding the entire process. This includes an investigation of various forms of solid-liquid equilibria and kinetic phenomenon crucial to know how a substance transition from a liquid to a solid state. Additionally, the chapter concludes with a detailed description on PC process and concise summary of alternative methods for conducting PC.

In **chapter 3**, we focus on the technical aspects of our study, particularly the Population Balance Model (PBM) that is widely used to model the PC process. It allows us to simulate the changes in population of particles over time, considering aspects such as nucleation, growth, and aggregation. Furthermore, the chapter advances by detailing the methodology used for calculating the driving forces in PC using Ternary Phase Diagrams. This chapter also details the numerical solutions we've utilized for solving the resulting PBEs in this work.

**Chapter 4** of thesis introduces the Shortcut Model (SCM) developed in the course of this work. It is suggested as a tool for rapidly estimating the productivity of PC process. The initial section of this chapter explains the foundational principles behind the development of this model, along with the assumptions that support it. This offers a comprehensive understanding of the

model's theoretical basis. Following this, we present the specific equations that describes the model. These equations are crucial for understanding how the SCM functions and predicts the outcomes of the PC process. The chapter continues with a detailed procedure for quantifying experiments and process evaluations. This includes key performance indicators such as productivity, yield, and purity, which are essential for evaluating the efficiency of PC process. In the next section, to further develop the SCM, we extend its application to accurately depict the continuous PC at steady state. This advancement leverages key concepts and analogies from Chemical Reaction Engineering (CRE), particularly focusing on the transition of the model from batch to continuous operations. A significant aspect of this extension is the incorporation of instructive dimensionless numbers, which are widely used in CRE to generalize and simplify complex processes. The integration of these dimensionless numbers aims to make the SCM more suitable for qualitative analysis of continuous PC processes carried out in tubular crystallizers. In the last section of this chapter, we expand the applicability of SCM to a batch PC coupled with enzymatic racemization in two different process variants. We also demonstrate the flexibility of the SCM by evaluating a cascade of tank crystallizers, which offer improvements over traditional single-tank operation.

In **chapter 5**, we summarize the thermodynamic and kinetic data used to estimate the SCM model parameters applied in various case studies.

**Chapter 6** contains demonstrations of the SCM for 3 different scenarios. In the first section, we propose a methodology for applying the SCM and for estimating its parameters. To demonstrate the practical application of the model, the results of chapter 5 are used to parameterize the SCM and estimate productivity for batch operation based on the strategy outlined in the chapter 4. In the next section we demonstrate six sensitivity studies of continuous PC in a tubular crystallizer using dimensionless form of SCM. Finally, the last section of this chapter shows predictions of SCM for batch PC coupled with enzymatic racemization in two different process variants. This includes a discussion on the simulation results concerning the productivity and yield for resolving asparagine monohydrate enantiomers. By providing these real-world applications and outcomes, the chapter aims to show the flexibility of the SCM in modelling different variants of PC processes.

**Chapter 7** concludes and provides an outlook of this work.

# 2. Principle of Crystallization

Crystallization is one of the oldest unit operations in the field of chemical engineering. For instance, the process of manufacturing sodium chloride through crystallization has been practiced since the earliest days of human civilization. This longstanding history underscores the enduring importance and significance of crystallization as a fundamental technique in chemical engineering (Mullin 2001). At present, crystallization process is used for separating and purifying a diverse range of materials. It involves a phase change where a crystalline substance is obtained from a solution. A solution is essentially a mixture composed of two or more substances that combine to form a uniform and homogeneous single phase. In common usage, the term "solution" typically refers to a liquid mixture comprising a solvent (a liquid) and a solute (a solid) under specific conditions of interest (Myerson 2002).

Crystallization proves to be an effective method for separating enantiomers, which are molecules with mirror-image structures. In cases where the enantiomers crystallize as conglomerates (distinct crystals), their separation can be achieved through several techniques such as preferential crystallization or deracemization techniques.

This chapter serves as a foundational introduction to the key concepts explored in the thesis. It begins by elucidating the thermodynamic properties of chiral compounds, including aspects such as supersaturation, the width of the metastable zone, and phase diagrams. In this sequence of discussions, we delve into the key kinetic aspects of crystallization, particularly focusing on the roles played by nucleation and growth kinetics. We then explore the fundamental principles of preferential crystallization, highlighting the two modes of operation; batch and continuous. Following that, we provide a concise overview of the integration of preferential crystallization with racemization technique.

## 2.1. Thermodynamics of crystallization

Crystallization, a process that converts a fluid (liquid or gas) into a solid crystalline state, is fundamentally rooted in thermodynamic principles. Central to understanding crystallization is the concept of supersaturation, which dictates the driving force for crystallization. The metastable zone is an essential region of understanding in crystallization kinetics, while phase diagrams provide insight into the thermodynamic landscape of the system. In this section, we delve into these concepts and explore their interrelation.

### 2.1.1. Supersaturation

Supersaturation represents the driving force for crystallization. It is defined as the state in which the concentration of solute in a solution exceeds its equilibrium or saturation concentration. Mathematically, the degree of supersaturation ($S_i$) can be defined as:

$$S_i = \frac{c_i}{c_{i,sat}} \qquad i \in \{1,2\} \tag{2.1}$$

where $c_i$ is the actual concentration of the solute and $c_{i,sat}$ is its saturation concentration (Myerson 2002).

Analogously, the following alternative mass-based definition of the supersaturation can be defined:

$$S_{m,i} = \frac{w_i}{w_{sat,i}(w_1, w_2)} \qquad i \in \{1,2\} \tag{2.2}$$

In this study, when discussing enantiomers, the preferred enantiomer is labeled as $i$ = 1 and the unwanted one as $i$ = 2. The solvent is represented by $i$ = 3. The term $w_{sat,i}$ refers to the equilibrium mass fraction in the liquid phase. A system with $S_{m,i}$< 1 is not saturated, while a system with $S_{m,i}$> 1 is supersaturated. Concentrations are given as weight fractions (eq. 2.3) based on the total liquid phase mass $m_{tot}$, which is the sum of $m_1$, $m_2$, and $m_3$.

$$w_i = \frac{m_i}{m_1 + m_2 + m_3} = \frac{m_i}{m_{tot}} \qquad i \in \{1,2\} \tag{2.3}$$

Crystallization is driven by supersaturation. In its essence, the greater the degree of supersaturation, the stronger the driving force for crystal nucleation and growth. Supersaturation defines the thermodynamic potential for crystallization and directs both the kinetics and thermodynamics of the process.

For crystallization purposes, supersaturated solutions are often achieved through:

- Cooling Crystallization: This involves preparing a solution saturated at a higher temperature and then cooling it down. As the temperature decreases, the solubility of the solute often decreases, leading to supersaturation.

- Evaporative Crystallization: In this method, the solvent is evaporated from a saturated solution, increasing the solute concentration beyond saturation.

- Reactive Crystallization: Supersaturation is achieved when a chemical reaction produces a product in a solution that exceeds its saturation concentration (Mullin 2001).

- Antisolvent: Introducing an anti-solvent, leads to decreased solute solubility, resulting in crystallization.

The degree of supersaturation affects the two primary stages of crystallization. At high supersaturation, nucleation rates are high, leading to the formation of a large number of small crystals. This is because the solution has a strong driving force to revert to its stable state and will form numerous nuclei spontaneously (Kashchiev 2000). Once nuclei are formed, they grow by the addition of solute molecules. The growth rate often increases with increasing supersaturation but can become limited by mass transfer or kinetic factors at very high supersaturation levels (Randolph and Larson 1988).

While supersaturation is necessary for crystallization, there is a risk associated with it. If the degree of supersaturation is too high, it might lead to undesirable outcomes. High supersaturation can cause existing crystals to produce new nuclei (secondary nucleation), leading to a large number of small crystals rather than fewer larger ones. Some compounds might not crystallize but instead form an amorphous or oily phase if the supersaturation is exceedingly high (Oiling Out). To avoid these challenges, crystallization processes aim to maintain the solution within a desired "metastable zone" where the solution is supersaturated enough to drive crystallization but not so much that it leads to uncontrolled nucleation or oiling out. Therefore, for consistent and predictable crystallization, seed crystals can be introduced to a supersaturated solution to control nucleation. These seeds provide a platform for crystal growth, reducing the chances of uncontrolled spontaneous nucleation. Another technique is by precisely controlling the rate of cooling or solvent evaporation, one can manage the rate at which supersaturation is achieved, allowing for better control over nucleation and growth (Myerson 2002).

### 2.1.2. Metastable Zone

The metastable zone is a region between the solubility curve and the supersaturation limit at which spontaneous nucleation can occur. Within this zone, the solution is supersaturated but does not spontaneously crystallize. This zone is significant for industrial crystallization since it determines the conditions under which controlled nucleation can be achieved.

The width of the metastable zone (MZW) can be influenced by several factors, including impurities, cooling rate, agitation, and the history of the solution. The MZW is typically narrower at higher supersaturation levels (Mullin 2001).

The metastable zone can be very well described with the help of a binary solubility diagram illustrated in figure 2.1. The diagram displays the concentrations at which two components (a solute and a solvent) are in equilibrium as a function of temperature. The y-axis typically represents the concentration of the solute, and the x-axis represents temperature.

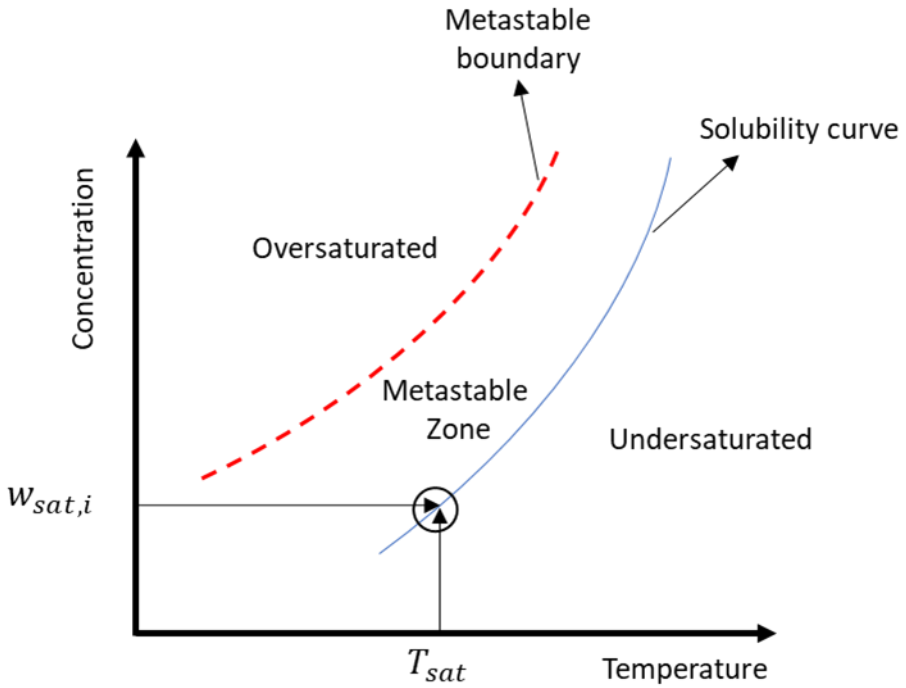


**Figure 2.1**. The diagram shows the changes in solubility with temperature, represented by the solubility curve for component $i$ in a specific solvent. This curve indicates the saturation concentration $w_{sat,i}$ based on temperature $T_{sat}$. There's another limit called the metastable boundary where nucleation can spontaneously happen. Between this limit and the solubility curve lies the metastable zone (MZ).

The diagram is composed of two curves. The solubility curve (blue curve) separates the one-phase region, where the solution is entirely liquid (undersaturated), from the two-phase region, where the solution is saturated, and excess solute crystallizes out. The other curve represents the metastable boundary (dashed red curve). Above that limit is where nucleation can happen spontaneously and the solution is oversaturated. Between metastable boundary and solubility curve lies the metastable zone (MZ). The MZ represents the region under which the solution is supersaturated but does not immediately crystallize. While the solution is unstable in this region, it won't necessarily form crystals until it's disturbed or until the supersaturation is high enough. Recognizing the MZ is vital for industrial crystallization processes. It allows for controlled crystallization by maintaining the solution within this zone. This control ensures larger crystal growth (which can be desirable) instead of rapid, uncontrollable nucleation. The width of the MZ can be influenced by various factors, including the rate of cooling, impurities present in the solution, and the presence of seeding crystals. A wider metastable zone suggests that the solution can be supersaturated to a greater extent

before spontaneous nucleation occurs (Lorenz 2013; Mullin 2001). In the industry, supersaturation is typically around 30% of the MZW (Lorenz, Polenske, and Seidel-Morgenstern 2006).

### 2.1.3. Phase Diagrams

Phase diagrams represent equilibrium states between phases as a function of variables such as temperature and concentration. Different regions in these diagrams represent the presence of one or multiple phases, which can be pure compounds or mixtures. The number of substances involved categorizes them as binary, ternary, or quaternary diagrams (Lorenz 2013). When dealing with enantiomers, the phase diagram is symmetrical around the racemic composition due to their identical melting characteristics. Enantiomers can be represented in binary systems (showing only the chiral isomer pairs) or ternary systems (including a solvent with the two enantiomers).

Melting point phase diagrams or binary phase diagrams (BPD) help distinguishing the types of enantiomers. They are the pairs of molecules with mirror-image structures, can be categorized into three distinct types based on their binary melting point phase diagrams, as established by (Jacques et al. 1994; Roozeboom 1899). In figure 2.2, we can observe the solid-liquid equilibria (SLE) for mixtures containing two enantiomers, 1 and 2.

Among these three types, the most prevalent are the conglomerate type (depicted in figure 2.2 left). Around 10% of the total enantiomers are conglomerates. They exhibit a single eutectic point. This point denotes the lowest melting temperature, denoted as $T_e$, and takes place when the mixture has a racemic composition, meaning that the molar fractions of the two enantiomers, 1 and 2, are equal ($x_1 = x_2$). Below the eutectic temperature ($T_e$), the system exists solely in the solid state. An important characteristic of conglomerate systems is their ability to completely separate both the enantiomers in the solid state. Consequently, each crystal formed consists of either enantiomer 1 or enantiomer 2. In theory, this implies that the enantiomers can be separated through mechanical methods such as sieving or manual sorting, as famously demonstrated by Louis Pasteur in 1848 (Pasteur 1848). Above the eutectic temperature ($T_e$), there are only two possibilities. Either the system can exist as a single phase (in the area above the liquidus curve) or appear in one of the two regions enclosed by the liquidus and solidus curves, where both the phases coexist.

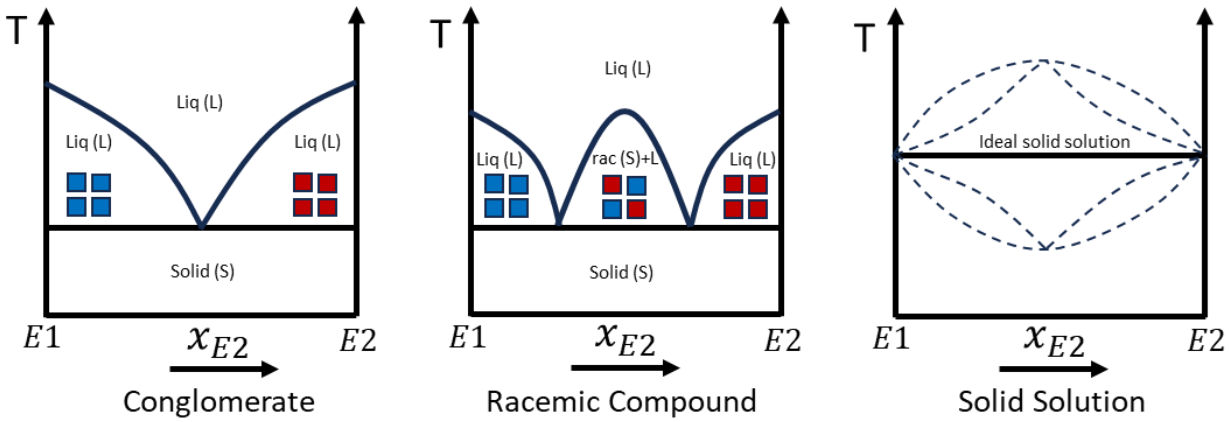


**Figure 2.2**. Binary melting point phase diagram of the three recognized systems. Left plot represents conglomerate system, middle plot is racemic compound forming systems and the right plot is solid solutions.

The compound forming type (figure 2.2 middle) is particularly common and is estimated to constitute more than 90% of all enantiomeric systems, as reported by (collet, Brienne, and Jacques 1980). In addition to the two pure enantiomers, 1 and 2, a third compound known as the racemic compound emerges in the solid state. Its crystal lattice consists of equal proportions of enantiomers 1 and 2. This differs from conglomerates, where the crystal lattice is composed of physical mixture of distinct, homochiral crystals. The binary phase diagram of a racemic compound forming system includes an additional two-phase region cantered around the racemic composition. In this region, crystals of the racemic compound coexist in equilibrium with the liquid phase. It exhibits two eutectic points at deviating compositions. The size of this region depends on the melting point of the racemic compound. In certain cases where the melting point of the racemic compound is significantly lower than that of the pure enantiomers, this region can be quite small, making it challenging to identify the system as racemic compound forming type.

The third type of system is known as solid solutions. It is comparatively rare. Solid solutions, as depicted in binary melting point phase diagrams (right plot in figure 2.2), represent the range over which two components can form a homogeneous solid mixture due to partial or complete solubility of the components in each other. Such diagrams typically feature temperature versus composition axes and display various regions indicating the phase(s) present under varying conditions.

To fully comprehend the thermodynamic interactions in a mixture that includes both enantiomers and a solvent, it's vital to merge information from the solubility diagrams (displayed in figure 2.1) which provide details on how each enantiomer dissolves at various temperatures and the binary melting point phase diagram (as shown in figure 2.2) provides essential data about the melting behaviors of each enantiomer. By synthesizing information

from both these diagrams, we can achieve a clear understanding on the solid liquid equilibria (SLE) of these ternary mixtures, illustrated using figure 2.3.

A ternary phase diagram (TPD) provides a visual representation of the phase behavior involving three components in equilibrium as a function of the composition of each component at a constant temperature and pressure. In the context of chiral crystallization, these components often involve a solvent and a pair of enantiomers. Depending on conditions and inherent properties, these enantiomers can either crystallize separately (conglomerate) or together in a 1:1 stoichiometric ratio (racemic compound). A TPD is typically represented as an equilateral triangle. Each vertex of the triangle corresponds to a pure component (enantiomers 1 and 2 and solvent 3). Any point within the triangle represents a unique composition of the three components, with the position of the point indicating the relative proportion of each. Typically, mole or mass fraction are used to represent the composition. The TPD of two types of crystalline phases (a) conglomerate forming system and (b) racemic compound forming system are illustrated in figure 2.3 (Jacques et al. 1994).

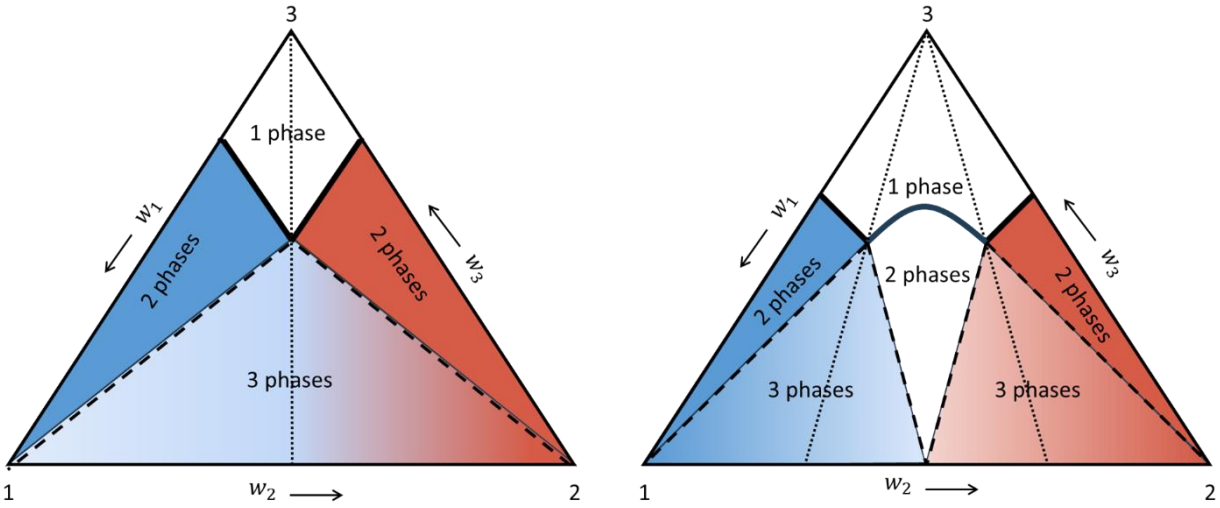


**Figure 2.3**. Ternary phase diagrams are depicted for two types: (a) conglomerate, (b) racemic compound. The thick curves represent solubility isotherms. Dotted lines mark the eutectic compositions. Dashed lines act as boundary markers, indicating the limits of co-existing phases. In these diagrams, the blue regions represent areas with enantiomer 1 crystallizes in liquid phase, while red regions show areas with enantiomer 2.

In conglomerate-forming systems (left diagram of figure 2.3), each enantiomer can crystallize separately. Since each enantiomer exhibits different physical properties, the phase diagram will have distinct regions for each one. The 2-phase region where enantiomer 1 crystallizes separately in the liquid phase is represented by blue color and for enantiomer 2 is shown by red color. Solubility isotherms is represented by thick lines. The region above is undersaturated and therefore exist in one single liquid phase. The 3-phase region below the

solubility isotherms consists of a racemic composition of liquid phase and crystals of pure enantiomers 1 and 2.

A racemic compound (right diagram of figure 2.3) is formed when the two enantiomers crystallize together in a 1:1 ratio as a new, single crystal lattice. It's not a physical mixture like the conglomerate but a distinct crystalline entity. It shows five different equilibrium states due to the formation of the racemic compound. As represented by the blue and red colors respectively, enantiomer 1 and 2 crystallizes separately in liquid phase in these 2-phase regions. Similar to conglomerate system (left diagram of figure 2.3), solubility isotherms are shown by thick lines. Above the isotherm is the 1-phase region where all components are dissolved in one single liquid phase. Below the isotherm, there are two 3-phase regions and one 2-phase region.

Ternary phase diagrams are crucial for assessing the balance and transitions between different states in a mixture, particularly in the context of chemical processes like crystallization. These diagrams provide a detailed mapping of potential outcomes like the specific solid forms that might emerge at varying conditions, and the occurrence of different molecular configurations such as solvates, polymorphs, and solid solutions. They extend beyond simply showing the static equilibria to revealing kinetic states that evolve over time. The metastable solubility, indicated by extending the solubility isotherms beyond the eutectic points in these diagrams, marks a pseudo-equilibrium state (Jacques et al. 1994). This state dictates the system's short-term behaviour and is crucial for understanding the dynamics of the crystallization process over time.

Additionally, these diagrams illustrate the correlation between the solubility of individual components and that of their combined eutectic forms, which is particularly significant in systems where enantiomers form conglomerates. The relationship determines the slope of the solubility curve as it moves from the pure enantiomer to the racemic mixture, consequently affecting the metastable zone width—an important consideration for developing strategies for chiral resolution.

The solubility ratio, denoted as $w_{ratio}$, is an important term in this analysis. It's calculated by comparing the equilibrium solubility of the racemic mixture, $w_{rac}$, to that of a single pure enantiomer, $w_{sat,i}$, at a given temperature as shown in eq. 2.4. In an ideal mixture, the solubility of the racemic compound is expected to be twice that of an individual enantiomer, resulting in a solubility ratio of 2.

$$w_{ratio} = \frac{w_{rac}}{w_{sat,i}} \qquad i = 1,2 \tag{2.4}$$

This detailed understanding of solubility and phase diagrams is fundamental for chemists and engineers who aim to optimize crystallization processes for the efficient production and purification of chiral substances, which are often used as building blocks in various areas such as pharmaceuticals.

## 2.2. Crystallization kinetics

The fundamental kinetic processes that govern the formation of crystals—such as the initiation of crystal structures (nucleation), their growth, and their potential dissolution—are complex and not fully understood. However, to effectively design and manage crystallization processes, it is essential to have a quantitative model of these kinetic processes. To mathematically represent how the characteristics of a population of particles change over time and space within a certain area, a system of equations known as Population Balance Equations (PBE) are used (Randolph and Larson 1988). These equations differentiate individual particles within the population based on a series of unique properties, such as their location or their size and form. Alternatively, we have developed a shortcut model (SCM) (discussed in chapter 4) to quickly access the key performance indicators of the crystallization process (Carneiro et al. 2019).

In both PBE and SCM, the principal equations incorporate specific mathematical terms that account for the kinetics—the rates and mechanisms of the changes occurring within the system. For every given substance or experimental set-up, the values for these kinetic terms must be determined separately. The mathematical understanding provided by these models about the process is crucial for developing precise control measures and for designing processes that can predictably and efficiently lead to the formation of crystals.

### 2.2.1. Kinetic mechanism of crystallization process

Crystallization is the process by which a liquid or an amorphous solid transform into a crystalline solid phase (Mullin 2001). As mentioned earlier in this chapter, supersaturation is the primary force that drives this transformation, and for the substances and processes examined in this study, it is mostly achieved through changes in temperature.

When a solution is undersaturated, existing crystals will dissolve, preventing the formation of new solid phase. However, when the temperature of such a solution drops, a point of saturation will be reached (as described by eq. 2.1) where the concentration of the dissolved substance equals its solubility at the new temperature, leading to a stable condition where neither dissolution nor crystallization takes place. As the temperature continues to fall, the solution becomes supersaturated, which favours the growth of existing crystals. Nonetheless, the creation of new crystals, or nucleation, won't happen in a clear solution until it is sufficiently subcooled (Mullin 2001; Nyvlt et al. 1985). During this metastable phase, transient

clusters of the substance's building-blocks form and typically dissolve again. These clusters grow larger with increasing supersaturation, reaching a critical size where they are just as likely to dissolve as they are to grow. This threshold marks the edge of the metastable zone, beyond which rapid crystal formation occurs, and small crystals start to grow, or agglomerate as the excess solute in the solution is used up. Furthermore, during the process, larger crystals may collide with the mixing device, the walls of the reactor, or other particles, causing them to break apart or wear down.

The thermodynamic principles outlined earlier lay the groundwork for understanding how a system transitions from the initial to the final state during crystallization. Once a state of supersaturation is attained, the system attempts to stabilize itself by attaining equilibrium. It does this through two principal kinetic mechanism: nucleation and crystal growth. It will be analysed and discussed in the subsequent sections along with the corresponding mathematical models that describe them. This discussion will aid in understanding the complexities of crystallization, necessary for designing more efficient and controlled crystallization systems.

### 2.2.2. Nucleation

Nucleation is the initial step where atoms or molecules arrange into a new phase or structure, marking the birth of a crystal. This process can occur spontaneously in a supersaturated solution, where the concentration of solute molecules is higher than in a saturated solution, leading to a state of instability. This instability prompts the molecules to cluster together to reduce the system's free energy, forming a stable nucleus. Once a nucleus reaches a critical size, it can serve as a foundation for further growth. Nucleation is classified based on various influencing factors that drive the formation of nuclei. According to (Mullin 2001), the process falls into distinct categories: Primary homogenous nucleation, primary heterogeneous nucleation and secondary nucleation.

Homogeneous primary nucleation is the process where a new phase begins to form in a uniform system without any foreign substances or surfaces to facilitate the process. This type of nucleation can occur in both pure melts and solutions. It is a stochastic process that involves fluctuations within the system that lead to the formation of a stable cluster of a new phase. The Classical Nucleation Theory (CNT) (Becker and Döring 1935; Farkas 1927; Frenkel 1939; Volmer and Weber 1926) provides a mathematical framework to describe homogeneous primary nucleation. The theory is built around the concept of the Gibbs free energy of formation of a cluster of the new phase within the old phase.

According to the CNT and illustrated in figure 2.4, the change in Gibbs free energy (ΔG) for the formation of a spherical cluster of radii $r$ in a homogeneous phase is given by the sum of a positive term due to the creation of a new surface (with surface tension $\gamma$) and a negative

term due to the volume free energy change (with a bulk free energy change per unit volume $\Delta\mu$):

$$\Delta G = \Delta G_v + \Delta G_s = -\frac{4}{3}\pi r^3 \Delta\mu + 4\pi r^2 \gamma \quad 2.5$$

Here:

- $\Delta G$ is the change in Gibbs free energy.
- $r$ is the radius of the spherical cluster.
- $\gamma$ is the surface tension between the two phases.
- $\Delta\mu$ is the difference in chemical potential between the bulk phases, which is related to the degree of supersaturation.

The first term $4\pi r^2\gamma$ represents the amount of energy to create a new surface of the nucleus. The second term $-\frac{4}{3}\pi r^3\Delta\mu$ is the free energy gain from the bulk phase transition.

The critical radius $r_{crit}$, where the cluster becomes stable and capable of growing, is estimated when the derivative of $\Delta G$ with respect to $r$ is zero:

$$\frac{d\Delta G}{dr} = 0 = 8\pi r_{crit}\gamma - 4\pi r_{crit}^2 \Delta\mu \quad 2.6$$

$$r_{crit} = \frac{2\gamma}{\Delta\mu} \quad 2.7$$

The critical Gibbs free energy $\Delta G_{crit}$ is the maximum energy barrier that must be overcome for a cluster to become a stable nucleus (Mullin 2001):

$$\Delta G_{crit} = \frac{16\pi\gamma^3}{3(\Delta\mu)^2} \quad 2.8$$

The rate of nucleation $B_{prim}$, which is the number of nuclei forming per unit volume per unit time, is then given by an Arrhenius-type expression (Farkas 1927; Frenkel 1939):

$$B_{hom} = k_b \exp\left(\frac{\Delta G_{crit}}{kT}\right) \quad 2.9$$

Here:

- $B_{hom}$ is the nucleation rate.
- $k_b$ is a pre-exponential factor that includes the attempt frequency of molecules to join the cluster.
- $k$ is the Boltzmann constant.
- $T$ is the absolute temperature.

The pre-exponential factor $k_b$ is often difficult to determine and can vary significantly depending on the specifics of the system.

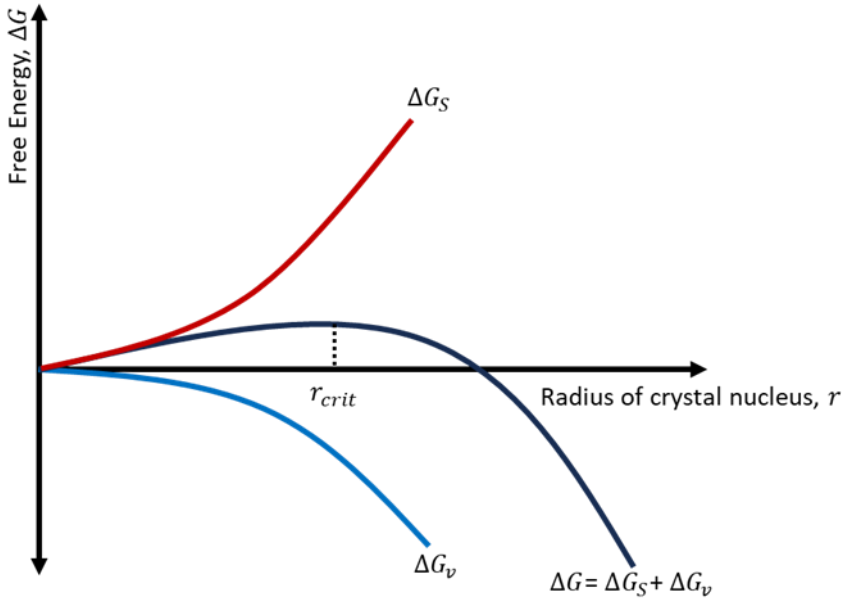


**Figure 2.4**. Overall free energy $\Delta G$ as a function of cluster size $r$ for homogeneous primary nucleation.

Heterogeneous primary nucleation is the process by which a new phase or a new structure begins to form on a pre-existing surface. This surface can be a foreign particle, a container wall, or any interface other than the phase that is nucleating. The presence of this surface lowers the energy barrier for nucleation compared to homogeneous nucleation, making the process more energetically favorable and often faster (Mullin 2001). Heterogeneous nucleation is significantly more complex than homogeneous nucleation because the nature of the surface, its interactions with the nucleating phase, and the exact conditions under which nucleation occurs can greatly affect the process.

Secondary nucleation in crystallization is the process where new crystals are formed from pre-existing crystals, rather than from the pure solvent or solution (Botsaris 1976; Mullin 2001; Nyvlt et al. 1985). This process occurs at lower levels of supersaturation compared to primary homogeneous or heterogeneous nucleation (Kadam, Kramer, and Ter Horst 2011). Secondary nucleation can be influenced by several factors, such as fluid shear, inter-crystal collisions, and the presence of impurities or additives.

The physical mechanisms behind secondary nucleation include:

1. Contact Nucleation: When existing crystals collide with each other or with the walls of the crystallizer, small fragments can break off and serve as new nuclei.

2. Shear-induced Nucleation: Fluid motion and shear can cause the erosion of crystal surfaces or the removal of small crystallites, which can then grow independently.

3. Attrition Nucleation: Larger crystals breaking into smaller fragments under mechanical stress, such as stirring, can create new nuclei.

Secondary nucleation is often described mathematically through power law (eq. 2.8) (Elsner, Ziomek, and Seidel-Morgenstern 2011; Mueansichai et al. 2013; Randolph and Larson 1988) because the exact mechanisms can be complex and are not fully understood at a fundamental level. These correlations usually relate the rate of secondary nucleation to the level of supersaturation, the amount of solid present, the shear rate, and other process parameters.

$$B_{sec} = k_b \omega^{P_1} \rho_{susp}^{P_2} \exp\left(-\frac{E_A}{RT}\right)(S-1)^{P_3} \qquad 2.10$$

where:

- $B_{sec}$ is the secondary nucleation rate,
- $\omega$ is the stirrer speed
- $\rho_{susp}$ is an empirical constant,
- $E_A$ is the concentration of crystals,
- $P_1, P_2$ and $P_3$ are empirical exponents,
- $k_b$ a pre-exponential factor encompasses all additional effects that influence secondary nucleation, such as the dependency on crystal shape or the geometrical characteristics of the setup, which are assumed to be stable.
- $S$ is the supersaturation level.

### 2.2.3. Crystal Growth

Following the formation of a new solid phase by nucleation, the size of the individual particles increases through the process of crystal growth. This typically involves the movement of solute molecules—or growth units—from the bulk of the solution to the boundary layer that exists at the interface between the crystal surface and the solution. These molecules must then diffuse through this boundary layer and locate a site on the crystal surface where the energy conditions are optimal for attachment, allowing them to be incorporated into the crystal structure. Numerous theories have been formulated to explain the various stages of crystal growth and to derive a general equation for the rate of crystal growth.

The intricate process of crystal growth is elucidated by various theories, broadly classified into two categories. The first includes two-dimensional growth theories, such as the mononuclear, polynuclear, and birth and spread models. These suggest that crystal growth occurs through discontinuous two-dimensional nucleation, with growth rates influenced by the critical size of nuclei formation. However, these models often fall short in accurately predicting growth rates under conditions of low supersaturation, as the nucleation events become rare.

For continuous growth on crystal surfaces, the Burton-Cabrera-Frank (BCF) theory offers a more refined approach (Burton, Cabrera, and Frank 1951). This model introduces the concept of screw dislocations—a type of defect in the crystal lattice. These dislocations create a continuous helical ramp that allows for the addition of growth units without the need for nucleation. As a result, the growth process resembles a spiral staircase. Surface diffusion—the movement of growth units along the surface to the step edge is considered the limiting factor for growth rate in this model. To enhance the BCF theory, the diffusion layer model (Chernov 1961), shifts the focus to bulk diffusion as the limiting step in crystal growth. Comprehensive explanations of these theories and their implications for crystal development are extensively documented in works by (Mullin 2001; Myerson 2002; Nyvlt et al. 1985; Ohara 1973). These theories postulate that the crystal growth mechanism consists of two primary phases: (i) the movement of the solute from the bulk solution to the vicinity of the crystal, and (ii) the attachment of the solute molecule onto the crystal surface. The growth of a component through these stages can be collectively described using the following power law expression:

$$\frac{dm_S}{dt} = k_g A(c - c_{sat}(T))^g \qquad 2.11$$

Eq. 2.11 mathematically models the kinetics of crystal growth, where the rate of increase in the mass of solid component is determined by three factors: the growth rate constant $k_g$, the exposed surface area of the crystal $A$, and a power $g$ that characterizes the influence of supersaturation on the growth process. Here, $c$ represents the bulk concentration of the solute, and $c_{sat}$ is its equilibrium saturation concentration. The term $(c - c_{sat}(T))^g$ serves as the driving force for crystal growth, indicating that the rate at which the solid mass increases is directly proportional to how supersaturated the solution is relative to the solute's saturation concentration.

To express the growth rate of a specific dimension, L, for integration into the Population Balance Equation (PBE) model is given by eq 2.12 (Randolph and Larson 1988)

$$G = \frac{dL}{dt} = k_g(T)(S(T) - 1)^g \qquad 2.12$$

The temperature dependence of equation 4.14 can be effectively estimated using the well-established Arrhenius equation (Mullin 2001; Nyvlt et al. 1985).

$$k_g = k_{g,0} \exp(-\frac{E_{A,g}}{RT}) \qquad 2.13$$

Although eq. 2.13 effectively models experimental data into crystallization process, it overlooks two significant factors: the presence of additives and individual variations in growth rates for each crystal.

Additives often introduced during processing or through the materials used can substantially reduce growth rates, even at minimal concentrations (Nyvlt and Ulrich 1995). These effects can be anisotropic, potentially altering crystal morphology, as detailed in several studies (Kuvadia and Doherty 2013; Rauls et al. 2000; Sangwal 2007). However, the exact mechanisms by which different impurities influence growth remain incompletely understood, resulting in 'effective' growth rates that are particular to each experimental setup.

Moreover, individual crystals exhibit unique growth rates, a phenomenon known as growth rate dispersion (Mullin 2001; Nyvlt et al. 1985). According to the Gibbs-Thomson effect, smaller crystals (under 1μm) dissolve more readily and grow more slowly. Fluid dynamics also play a role; larger crystals experience different flow conditions than smaller ones, affecting substance transport resistance and potentially leading to higher abrasion rates due to collisions with reactor elements, which can reduce their growth rate. While these variations are often confused with size-dependent growth, they're also influenced by intrinsic factors like lattice defects, leading to a spread in the growth rates within a crystal population (Jones and Larson 1999; Srisanga et al. 2015).

## 2.3. Isothermal Preferential Crystallization (PC)

The recognition of chirality dates back to the 19th century, starting with Louis Pasteur's famous discovery in 1848 (Pasteur 1848), where he manually separated the enantiomers of sodium ammonium tartrate using a microscope and tweezers, noting their different effects on plane-polarized light. The development of preferential crystallization as a technique for separating enantiomers has evolved over the years. It gained particular importance in the 20th century as the demand for enantiopure compounds in the pharmaceutical industry grew. The thalidomide tragedy in the 1950s and 1960s, where one enantiomer caused severe birth defects while the other was therapeutically effective, underscored the need for enantiomeric purity in drugs, propelling the advancement of chiral resolution techniques (Jacques et al. 1994).

Preferential crystallization is a crucial technique in chiral resolution, which is used to separate enantiomers. This process is of paramount importance in the pharmaceutical industry due to its cost-effectiveness, scalability and simplicity. Furthermore, it is energy efficient and has a potential to scale up in a continuous mode (Jacques et al. 1994; Jones, Budz, and Mullin 1986; Myerson 2002). PC can be used to separate a racemic mixture (a 50:50 mixture of enantiomers) into its individual enantiomers. Separating enantiomers through preferential crystallization is feasible due to the significant role that kinetic factors play in the

crystallization process. The foundational concept behind preferential crystallization is enantioselective crystallization. This phenomenon occurs in a scenario where both enantiomers have reached a level of supersaturation and are ready to crystallize at the same time. However, when a supersaturated solution is introduced to a seed crystal, it does not achieve equilibrium instantly. Instead, there is a delay before nucleation starts, which comes from the different energy requirements for initiating nucleation compared to those for continuing the growth of seeded crystals. It takes less energy to grow an existing crystal than to start forming a new one. This kinetic benefit allows one enantiomer's crystals to grow in preference to the other during a certain period, enabling their separation.

### 2.3.1. Batch PC

Conventional batch preferential crystallization, typically conducted in a single stirred tank under constant temperature conditions, is foundational for understanding enantioseparation. The process often begins with a racemic solution that is not yet saturated with the compound of interest. To initiate crystallization, the solution is cooled to a point below its saturation temperature, a process known as subcooling. This cooling must be done cautiously to ensure that the solution achieves supersaturation and enters the metastable zone—a state where spontaneous nucleation is avoided, yet crystal growth can occur without crystallizing out of solution too quickly. Knowing the metastable zone width is crucial because it informs how much the solution can be subcooled without triggering uncontrolled nucleation. The proper degree of subcooling is determined based on this prior knowledge, allowing for a controlled crystallization process that favors the growth of one enantiomer over the other. In the metastable zone, the process of spontaneous nucleation is kinetically hindered, which means it doesn't occur immediately. This delay creates a valuable opportunity for enantioseparation. During this period when the solution is supersaturated yet free of crystals, enantioseparation can commence with the introduction of enantiopure seed crystals. These seeds act as a base for the growth of one enantiomer, while the formation of the counter enantiomer's crystals is kinetically suppressed, allowing for the selective crystallization of the desired enantiomer. This step is graphically illustrated with a red circle in figure 2.5. To verify how PC progresses over time through experiments, optical rotation in real-time can be estimated using a polarimeter. The optical rotation of isothermal batch preferential crystallization has similar time profile as the enantiomeric excess of the liquid phase. It is given by:

$$\alpha = \frac{ee_L\,(w_1 + w_2)}{k_\alpha} \tag{2.14}$$

$$ee_L = \frac{|w_2 - w_1|}{w_2 + w_1} \tag{2.15}$$

where:

- $\alpha$ is the optical rotation,
- $ee_L$ is the enantiomeric excess in the liquid phase,
- $w_1, w_2$ are the weight fraction of both enantiomers (eq. 2.3),
- $k_\alpha$ is the temperature dependent calibration parameter,

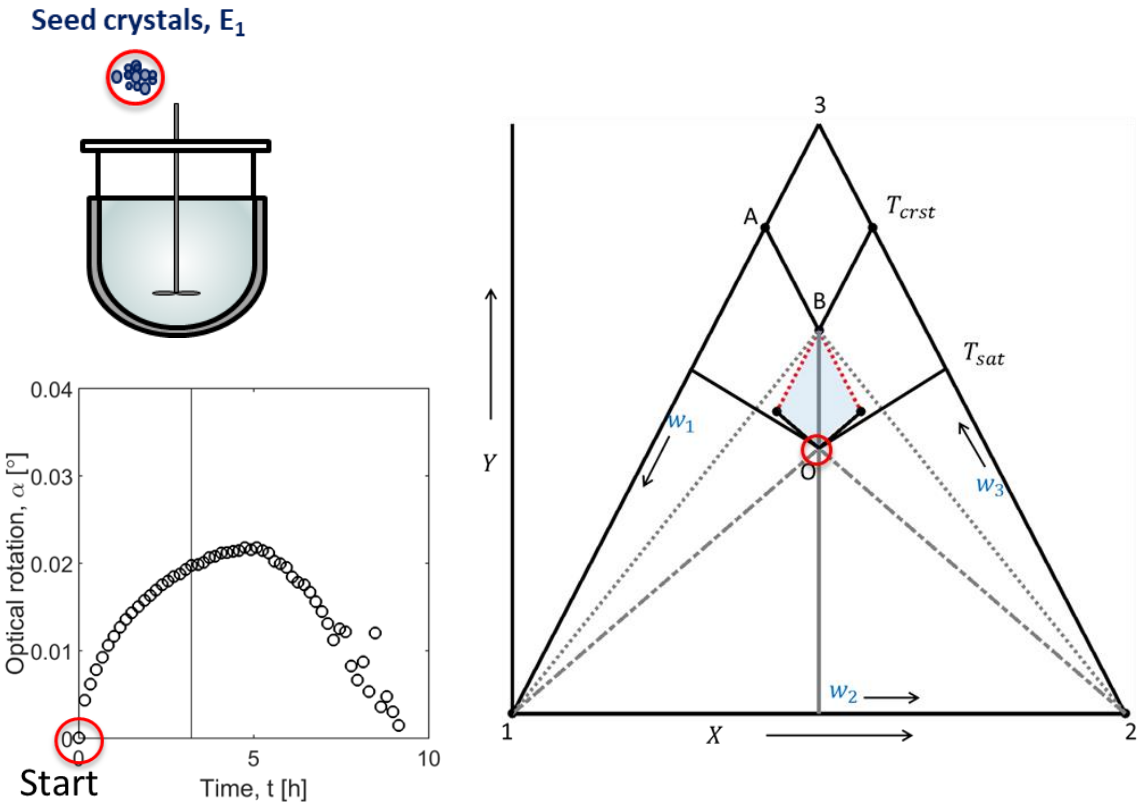


**Figure 2.5**. Progress of isothermal batch Preferential Crystallization process. Seeding step is marked with red circle in single batch crystallizer, Ternary Phase Diagram and Optical rotation plot (chapter 5, Table 5.2, experiment $I_{(2)}$).

The process of PC can be mapped out on a ternary phase diagram, as shown in figure 2.5. This figure includes solid lines that indicate solubility isotherms, labeled $OT_{sat}$ and $BT_{crst}$. Metastable zone is depicted by extending the solubility lines beyond the point where the solution is in equilibrium, illustrate using dotted red lines in the figure. The metastable zone, colored blue on the diagram, lies between the temperatures at which the solution becomes saturated ($T_{crst}$) and the temperature at which crystals start forming ($T_{sat}$). The width of the metastable zone differs for each substance being crystallized. The angle or steepness of the solubility isotherms in the phase diagram determines how large this zone is (eq. 2.4). Compounds that significantly differ in solubility between the racemic mixture and the single enantiomer at the temperature of crystallization will have sharper or steeper isotherms, leading to a smaller metastable zone for conducting preferential crystallization. Optical rotation at the seeding step is zero as both the enantiomers are in equal proportion in the liquid phase.

In the next step on the progress of PC, the crystals of the target enantiomer will grow predominantly, utilizing the available surface area. However, after a certain period known as the stop time (discussed later in chapter 4, section 4.1.4.1), crystals of the unwanted enantiomer begin to form, which affects the purity of the desired product. Therefore, in order to attain high purity, the process of PC must be stop at this point. This step is marked with red circle in figure 2.6. In the TPD, the black curve $OB$ represents the progress of PC process. When seeds of only one type of enantiomer (enantiomer 1) are added to the solution, the composition begins to shift away from the corresponding corner of the ternary phase diagram, marked as vertex 1. This shift is due to the selective crystallization of enantiomer 1, which moves the solution closer to the metastable solubility boundary, indicated by a dotted line in the diagram. The point marked with the red circle in figure 2.6 traces the period during which only the seeded enantiomer (enantiomer 1) is crystallizing. This phase spans from the beginning ($t$ = 0) of seeding until a specific point referred to as stop time ($t_{stop}$). Following this period, crystals of the counter enantiomer (enantiomer 2) start to form, causing the solution's composition to drift away from the pure enantiomer 2 vertex and move toward the metastable solubility boundary on the diagram's left side. On the optical rotation plot, at this step, we see an enantiomeric excess of the counter enantiomer in the liquid phase as the target enantiomer has been crystallized to the solid phase.

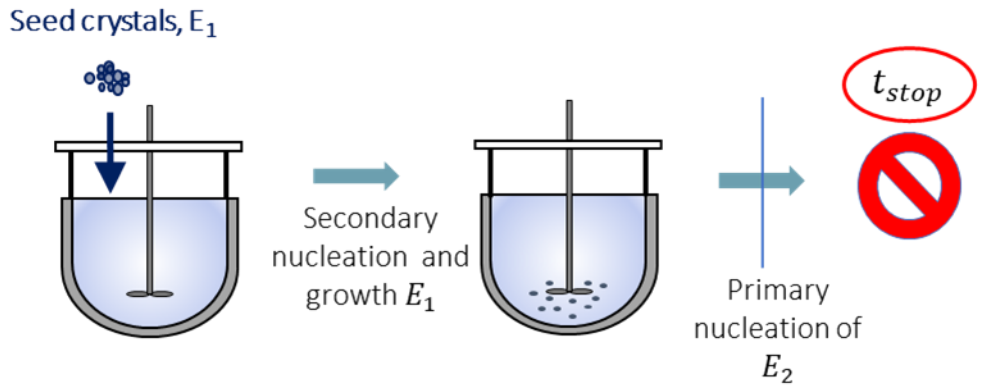

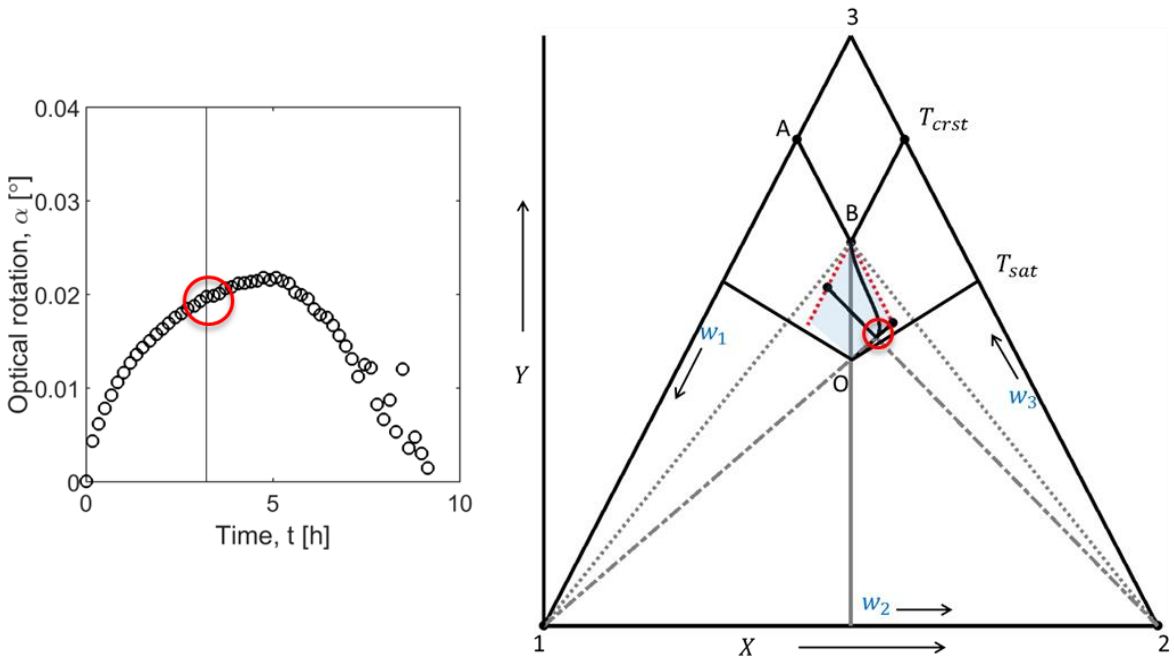


**Figure 2.6**. Progress of isothermal batch Preferential Crystallization process. Stopping step is marked with red circle in single batch crystallizer, Ternary Phase Diagram and Optical rotation plot (chapter 5, Table 5.2, experiment $I_{(2)}$).

If the process is allowed to continue undisturbed for an extended duration, the system will naturally move towards a state of equilibrium. In such a state, the solution (mother liquor) and the crystalline product will both be racemic, containing equal amounts of both enantiomers. Nevertheless, due to the initial seeding, the crystal product may retain a minor excess of the intended enantiomer. This step is demonstrated using red circle in figure 2.7. As shown in the TPD marked with the red circle, ultimately, the system settles into an equilibrium state at point $B$, where both the liquid and solid phases present a racemic composition, meaning they contain equal amounts of both enantiomers. Thus, at equilibrium, the optical rotation has become zero again as both the liquid and solid phase forms a racemic composition.

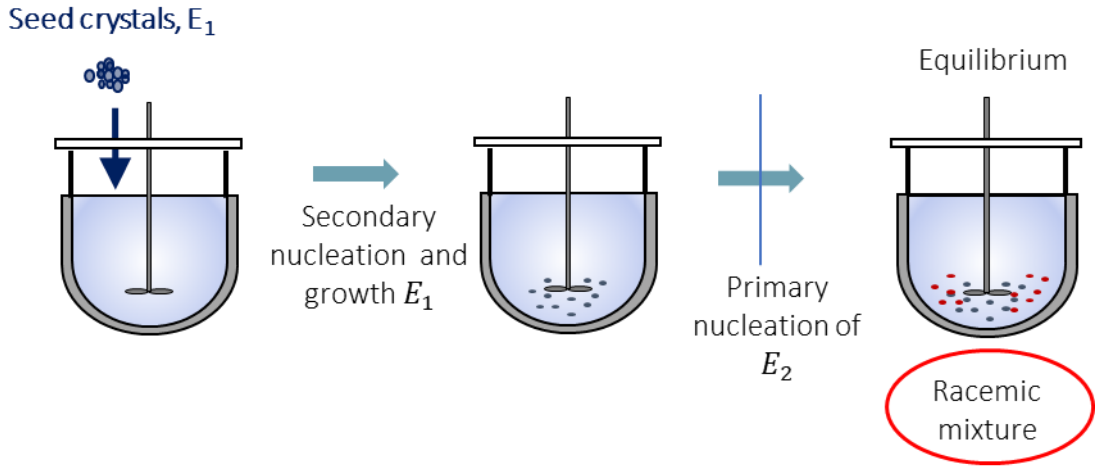

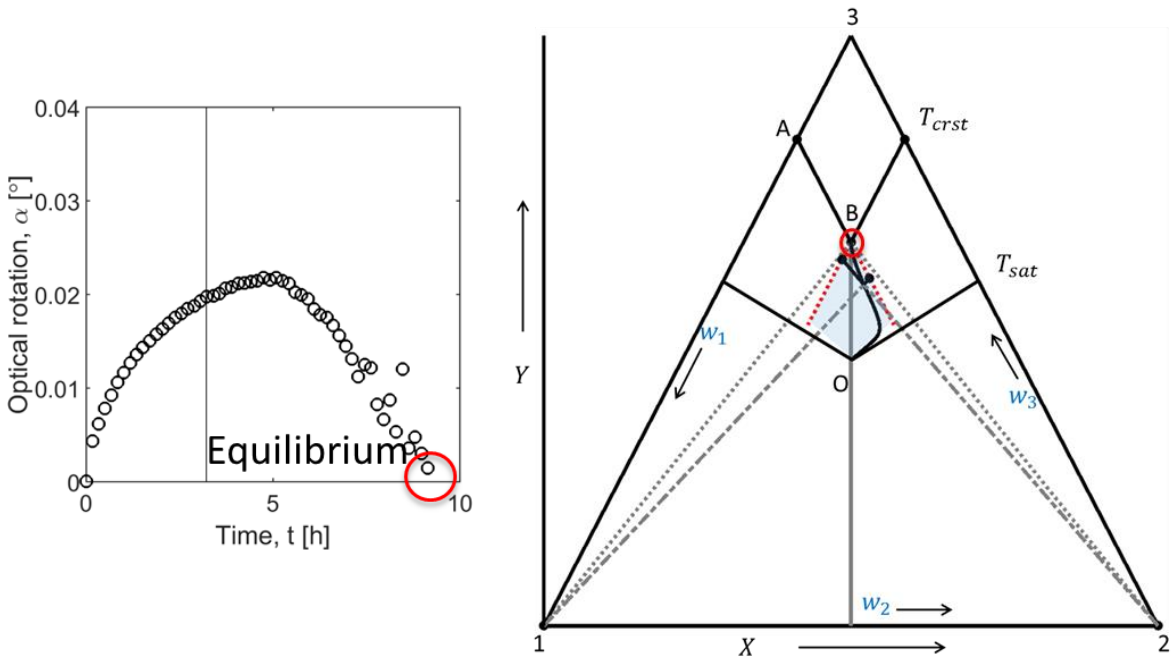


**Figure 2.7**. Progress of isothermal batch Preferential Crystallization process. Equilibrium step is marked with red circle in single batch crystallizer, Ternary Phase Diagram and Optical rotation plot (chapter 5, Table 5.2, experiment $I_{(2)}$).

The primary limitation of the preferential crystallization process is its low yield, primarily because the unwanted enantiomer constitutes up to 50% of the solution. Additionally, in some cases, the time it takes for the unwanted enantiomer to begin nucleating can be so short that achieving 100% purity becomes challenging, demanding alterations to the process (Srimahaprom and Flood 2013). To address these issues, a coupled-crystallizer setup has been proposed, where the mother liquors are interchanged between two vessels (Chaaban et al. 2013; Elsner et al. 2011; Hein et al. 2013). Both crystallizers start with the same racemic solution and are cooled to an identical subcooling temperature. Then, each crystallizer is seeded with pure crystals of opposite chirality. The liquid phases maintain a racemic concentration due to the continuous exchange between the crystallizers, provided if it occurs quickly. This exchange minimizes the concentration of the unwanted enantiomer in each crystallizer's liquid phase because it preferentially crystallizes in the other tank. Moreover, the liquid exchange impacts the supersaturation levels—increasing it for the seeded enantiomer and reducing it for the other, thereby promoting the racemization of the liquid phase.

In recent years, the scientific community has shown growing interest in advancing crystallization techniques, focusing on both batch and continuous modes of operation (Wood et al. 2019). This surge in research aims to optimize the crystallization process for various applications, enhance efficiency, and adapt to the needs of large-scale production. An additional strategy to enhance the process involves combining preferential crystallization with selective dissolution. In this setup, two crystallizers are connected and operate at

different temperatures. While one crystallizer undergoes the standard preferential crystallization, the other engages in selective dissolution from a racemic solid phase (Levilain, Eicke, and Seidel-Morgenstern 2012; Temmel et al. 2019). This method allows for the selective enrichment of one enantiomer in one crystallizer while the other crystallizer helps in dissolving the undesired enantiomer, thereby improving the overall yield and purity of the target compound.

An alternative method for separating enantiomers is through solid-state deracemization, which can be done by either grinding (Ishikawa et al. 2020; Sögütoglu et al. 2015; Xiouras et al. 2019) or temperature cycling (Cameli et al. 2020; Intaraboonrod, Harriehausen, et al. 2020). Grinding involves physically breaking down the racemic mixture to promote the separation of enantiomers, while temperature cycling entails repeated heating and cooling to achieve the same effect. One of the newer techniques that has drawn considerable attention over the last ten years is Viedma Ripening (Viedma 2005). Unlike preferential crystallization, which operates away from thermodynamic equilibrium, Viedma Ripening takes place close to equilibrium and transforms a racemic solid into a single-enantiomer product. Viedma Ripening encompasses several processes including attrition, where particles are broken down; agglomeration, where particles stick together; Ostwald ripening, a process where larger particles grow at the expense of smaller ones; and a racemization reaction within the liquid phase. While Viedma Ripening operates under thermodynamic equilibrium conditions, making it potentially suitable for some applications, the choice between this method and others like preferential crystallization depends majorly on the compound.

### 2.3.2. Continuous PC

In the pharmaceutical production field, crystallization is a key step that usually connected with other downstream processes such as filtration and drying. Traditionally, crystallization is done in batches, but this approach can lead to inconsistent product quality, which may affect the later stages of manufacturing (Chen et al. 2011; Plumb 2005). On the other hand, continuous crystallization methods are gaining favour because they can use smaller equipment and potentially cut down on costs. Moreover, when continuous systems reach a stable operating condition, they tend to produce results that are more reliable and of higher quality (Köllges and Vetter 2018; Vetter, Burcham, and Doherty 2015).

The MSMPR (Mixed Suspension, Mixed Product Removal) model is a theoretical framework used to understand crystallization kinetics, specifically the rates of crystal growth and nucleation (Jones et al. 1986; Mersmann 2001; Mullin 2001; Nyvlt et al. 1985; Randolph and Larson 1988). This model helps describe how a continuous crystallizer operates at a steady state by simplifying the population balance regarding crystal size distribution. To use the MSMPR model, certain conditions must be met in experiments. The system should maintain a steady state with consistent temperature and supersaturation, constant inflow and volume,

as well as stable mixing within the crystallizer. It's typically assumed that the crystallizer is perfectly mixed, with a solid-free feed and uniform removal of the product. To avoid crystallization of the counter enantiomers, the mother liquid has to be in the metastable zone throughout the process.

Continuous PC can also be characterized using dimensionless numbers, which are mathematical tools that simplify the complexity of physical processes. These numbers help compare the influence of different factors on the crystallization process without the constraints of specific units of measurement. Experts in Chemical Reaction Engineering (CRE) have investigated deeply into the specifics of continuous processes (Fogler 2006; Levenspiel 1998; Zlokarnik 2006). Scholars like Garside and Tavare have found that reaction engineering and crystallization share many similarities (Garside and N.S. 1984). They have used the similarities in the fundamental laws of mass conservation and kinetics from reaction engineering to better understand crystallization. An important discovery from their work is that certain dimensionless numbers (Weller 1994), which are important in CRE for analysing reactions, can also be very useful in crystallization once they're properly adjusted. These numbers help in predicting how crystallization processes will behave.

Building on this insight, in section 4.2 of chapter 4, we plan to use two well-known dimensionless numbers applied in the Chemical Reaction Engineering (CRE) community—namely the Damköhler number (Damköhler 1936; Inger 2001; Rehage and Kind 2021) and the Bodenstein number (Westerterp et al. 1984)—to extend our existing shortcut model (section 4.1 of chapter 4) for batch preferential crystallization. These adaptations will help us to better understand and design continuous PC processes, which are becoming a more appealing option in the industry.

### 2.3.3. PC with racemization reaction

Integrating preferential crystallization with racemization can significantly enhance yields in optical resolution, an advantage especially when only one enantiomer is needed for a pharmaceutical product. Instead of crystallizing both enantiomers, which may not be economically viable, converting the undesired enantiomer back to a racemic form through racemization is more cost-effective and sustainable. It recycles the unwanted enantiomer and helps prevent its crystallization and potential contamination of the desired product. Ideally, this combination keeps the mother liquor racemic, ensuring the final product's purity. This approach has been termed "crystallization induced asymmetric transformation" (Yoshioka 2006) or "second-order asymmetric transformation" (SOAT) (Levilain and Coquerel 2010; Oketani et al. 2019b).

Racemization, a process where one enantiomer of a molecule is converted into its mirror image, can be catalysed both chemically and using enzymes (Horn et al. 2008; Segel 1975).

There are mostly metal organic chemical catalysts for racemization available (Von Langermann et al. 2012).

However, the use of (biocatalysts) enzymes offers certain benefits:

- Milder Conditions: Enzymatic reactions often occur under mild temperature and solvent conditions, which are more likely to be compatible with the delicate nature of the resolution process.

- Versatility of Enzyme Use: Enzymes can be used in their free form, which is generally less costly, or in an immobilized state, which, although potentially more expensive, can improve enzyme stability, allow for repeated use, and make separation from the product easier.

The efficiency of racemization is influenced by the concentration difference between the two enantiomers (i.e. by the driving force for racemization), which, in the case of applying preferential crystallization (PC) is rather small. Research has shown that having a racemization reaction in parallel with PC can be advantageous—it can enhance the supersaturation necessary for PC by speeding up the growth of the desired enantiomer while simultaneously inhibiting the nucleation of the counter enantiomer (Carneiro et al. 2020; Harriehausen et al. 2021; Oketani et al. 2019b; Steendam and Ter Horst 2017; Würges et al. 2009; Yagishita et al. 2012). Combining racemization with PC introduces a variety of possible setups, which will be further explored and extended to SCM in section 4.3 of chapter 4 (Bhandari et al. 2022).

# 3. Models applied for quantifying PC

Modeling the preferential crystallization (PC) process is about creating a detailed roadmap that predicts how changing different variables (like temperature or seed mass) affects the performance of the process. It involves developing a mathematical model of the physical and chemical phenomena that occur during the separation and purification of enantiomers. This process is complex, as it involves understanding and simulating the interactions between solid and liquid phases such as the kinetics of crystal growth and nucleation, and the thermodynamics of chiral compounds.

For an effective modeling of the PC process, it is important to understand the system. This involves identifying whether the enantiomers belong to a conglomerate-forming system or a racemic compound-forming system (discussed in chapter 2). Subsequently, estimating the solubility of the compound is a critical step. Enantiomers often have different solubilities in various solvents, which is a key aspect exploited in preferential crystallization. Therefore, the next step is to create phase diagrams (discussed in chapter 2). These diagrams show how the solubility of enantiomers changes with temperature and composition. They are foundational for understanding at what conditions crystallization will occur. Upon comprehending the thermodynamics, the subsequent step involves exploring the kinetics of the process. It involves understanding how crystals of each enantiomer form (nucleation kinetics) and grow (growth kinetics). After acquiring knowledge of thermodynamics and kinetics of the compound in a given solvent, the PC process can be quantified and optimized by varying process parameters such as temperature, supersaturation and seed mass using various process models. Among them, Population balance equations (PBE) form the foundation of the most widely used models for describing preferential crystallization.

## 3.1. Population Balance Model

The Population Balance Model (PBM) is a mathematical framework used to describe the dynamics of a population of particles, such as crystals in a solution. In a population, each individual can be identified by a collection of independent characteristics, as noted in reference (Randolph and Larson 1988). External coordinates are used to outline their spatial distribution, while internal coordinates characterize the intrinsic attributes such as size and shape. The solid phase (consists of solid particles) interacts with a continuous phase, such as a liquid or gas, to facilitate necessary mass or energy transfer for the process under consideration. To ensure the conservation laws, specific balances are applied for the exchange between the solid and the continuous phase. These balances account for the state of the overall system, varying over time and space. For more detailed explanations of PBM, the books by (Ramkrishna 2000) and by (Randolph and Larson 1988) serve as comprehensive resources. In the context of preferential crystallization (PC), it is used to model the nucleation and growth of enantiomer crystals from a racemic solution. The PBM helps in understanding

how different factors influence the size and distribution of crystals, which is crucial for achieving the desired purity and yield of the desired enantiomers.

### 3.1.1. Mass balance of the solid phase (or dispersed phase)

Simplified Population Balance Equations (PBEs) with a single internal coordinate, typically size, are often used in crystallization processes. In case of an ideally-mixed crystallizer, it is generally assumed that the characteristic properties of the particles do not vary with their position inside the vessel. Therefore, in such scenarios, spatial external coordinates are not incorporated into the mathematical model. This simplification helps in focusing on the internal characteristics of the particles, making the analysis more straightforward and less complex. In this study, the 1-D PBE is formulated based on the characteristic length coordinate, denoted as $L$ and given by eq. 3.1:

$$\frac{\partial f_i(t,L)}{\partial t} = -\frac{\partial}{\partial L}\big(G_i(S,L,T) f_i(t,L)\big) + B_i(S,T) \qquad i = 1,2 \tag{3.1}$$

The above PBE equation represents the evolution of the number density distribution, $f(L,t)$ with size $L$ over time $t$, of enantiomer $i$, where $i$ represents either 1 (preferred enantiomer) or 2 (counter enantiomer). $B_i$ represents the nucleation kinetics and $G_i$ is the growth kinetics. In this context, the nucleation rate is represented through the boundary conditions in the discretization of the PBEs system. As a result, it can be neglected from the general formulation of the equation. Since no particles are introduced into or removed from the reactor, eq. 3.1 is specifically applicable for the simulations of a polythermal batch PC process. In the case of PC, it is often assumed that crystal growth and nucleation rate, driven by supersaturation denoted as $S$ (eq. 2.1), is the key factor influencing the evolution of the number density function. Consequently, other kinetics such as agglomeration, attrition and dissolution are typically considered less significant and can be neglected in this analysis (Mullin 2001). Under this assumption, and considering a size-independent growth rate, the PBE eq. 2.1 is reduced as follows:

$$\frac{\partial f_i(t,L)}{\partial t} = -G_i(S,T)\frac{\partial f_i(t,L)}{\partial L} \qquad i = 1,2 \tag{3.2}$$

To effectively solve equation (3.2), it is essential to establish both initial and boundary conditions.

The initial conditions are as follows:

$$f_1(t=0,L) = f_{seeds} \qquad for\ S > 1 \tag{3.3}$$

$$f_2(t=0,L) = 0 \qquad for\ S > 1 \tag{3.4}$$

$f_{seeds}$ denotes the size distribution of the seed crystals of the target enantiomer. This is an important factor as it provides a starting point for the crystallization process, particularly when seed crystals are used to initiate the process. For the counter enantiomer, the initial number density function, $f_2$, is set to zero. This is because the model considers only primary nucleation for the counter enantiomer, implying that there are no initial seed crystals for this enantiomer in the system. In the context of this model, the formation of new crystals through nucleation is incorporated as a boundary condition at the smallest crystal size, specifically at $L = 0$, as described in eq. 3.5.

$$f_i(t, L = 0) = \frac{B_i(S,T)}{G_i\,(S,T)} \qquad i = 1{,}2 \qquad for\ S > 1 \tag{3.5}$$

In simulations of seeded PC experiments, it is often assumed that the seed crystals can be described by a perfect log-normal distribution, as outlined in eq. 3.6. This distribution is characterized by $\mu$ which represent a mean value of logarithms of $L$, and a standard deviation, $\sigma$.

$$f_{seeds}(L) = \frac{A_{seeds}}{L\sigma\sqrt{2\pi}} \exp\left[-\frac{1}{2}\left(\frac{\ln \mathrm{L} - \mu}{\sigma}\right)^2\right] \tag{3.6}$$

The log-normal distribution is intrinsically normalized, meaning it integrates to unity over its entire range. To align this distribution with the specific mass of seed crystals in the experiment, denoted as $m_{seeds}$, it is scaled appropriately using eq. 3.7. This scaling ensures that the initial size distribution of seed crystals in the model accurately reflects their mass in the physical system being simulated, allowing for a more accurate and representative analysis of the crystallization process.

$$A_{seeds}(L) = \frac{m_{seeds}}{k_v \rho_{solid} \int_0^\infty L^3 f_{seeds}(L) dL} \tag{3.7}$$

Where, $k_v$ is a volume shape factor and $\rho_{solid}$ is the density of the solid phase.

### 3.1.2. Mass balance of the continuous phase

The PBE is closely connected with the continuous phase, primarily through factors like supersaturation and the concentration of the solute. According to (Myerson 2002), this connection is demonstrated by the fact that the rate at which solute mass exits the liquid phase is balanced by the rate at which it accumulates in the solid phase. The accumulation of the mass of enantiomer $i$ in the liquid phase, $m_{L,i}$, is calculated by the following mass balance:

$$\frac{dm_{L,i}}{dt} = \dot{m}_{L,i}^{in} - \dot{m}_{L,i}^{out} - \dot{m}_{L,i}^{cryst} \qquad i = 1{,}2 \tag{3.8}$$

The mass consumed due to crystal growth, $\dot{m}_{L,i}^{cryst}$, depends on the changes in the third moment of the particle size distribution. In simpler terms, this third moment is a measure that incorporates the size and number of particles, reflecting how mass is distributed across different particle sizes in the system. Hence, for a polythermal batch PC, the formulation of the mass balance eq. 3.8 can be rewritten as:

$$\frac{dm_{L,i}}{dt} = -3k_v\rho_{solid}G_i(S,T)\int_0^\infty L^2 f_i(t,L)dL \qquad i = 1,2 \qquad 3.9$$

Where, $k_v$ is a volume shape factor, $\rho_{solid}$ is the density of the solid phase and $G_i$ is the size independent growth rate.

To solve eq. 3.9, initial conditions are given as follow:

$$m_{L,i}(t=0) = m_{L,i}^0 \qquad i = 1,2 \qquad 3.10$$

Here, $m_{L,i}^0$ is the initial mass of each enantiomer $i$ dissolved in the liquid phase.

### 3.1.3. Kinetic rate equations

The phase separation that occurs in crystallization is a complex process, but it can be simplified using semi-empirical equations. Our main interest lies in the broader, macroscopic process, so initially, there's no need to investigate into highly detailed physical modeling (Mersmann 2001). Instead, we use combined parameters in the kinetic equations. These parameters summarize the overall effects of the process, which can be conveniently measured and understood through basic experiments.

In the case of seeded crystallization, where crystallization is initiated using pre-existing crystals, growth is the primary kinetic effect. This growth typically varies according to various growth models as discussed in previous chapter's section 2.2.3. However, for the purpose of simplification, the dispersion in growth rates and the effects of growth that depend on the size of the crystals are often overlooked. This approach simplifies the modelling process by avoiding the complexities in growth rates. Under these simplified conditions, the crystal growth rate, denoted as $G$, can be described using a power law as illustrated in eqs. 2.12 and 2.13. This power law is a mathematical relationship that describes how the growth rate changes with supersaturation.

Nucleation is the process responsible for the formation of new particles in crystallization. When the system experiences moderate levels of supersaturation, secondary nucleation typically becomes more dominant than primary nucleation. Secondary nucleation occurs due to the influence of existing crystals in the solution, as opposed to primary nucleation, which happens spontaneously without the presence of any seed crystals. The relationship between secondary nucleation and supersaturation is also described using a power law:

$$B_{sec,i} = k_{bsec,i}(S_i - 1)^{b_{sec.i}}(\mu_{3,i})^{n_{sec,i}} \qquad i = 1,2 \tag{3.11}$$

where:

- $k_{bsec,i}$ is the secondary nucleation rate coefficient,
- $S_i$ is supersaturation,
- $b_{sec.i}, n_{sec,i}$ are the model exponents,
- $\mu_{3,i}$ is the third moment (explained in the later section of this chapter)

In addition to the influence of supersaturation, secondary nucleation is typically assumed to increase with the presence of a larger quantity of existing crystals in the system. This relationship is accounted by including the third moment in the model, which represents the total volume or mass of the crystals in the system. Essentially, this term reflects the idea that the more crystals there are in the system, the higher the likelihood of secondary nucleation occurring. Therefore, secondary nucleation is depending on the presence of a solid phase – it can only take place if there are already crystals in the system. This means that for an unseeded enantiomer, where no solid phase is initially present, secondary nucleation starts at zero.
Furthermore, the secondary nucleation coefficient, denoted as $k_{bsec,i}$, is typically assumed to be influenced by temperature. It can affect the solubility and supersaturation levels, which in turn influence nucleation rates. Similar to eq. 2.11, effects of temperature on secondary nucleation can be addressed by an Arrhenius equation with activation energy $E_{Ab,i}$:

$$k_{bsec,i} = k_{bsec0,i} \exp(-\frac{E_{Ab,i}}{RT}) \qquad i = 1,2 \tag{3.12}$$

At higher levels of supersaturation, primary nucleation becomes a significant mechanism in the crystallization process. This form of nucleation leads to the direct formation of particles from the solution, without the need for pre-existing crystals to act as a catalyst. This is particularly relevant for the unseeded enantiomer in a system, which eventually transitions to the solid phase through primary nucleation when the solution reaches a sufficiently high level of supersaturation.

The equation used to model this primary nucleation process is described in classical nucleation theory. This theory provides a framework for understanding how and when new particles form in a supersaturated solution. The adaptation of the original model for primary nucleation, as described in (Mersmann 2001), offers a more tailored approach to crystallization processes involving specific compounds or conditions. The detailed derivation and application of this adapted model can be found in the work of (Elsner et al. 2011). The overall primary nucleation rate is given by:

$$B_{prim0,i}(t) = k_{bprim1}\, T_L(\mathrm{t}) \exp\left(-\frac{K_{Tv}}{T_L(t)}\right) exp\left(-\frac{\sum_i w_{L,i}(t)}{K_{wv}}\right) \sqrt{ln\left(\frac{\rho_s}{C_{L,eq,i}(T)}\right)} \tag{3.13}$$

$$\left(S_i(t)\, C_{L,eq,i}(T)\right)^{7/3} exp\left(k_{bprim2}\left(ln\left(\frac{\rho_s}{C_{L,eq,i}(T)}\right)\right)^3 \frac{1}{ln\left(S_i(t)\right)^2}\right) \qquad i = 1{,}2$$

During the process of parameter estimation studies, it was discovered that eq. 3.13 did not adequately replicate the nucleation events observed in experimental settings. This indicated the need for a more comprehensive approach to accurately model the primary nucleation rate. Thus, adjustments or additional considerations were incorporated into the overall primary nucleation rate model results in eq. 3.14 (Eicke 2016).

$$B_{prim,i} = B_{prim0,i}\left(1 + M_{prim}\left(\mu_{2,i}\right)^{n_{prim,i}}\right) \qquad i = 1{,}2 \qquad 3.14$$

In the context of preferential crystallization, an additional term was included in the above equation to account for the role of the seeded enantiomer in catalysing the primary nucleation of the unseeded enantiomer. This additional term considers the fact that the seeded enantiomer provides a significant heterogeneous surface area, which can act as a catalyst for the nucleation of the unseeded enantiomer. This influence is quantified by including the second moment, denoted as $\mu_{2,i}$, in the equation. The second moment is a measure of the total crystal surface area available in the system. The larger this surface area, the greater the potential for it to catalyse nucleation. The parameter $M_{prim}$ in this additional term acts as a magnitude of the gain factor, determining the extent of the seeded enantiomer's influence on the primary nucleation of the unseeded species. Another parameter$n_{prim,i}$, is included to account for any non-linear relationships in this process. The total rate of nucleation, $B_i$, is then defined as the sum of the rates from equations 3.11 and 3.14. This combined rate is used in the boundary condition of the Population Balance Equation (PBE) as specified in eq. 3.5.

## 3.2. Driving force calculations

In preferential crystallization (PC), the driving force is fundamentally derived from the differences in concentrations between the current state of the process and the equilibrium state. This driving force is crucial as it determines the rate and extent of the crystallization process. As discussed in section 2.1.1, the supersaturation, denoted as $S_i$, is a key metric for quantifying this driving force. Supersaturation essentially measures how much more of a substance is present in the solution compared to what can be dissolved at equilibrium. It is often expressed as a ratio of mass fractions, as indicated in eqs. 2.2 and 2.3.

The supersaturation of each enantiomer, denoted as $i$, is a dynamic variable that changes during the crystallization process due to the depletion of the enantiomer's concentration in the liquid phase. This change is a critical aspect to consider when quantifying preferential crystallization (PC), using any type of modelling strategy. The key to accurately quantifying

supersaturation lies in the correct formulation of the saturation mass fractions, $w_{sat,i}$, for each enantiomer. These saturation mass fractions are determined based on solubility data, which are often represented in a ternary phase diagram (TPD).

In figure 3.1, the TPD for the system consisting of enantiomers 1 and 2 (or solvates 1' and 2') and the solvent (3) is illustrated. Within this diagram, the lines labelled AB and CB represent the solubility curves at the crystallization temperature for the target enantiomer and the counter enantiomer, respectively. Any concentration above these curves represents a supersaturated state, which is essential for the crystallization process to occur. The slope of the solubility curves is determined by the solubility ratio which is illustrated in eq. 2.4.

In figure 3.1, which illustrates the TPD for a system involving enantiomers and solvent, point O represents the starting composition of the PC process. The concentration at this point is determined by the racemate's solubility at the saturation temperature. The saturation mass fractions for the preferred enantiomer at the starting composition (figure 3.1 (a)) or at any time as the PC progress (along curve OB in figure 3.1 (b)), is found by calculating the intersection point of the solubility isotherm (e.g., line AB for the preferred enantiomer) and the line connecting the current liquid phase composition (O') with the corresponding pure enantiomer (point 1 in figure 3.1a and point 1’ in figure 3.1b). This approach also applies to the counter enantiomer. By following these steps, you can calculate the current saturation mass fractions for both enantiomers at different stages of the PC process. The method is applicable to systems forming anhydrous or solvated crystals, as shown in figure 3.1 (a) and (b). It can also be extended to systems characterized by curved solubility isotherms. To navigate these scenarios, specific transformations are used to correlate the concentrations of different components. These transformations involve converting the concentrations to coordinates in an equilateral triangle placed in a Cartesian plane, as illustrated in the figure. The formulas $X = \frac{1}{2}(1 - w_1 + w_2)$ and $Y = \frac{\sqrt{3}}{2}(1 - w_1 - w_2)$ and vice versa $w_1 = 1 - X - \frac{Y}{\sqrt{3}}$ , $w_2 = X - \frac{Y}{\sqrt{3}}$ and $w_3 = \frac{2Y}{\sqrt{3}}$, are derived from geometric considerations of this representation (Carneiro 2021; Cascella 2021; Shimura and Kemp 2015; Temmel et al. 2012).

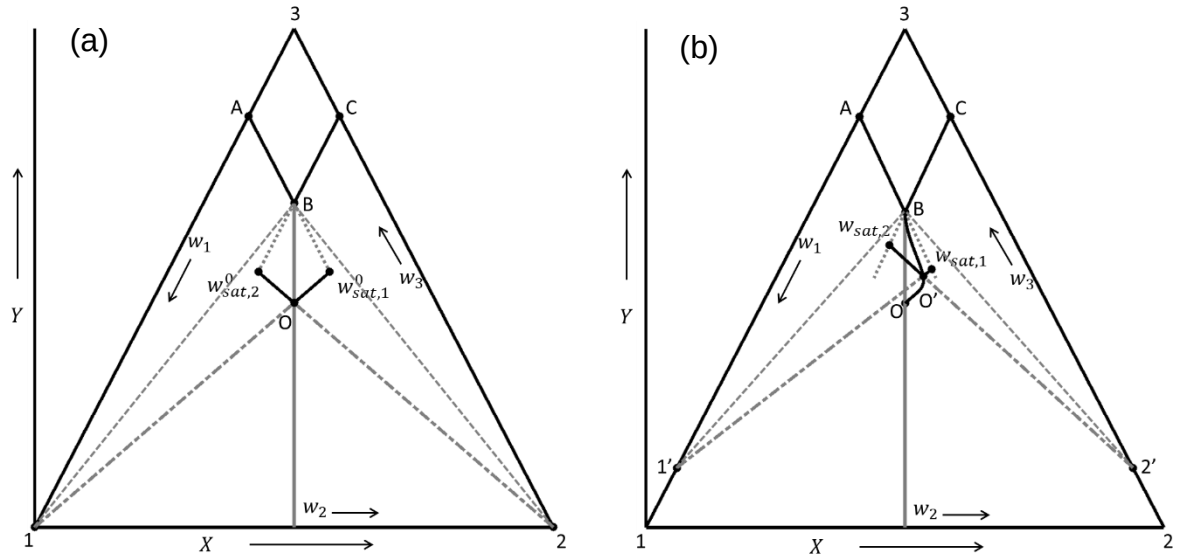


**Figure 3.1.** Ternary phase diagrams of conglomerates illustrating calculations of driving forces used in the SCM demonstrated (a) at starting point $O$ (lines $Ow_{sat,1}^0$ and $Ow_{sat,2}^0$) and (b) for solvated systems, at any process point $O'$ (lines $O'w_{sat_1}$ and $O'w_{sat_2}$). Points $1'$ and $2'$ are the respective solvated compounds of preferred and counter enantiomers. The driving force correspondent to each enantiomer at each time $t$ is calculated from the intersection between the line connecting pure phase corner ($1$, $2$, $1'$ or $2'$) and current state $O'$ (dash-dotted lines) and the metastable solubility (dotted lines) (Coquerel 2015; Jacques et al. 1994; Temmel et al. 2018).

## 3.3. Numerical techniques for solving PBE

PBE are often complex and can only be solved analytically in simplified cases. As a result, numerical methods are typically required for most practical applications. This necessity has led to a significant focus in research on developing accurate and efficient numerical solutions for PBEs. These methods involve discretizing the equations and solving them iteratively, which can be computationally intensive but allows for handling the complexity of PBEs in a manageable way. The work of (Ramkrishna 1985, 2000), highlights the importance and development of these numerical techniques. His research provides valuable insights into the methodologies for approaching PBEs, emphasizing both the accuracy and computational efficiency of the solutions.

### 3.3.1. Method of Moments

Alternatively, reduction techniques such as the Method of Moments (MOM), introduced by (Hulburt and Katz 1964), serves as an effective method for solving PBEs. While PBEs provide a detailed particle size distribution, MOM simplifies this by allowing the calculation of representative terms that describe a particle size distribution more generally, such as average values and total quantities. One of the key advantages of the Method of Moments is its ability

to streamline the complexity inherent in PBEs. Instead of dealing with the full distribution of particle sizes, MOM focuses on certain key characteristics of the distribution, like mean particle size or total particle number. This approach reduces the computational load and complexity while still providing essential insight into the system. Additionally, MOM can help resolve potential issues of dimension incongruence that may arise between PBEs and transport equations (Randolph and Larson 1988).

The $j^{th}$ moment of the distribution for a given enantiomer $i$, in the context of population balance equations, is mathematically defined as:

$$\mu_{j,i} = \int_{L=0}^{\infty} L_i^j f_i(L,t) dL \qquad i = 1,2 \qquad 3.15$$

In this equation, $f_i(L,t)$ represents the number density distribution function of the population of crystals of enantiomer $i$ at time $t$ and $L$ is a variable representing a characteristic length. The term $L^j$ is the moment order, and the integral computes the moment over all possible sizes.

Each of the first four moments of this distribution has a distinct physical meaning:

- $\mu_{0,i}$: This represents the total number of crystals in the system. It's a dimensionless quantity and gives a count of how many individual crystals are present.

- $\mu_{1,i}$: This is the cumulative length of all crystals, measured in meters (m). It sums up the lengths of each crystal to give a total length value.

- $\mu_{2,i}$: This moment calculates the total surface area of all crystals, in square meters ($m^2$). It's an indication of the combined surface area presented by all crystals in the system.

- $\mu_{3,i}$: This reflects the combined volume of all crystals, measured in cubic meters ($m^3$). It aggregates the volumes of individual crystals to give a total volume.

Higher moments, beyond the third, become more challenging to interpret physically. However, they can be crucial for reconstructing the complete crystal size distribution. This reconstruction is useful for understanding the detailed characteristics of the crystal population in the system (Qamar et al. 2008).

Based on eq. 3.15 and PBE given in eq. 3.2, one can derive a set of ODEs. This process involves multiplying the PBE by the $j^{th}$ power of the size coordinate $L$ and then integrating this product over the semi-infinite interval $[0, \infty)$. The expression can be written as:

$$\int_0^\infty L_i^j \frac{\partial f_i(t,L)}{\partial t} dL = -G_i(S,T) \int_0^\infty L_i^j \frac{\partial f_i(t,L)}{\partial L} dL \qquad i = 1,2 \tag{3.16}$$

According to Leibnitz's rule for differentiating under the integral sign, the order of integration and differentiation on the left-hand side of eq. 3.16 can be reversed since the integration limits are constant and do not depend on time. This allows the differentiation with respect to time $dt$ to be taken outside of the integral, leading to the resulting expression:

$$\frac{d}{dt} \int_0^\infty L_i^j f_i(t,L)\, dL = \frac{d\mu_{j,i}}{dt} \qquad i = 1,2 \tag{3.17}$$

Using integration by parts in case of the right-hand side of the eq. 3.16 gives:

$$G_i(S,T) \int_0^\infty L_i^j \frac{\partial f_i(t,L)}{\partial L} dL = G_i(S,T) \left( \left[ L_i^j f_i(t,L) \right]_0^\infty - \int_0^\infty j L_i^{j-1} f_i(t,L) dL \right) \; i = 1,2 \tag{3.18}$$

Given the regularity condition, which asserts that the number density function $f_i(t,L)$ approaches zero as $L_i$ approaches infinity, the combination of eqs. 3.16, 3.17, and 3.18 results in a set of ODEs for the first $j$ moments of the distribution. Eq. 3.19 and 3.20 represents this set of ODEs, which describes the evolution of these moments over time.

$$\frac{d\mu_{j,i}}{dt} = i\, G_i(S,T)\, \mu_{j-1,i} \qquad i = 1,2 \; and \; j = 1,2,3 \tag{3.19}$$

$$\frac{d\mu_{0,i}}{dt} = B_i \qquad i = 1,2 \tag{3.20}$$

### 3.3.2. Method of Characteristics

(Kumar and Ramkrishna 1997) made significant advancements in solving PBEs that include simultaneous nucleation, growth, and aggregation processes. They developed a unique approach by combining their discretization technique on a non-uniform grid, which was particularly effective for handling aggregation and breakage terms, combined with the Method of Characteristics (MOC) for quantifying growth . Typically, numerical techniques for solving PBEs can introduce errors known as numerical dissipation, particularly when discretizing growth terms. Numerical dissipation refers to the artificial reduction of the amplitude of the solution over time, which can lead to inaccuracies. However, Kumar and Ramkrishna found that the MOC helps avoid this specific error, making their approach more

accurate and reliable for modelling the growth process in crystallization. For handling the nucleation term, which is often challenging to model due to its dynamic nature and the typically small size of nuclei, they involved adding a cell of the nuclei size at a specific time level, effectively incorporating the nucleation process into their model. Building upon these concepts, (Lim et al. 2002) further expanded the methodology by applying high-resolution spatial discretization methods, specifically Weighted Essentially Non-Oscillatory (WENO) schemes, along with the MOC. They used these techniques for dynamic simulations of batch crystallization processes, which included the complexities of nucleation, growth, aggregation, and breakage kinetics.

### 3.3.3. Higher order resolution schemes

High-resolution numerical schemes, initially developed for gas dynamics, have been adapted for solving PBEs in various studies, such as those by (Gunawan, Fusman, and Braatz 2004; Ma, Tafti, and Braatz 2002; Qamar et al. 2007). These schemes are particularly beneficial for handling complex dynamics in crystallization processes, as they can solve one and two-dimensional PBEs with high accuracy. The main advantage of high-resolution schemes lies in their ability to achieve high-order accuracy even on coarser grids. This is especially valuable in simulations that require resolving sharp discontinuities, like sudden changes in particle size distributions in crystallization processes. By accurately capturing these discontinuities, these schemes help avoid numerical diffusion and dispersion which can cause unphysical oscillations in the solution, both of which are undesirable in accurate simulations. Another key strength of these high-resolution schemes is their general applicability. They can be used for a wide range of hyperbolic problems in conservation law form, without the need for detailed understanding of the physical characteristics specific to each problem. This makes them versatile tools for addressing a variety of complex systems, including those encountered in crystallization process modelling.

In this work, to solve PBE, we have used a model that was developed by (Qamar et al. 2006, 2008) for the preferential crystallization of enantiomers. This model has been further refined to account for both isothermal and non-isothermal conditions, enhancing its applicability to a wider range of crystallization scenarios. To solve the PBEs associated with this model, high-resolution numerical schemes have been employed. These include the scheme developed by (Koren 1993) and another by (LeVeque 2002). The chosen numerical schemes are characterized by their discrete nature in space while remaining continuous in time. This approach leads to the formulation of ODEs that describe the dynamics of the crystallization process over time. These ODEs are solved using ode45 in MATLAB (Mathworks M 2017).

As illustrated in eq. 3.2, the 1-D homogeneous PBE is given as:

$$\frac{\partial f_i(t,L)}{\partial t} = -G_i(S,T)\frac{\partial f_i(t,L)}{\partial L} \qquad i = 1,2 \tag{3.21}$$

To implement a finite volume scheme to solve PBEs, the internal property variable, denoted as $L$, is divided into $N$ subdivisions. This subdivision process is a critical step in the application of the finite volume method (FVM), as it helps in discretizing the continuous domain into discrete segments for numerical analysis. As illustrated in figure 3.2, for each cell index $k$ (where $k$ = 1, 2….,$N$), and given a cell width $\Delta L$, the cell centers are defined as $L_k$. Additionally, the cell faces are represented by the points $L_{k\pm1/2}$, which are calculated as $L_k \pm \frac{\Delta L}{2}$.

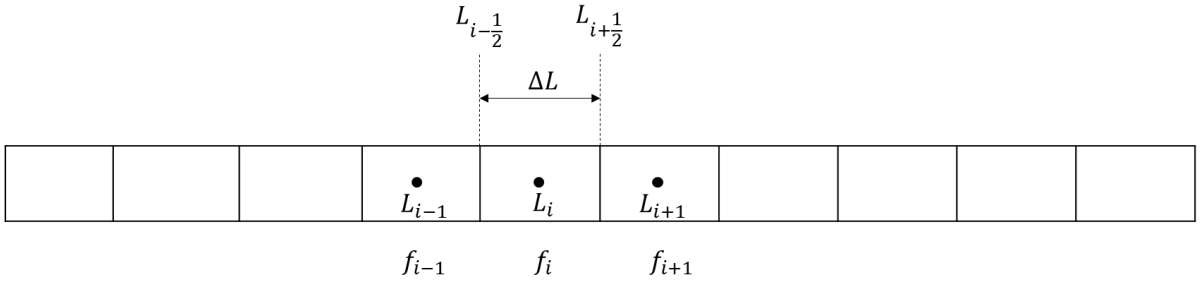


**Figure 3.2.** Cell centered finite volume grid

Eq. 3.21 can be rearranged as:

$$\int_{L_{k,i}^-}^{L_{k,i}^+} \frac{\partial f_{k,i}(t,L)}{\partial t}\partial L = -G_{k,i}(S,T)\left(f_{L_{k,i}^+} - f_{L_{k,i}^-}\right) \quad i = 1,2\ and\ k = 1,2\ldots.,N \qquad 3.22$$

First order accurate upwind scheme is obtained by taking the backward difference. In order to preserve the number, the population at the $k^{th}$ number is equal to the positive face of the $k^{th}$ section and the population at the $(k-1)^{th}$ number is equal to the negative face of the $k^{th}$ section.

$$f_{L_{k,i}^+} = f_{L_{k,i}} \ , \ f_{L_{k,i}^-} = f_{L_{k,i-1}} \qquad i = 1,2\ and\ k = 1,2\ldots.,N \qquad 3.22$$

Higher order accuracy is obtained by piecewise polynomial interpolation:

$$f_{L_{k,i}^+} = \left(f_{k,i} + \frac{1+m}{4}(f_{k+1,i} - f_{k,i}) + \frac{1-m}{4}(f_{k,i} - f_{k-1,i})\right) \quad i = 1,2\ and\ k = 1,2\ldots.,N \qquad 3.23$$

Similarly,

$$f_{L_{k,i}^-} = \left(f_{k-1,i} + \frac{1+m}{4}(f_{k,i} - f_{k-1,i}) + \frac{1-m}{4}(f_{k-1,i} - f_{k-2,i-1})\right) \quad i = 1,2\ and\ k = 1,2\ldots.,N \qquad 3.24$$

For all other values of $m \in [-1, 1]$, a weighted blend is obtained between the central scheme and the fully one-sided upwind scheme (van Leer, Leer, and B. 1985). Similar to (Qamar et al. 2006), we also used $m$ = 1/3 for our calculations. It reduces eq. 3.23 and 3.24 to following:

$$f_{L_{k,i}^{+}} = \left( f_{k,i} + \frac{1}{2}\left(\frac{1}{3} + \frac{2}{3} r_k^{+}\right)\left(f_{k,i} - f_{k-1,i}\right)\right) \qquad i = 1,2 \; and \; k = 1, 2 \ldots., N \tag{3.25}$$

Similarly,

$$f_{L_{k,i}^{-}} = \left( f_{k-1,i} + \frac{1}{2}\left(\frac{1}{3} + \frac{2}{3} r_k^{-}\right)\left(f_{k-1,i} - f_{k-2,i}\right)\right) \quad i = 1,2 \; and \; k = 1, 2 \ldots., N \tag{3.26}$$

The terms $r_k^{+}$ and $r_k^{-}$ of this function are upwind ratios which is given as:

$$r_k^{+} = r_k = \frac{n_{k+1} - n_k + \epsilon}{n_k - n_{k-1} + \epsilon} \tag{3.27}$$

$$r_k^{-} = r_{k-1} = \frac{n_k - n_{k-1} + \epsilon}{n_{k-1} - n_k + \epsilon} \tag{3.28}$$

This expression has to be evaluated with a small parameter $\epsilon = 10^{-10}$ to avoid division by zero (Koren 1993).

Higher order accuracy in numerical methods, particularly in the context of interpolation in finite volume schemes, can significantly enhance the efficiency and precision of the calculations. However, a notable drawback of higher order schemes is their tendency to induce vibrations or oscillations at the interfaces or faces of the grid. These oscillations can lead to inaccurate results, especially around sharp gradients or discontinuities in the solution. To mitigate this issue, a technique known as a "flux limiter" is often employed. Flux limiters are designed to reduce these unwanted vibrations at the cell faces by adaptively modifying the numerical scheme. Essentially, they allow the equation to switch from a higher order scheme to a lower (usually first) order scheme in regions where oscillations are likely to occur. In eqs. 3.25 and 3.26, $\left(\frac{1}{3} + \frac{2}{3} r_k^{+}\right)$ is replaced by $\emptyset(r_k^{+})$ and $\left(\frac{1}{3} + \frac{2}{3} r_k^{-}\right)$ is replaced by $\emptyset(r_k^{-})$. Where $\emptyset(r_k)$ is a flux limiter which is given by (Koren 1993) and illustrated in eq. 3.29 and 3.30.

$$\emptyset(r_k^{+}) = \max\left( 0, \min\left(2r_k^{+}, \min\left(\frac{1}{3} + \frac{2}{3} r_k^{+}, 2\right)\right)\right) \tag{3.29}$$

Similarly,

$$\emptyset(r_k^-) = \max\Big(\ 0, \min\Big(2r_k^-, \min\Big(\frac{1}{3}+\frac{2}{3}r_k^-, 2\Big)\Big)\Big) \tag{3.30}$$

Substituting eqs. 3.25, 3.26, 3.27, 3.28, 3.29, 3.30 in eq. 3.22, we get:

$$\frac{df_{k,i}}{dt} = -\frac{G_i}{\Delta L}\Bigg(\Big(f_{k,i} + \frac{1}{2}\emptyset(r_k)\big(f_{k,i} - f_{k-1,i}\big)\Big) - \Big(f_{k-1,i} + \frac{1}{2}\emptyset\big(r_{k-1,i}\big)\big(f_{k-1,i} - f_{k-2,i}\big)\Big)\Bigg) \tag{3.31}$$
$$i = 1{,}2 \; and \; k = 1, 2 \ldots., N$$

For second order accuracy and $S_i > 1$, the PBE in eq. 3.22 can be discretised as follow:

$$For\ k = 1 \qquad \frac{df_{1,i}}{dt} = -\Big(\frac{G_i * f_{1,i} - B_i}{\Delta L}\Big) \qquad i = 1{,}2 \tag{3.32}$$

$$For\ k = 2 \qquad \frac{df_{2,i}}{dt} = -\Big(\frac{f_{2,i} - f_{1,i}}{\Delta L}\Big) \qquad i = 1{,}2 \tag{3.33}$$

$$For\ k = 3, 4..N \qquad \frac{df_{k,i}}{dt} = -\frac{G_i}{\Delta L}\Bigg(\Big(f_{k,i} + \frac{1}{2}\emptyset(r_k)\big(f_{k,i} - f_{k-1,i}\big)\Big) - \Big(f_{k-1,i} + \frac{1}{2}\emptyset\big(r_{k-1,i}\big)\big(f_{k-1,i} - f_{k-2,i}\big)\Big)\Bigg) \quad i = 1{,}2 \tag{3.34}$$

In order to solve the ODEs given in eq. 3.32 - 3.34, following boundary conditions are used:

$$f_1(t = 0, L) = f_{seed}(L) \tag{3.35}$$

$$f_2(t = 0, L) = 0 \tag{3.36}$$

$$f_{i,0}(t, L = 0) = \frac{B_i}{G_i} \qquad i = 1{,}2 \tag{3.37}$$

$$f_{i,N}(t, L \to \infty) = 0 \qquad i = 1{,}2 \tag{3.38}$$

$$\emptyset(t, L \to \infty) = 1 \tag{3.39}$$

## 3.4. Performance criteria for process evaluation

For evaluating isothermal batch preferential crystallization (PC), productivity is a crucial Key Performance Indicator (KPI). It provides valuable insights into the efficiency of the process, making it a useful tool for process design and comparison with other crystallization alternatives. The productivity in this setting is defined by the following equation:

$$Pr = \frac{m_{s,1}(t_{stop}) - m_{seeds}}{\left(t_{stop} + t_{dead}\right) V_L} \quad 3.40$$

In this expression:

- $m_{s,1}(t_{Stop})$ represents the mass of the solid product (the target enantiomer) obtained at the stop time ($t_{Stop}$) of the batch.
- $m_{seeds}$ is the mass of the seed crystals used in the process.
- $t_{Stop}$ is the time at which the crystallization batch process is stopped.
- $t_{dead}$ is the dead time, which includes additional time necessary for preparation and cleaning of the equipment. In this study, $t_{dead}$ is assumed to be 1.0 hour.
- $V_L$ denotes the total volume of the liquid phase in which the crystallization occurs.

The productivity formula calculates the mass of solid product obtained per unit volume per batch time, including the dead time.

In PC, another important KPI is the process yield, which is defined as:

$$Yield = \frac{m_{s,1}(t_{stop}) - m_{seeds}}{m_{s,1,max}} \quad 3.41$$

The $Yield$ for PC is a crucial measure of process efficiency. It measures the proportion of the maximum possible product that is actually produced in a batch. This KPI is essential for assessing how effectively the process converts raw materials into the desired product. A high yield implies minimal waste and efficient use of resources. For PC, It is defined in terms of the mass of the product crystallized, specifically the final mass of the solid target enantiomer $m_{s,1}(t_{stop})$ after subtracting the mass of the seed crystals $m_{seeds}$, relative to $m_{s,1,max}$which is the maximum amount of solid product that could theoretically crystallize within a given temperature range. Eq. 3.42 formulates:

$$m_{s,1,max} = \left(w_1^0 - w_{sat,1}\right) m_{tot}^0 \quad 3.42$$

In this equation:

- $w_1^0$ is the concentration of the racemic mixture at the initial state.
- $w_{sat,1}$ is the concentration of the racemic mixture at the saturation state.
- $m_{tot}^0$ represents the initial total mass.

The yield thus calculates the efficiency of the crystallization process in converting the available racemic mixture into the desired solid product at specific temperatures.

Purity is another KPI in the design and evaluation of crystallization processes. It is defined as:

$$Pu = \frac{m_{s,1}(t_{stop})}{m_{s,1}(t_{stop}) + m_{s,2}(t_{stop})} * 100\ \% \qquad 3.43$$

In this equation:

- $m_{s,1}(t_{stop})$ is the mass of the solid target enantiomer at the end of the batch process ($t_{stop}$).
- $m_{s,2}(t_{stop})$ is the mass of the solid counter enantiomer at the same time ($t_{stop}$).

Purity, therefore, measures the proportion of the target enantiomer in the total solid product obtained, indicating the effectiveness of the process in selectively crystallizing the desired enantiomer.

Together, these KPIs provide a comprehensive overview of the PC process. They help in identifying areas for improvement, optimizing process conditions, and making informed comparisons with alternative methods. By monitoring and aiming to improve these KPIs, we can develop more efficient, cost-effective, and high-quality crystallization processes.

# 4. Shortcut Model (SCM) for PC quantification

The Shortcut Model (SCM) introduced in this chapter is a simple yet effective depiction of different variants of isothermal PC process for conglomerate forming systems. It provides a pre-screening tool to quickly evaluate PC's KPIs for a given model compound before applying complex population balance models. Further innovation includes extending SCM adaptability to continuous PC with dimensionless parameters and addressing PC's inherent yield limitation by integrating a racemization reaction, aiming for full utilization of enantiomers and maximizing process productivity.

## 4.1. SCM for batch PC

In this section, we introduce a straightforward shortcut model (SCM) for evaluating the efficiency of batch preferential crystallization. This model is based on the mass balances and metastable solubilities derived from Ternary Phase Diagrams (TPD). The application of the model is focused on isothermal preferential crystallization (PC) of conglomerate forms. The subsequent section outlines the underlying assumptions of the model and outlines a method to deduce its parameters with a minimal experimental dataset. Moreover, we recommend a model extension that incorporates temperature variations, substantiated by empirical findings from the second case study. Essential details provided in this section are already published in (Carneiro et al. 2019)

### 4.1.1. Assumptions of SCM

The SCM for batch PC process introduced in this section. It exploits the principle of “total mass transfer” causing mass depletion of the solute in the liquid phase and mass build-up of the solid phase. In order to derive the model, we have made the following assumptions and compared it with the more detailed population balance model (PBM).

#### I. Size and shape of particles

All crystals of one enantiomer are identical and distributed over one mean size (left plot of figure 4.1). The shape of crystals is spherical and grow by the same rate. In PBM, we consider a poly-dispersed distribution of particles (right plot of figure 4.1).

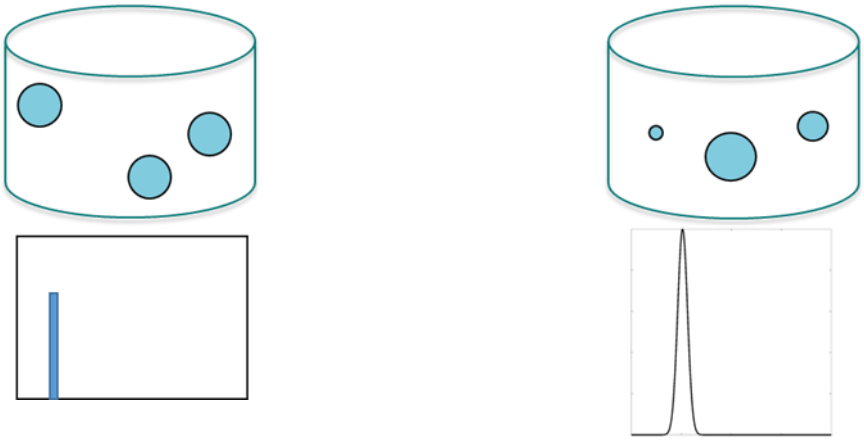

Shortcut Model Population Balance Model

**Figure 4.1**. Illustration of shape and size of particles in SCM and PBM

### II. Lumping of nucleation and growth mechanisms

The mass transfer from nucleation and growth rates are lumped together and considered as a total mass transfer of solute from liquid to solid phase. Nucleation does not produce any new particles and the connected mass transfer is accounted in the growth of the existing particles (left plot of figure 4.2). There is no clear distinction between mass transfer steps and surface integration. In PBM, nucleation and growth are considered as two separate mechanisms. Nucleation produces new particles and growth is responsible to grow the particles (right plot of figure 4.2).

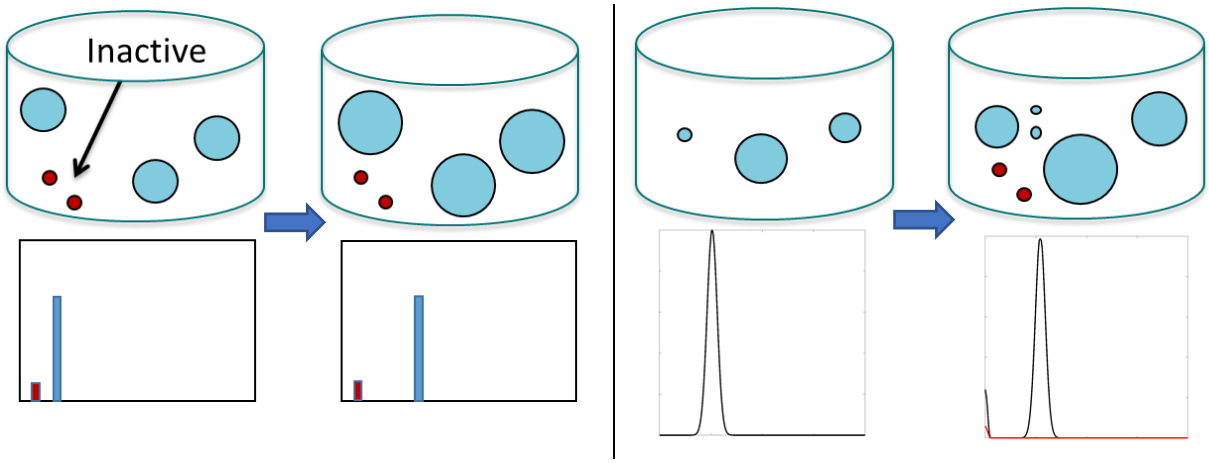


Shortcut Model Population Balance Model

**Figure 4.2**. Illustration of nucleation and growth of particles in SCM and PBM

### III. Crystals of counter-enantiomers

As there are no production of new crystals, to account the influence of counter enantiomer, we assume that very tiny crystals of counter enantiomers are initially present below a threshold of contamination (left plot of figure 4.3). These particles have no influence on the process until the stop time (see point IV). In PBM, we have a separate sub model for the nucleation of counter enantiomer and thus counter enantiomers are not initially present (right plot of figure 4.3). It only appears at the induction time of the counter enantiomers.

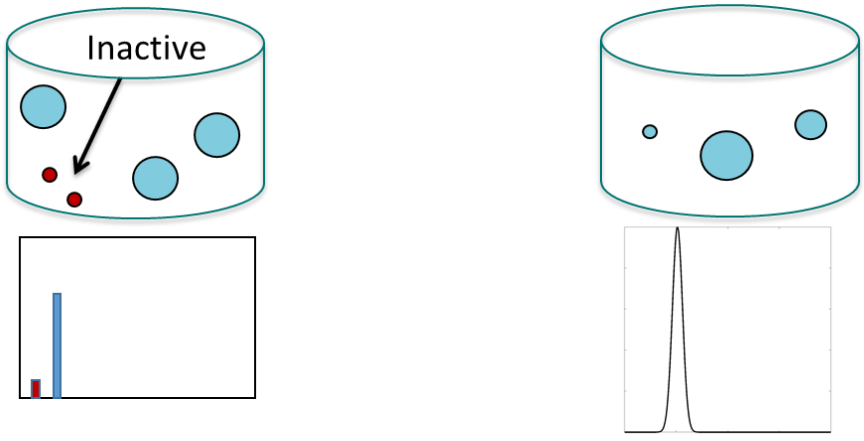


Shortcut Model

Population Balance Model

**Figure 4.3**. Illustration of initial counter enantiomer particles in SCM and PBM

### IV. Stop time ($t_{stop}$)

The growth of initially present counter enantiomer crystals activated at the stop time ($t_{stop}$) (left plot of figure 4.4). At this point, the contamination of the solid phase starts and the process needs to stop based on the purity requirements. This is a very crucial parameter and one needs to perform systematic PC experiments to estimate a correct value. In PBM, there are separate sub-models determine the nucleation of both enantiomers (right plot of figure 4.4).

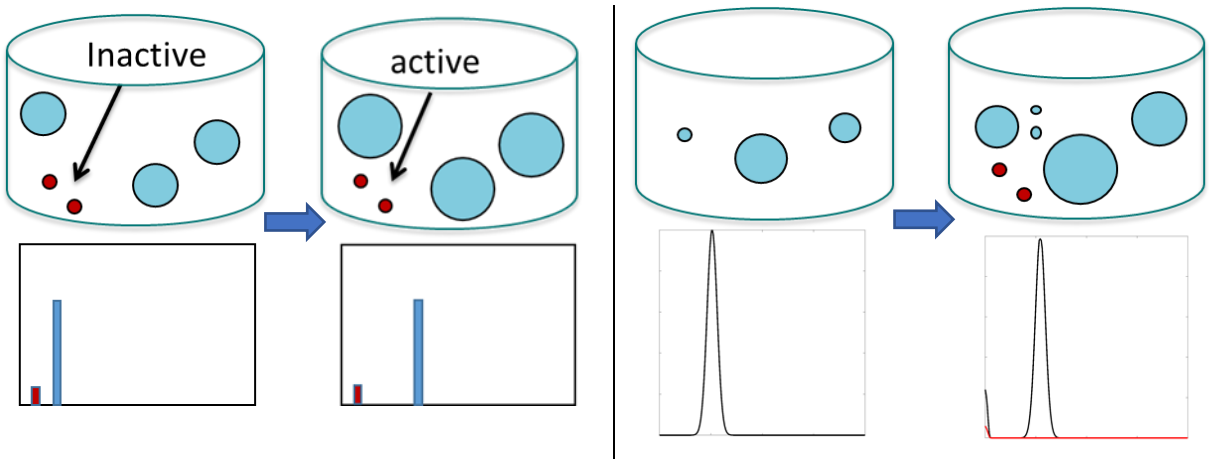


Shortcut Model

Population Balance Model

**Figure 4.4**. Illustration of induction time in SCM and PBM

### V. Total number of crystals

We do not consider agglomeration and breakage mechanisms in the process. There is no production or elimination of the particles in the entire process. It means that the total number of crystals in the beginning of the process is same as the total crystals at the end of the process (left plot of figure 4.5). In PBM, the total number of crystals varies on the various mechanisms considered in the process (right plot of figure 4.5). For example, nucleation, agglomeration and breakage may lead to addition of new crystals whereas dissolution, agglomeration and breakage may lead to removal of the existing crystals during the process.

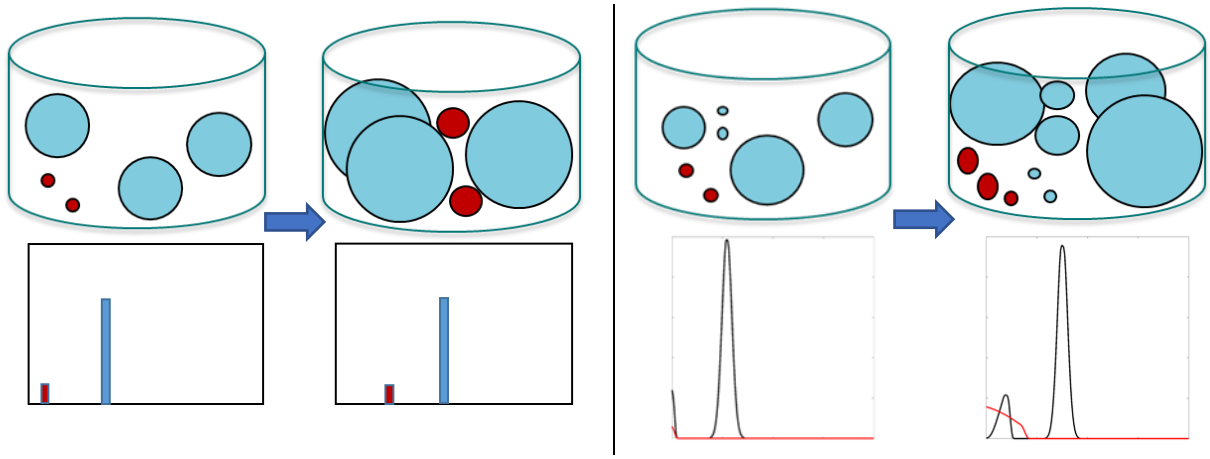

Shortcut Model

Population Balance Model

**Figure 4.5**. Illustration of total number of particles in SCM and PBM

## 4.1.2. Quantification and illustration of SCM

The shortcut model balances a ternary system with preferred enantiomer (index 1), counter enantiomer (index 2) dissolved in a solvent (index 3). The mass depletion of the solvent in the liquid phase is equal to the gain in the total solid mass during the batch PC process. The mass change in the liquid phase ($m_i$) and solid phase ($m_{Si}$, a function of the solid density $\rho_S$ and volume of solids $V_{Si}$) are quantified with the effective mass transfer rate ($\overline{GB}^{eff}$) caused by the combined effect of nucleation and growth of crystals.

The changes in the masses of liquid and solid phases for both enantiomers hold

$$\frac{dm_i}{dt} = -\overline{GB}_i^{eff} \quad i \in \{1,2\} \tag{4.1}$$

$$\frac{dm_{S_i}}{dt} = \rho_S \frac{dV_{S_i}}{dt} = \overline{GB}_i^{eff} \quad i \in \{1,2\} \tag{4.2}$$

The overall mass transfer rate from liquid to solid phase is explained by SCM for each enantiomer $i$ using the following equation:

$$\overline{GB}_i^{eff} = k^{eff} 4\pi N_i R_i^2 \, (S_i - 1)^{n^{eff}} \quad i \in \{1,2\} \tag{4.3}$$

The effective mass transfer rate (eq. 4.3) comprises of three terms: an effective mass transfer constant ($k^{eff}$); the total surface area of all crystals, where $N_i$ is the total number of spherical crystals of radius $R_i$; and a driving force term, a function of supersaturation $S_i$ and order of crystallization $n^{eff}$. A systematic approach to quantify driving force for PC process is already explained in chapter 3.2.

The transients of the both enantiomers in liquid and solid phase are described by a system of ordinary differential equations (ODEs). Eqs. 4.1 to 4.3 are rearranged for the crystals with the same radius ($R_i$), offering eqs. 4.4 to 4.8.

Liquid phase mass balances:

$$\frac{dm_1}{dt} = -k^{eff} 4\pi \, N_1 R_1^2 (S_1 - 1)^{n^{eff}} \tag{4.4}$$

$$\frac{dm_2}{dt} = -F_2 \, k^{eff} 4\pi \, N_2 R_2^2 (S_2 - 1)^{n^{eff}} \tag{4.5}$$

$$\frac{dm_3}{dt} = -\left(k^{eff} 4\pi \, N_1 R_1^2 (S_1 - 1)^{n^{eff}} + F_2 \, k^{eff} 4\pi \, N_2 R_2^2 (S_2 - 1)^{n^{eff}}\right)\left(\frac{M_S}{M_i} - 1\right) \tag{4.6}$$

Solid phase mass balances:

$$\frac{dR_1}{dt} = \frac{k^{eff}}{\rho_S} (S_1 - 1)^{n^{eff}} \tag{4.7}$$

$$\frac{dR_2}{dt} = F_2 \, \frac{k^{eff}}{\rho_S} (S_2 - 1)^{n^{eff}} \tag{4.8}$$

A crucial parameter of the model is the contamination factor of the counter enantiomer

$$F_2 = \begin{cases} 0, & t < t_{stop} \\ 1, & t \geq t_{stop} \end{cases} \tag{4.9}$$

The stop time ($t_{stop}$) is introduced in eqs. 4.5, 4.6 and 4.8 by using contamination factor $F_2$. It activates the crystallization of the counter enantiomers. As explained in assumptions III and IV, very small crystals of counter enantiomers are initially present but they are inactive until $t_{stop}$. Therefore, in order to avoid deterioration of the product purity, batch PC process should be stopped at $t_{stop}$. In case of enantiomers that crystallizes as a hydrate (or solvate), the mass balance of the solvent is given by eq. 4.6. The change in the mass of solvent in the liquid phase is proportional to the ratio of the molar mass of the solid solvate $M_S$ and the nonsolvate enantiomer $M_i (i \in \{1,2\})$. For the processes defined at product purity specification of 100%, only three ODEs eqs. 4.4, 4.6 and 4.7 are required to describe the initial production phase of PC until stop time. In this work, this time interval is used for parameter estimation and process modeling. The contamination phase after $t_{stop}$ is illustrated with the help of eqs. 4.5 and 4.8 but without the purpose of matching the real system. Hence, stop time is considered as a "switch parameter" to activate the equations enabling the influence of counter enantiomers to approximate the model in contamination phase for purity < 100%.

In order to solve the ODEs, the following initial conditions are required for both liquid and solid phase.

liquid phase:

$$m_i(t=0) = m_i^0 \qquad i \in \{1,2,3\} \tag{4.10}$$

Solid phase:

$$m_{S_1}(t=0) = m_{S_1}^0 = m_{seeds} \tag{4.11}$$

$$R_1(t=0) = R_1^0 \tag{4.12}$$

The initial conditions in liquid phase for each component (eq. 4.10) can be calculated from the initial composition of the solution. The initial solid mass for the target enantiomer is the seed mass $m_{seeds}$ introduced in the process (eq. 4.11). The initial radius $R_1^0$ of the target enantiomer is the mean of the experimentally determined crystal size distribution. As explained in assumption V, the total number of particles at the beginning of the process is assumed to be same during the process. It can be calculated by the ratio of the initial seed mass to initial mass of one single particle as shown in eq 4.13.

$$N_1(t=0) = N_1^0 = \frac{m_{seeds}}{\rho_S \frac{4}{3}\pi {R_1^0}^3} \tag{4.13}$$

The initial conditions for the solid phase of target enantiomer rely on the initial conditions of the PC experiment. Nevertheless, the initial conditions for the solid phase of counter enantiomer depend on assumptions. The initial size of the crystal $R_2^0$ should be a small quantity below a contamination threshold. We used 0.01 nm, which is even below the single unit cell unit cells or zero-dimensional crystal structure. For determining its order of magnitude, the total number of counter enantiomer particles $N_2^0$ did not act as a very sensitive parameter. To conclude the SCM, we suggest an easy approach to set $N_2^0$ to be equal to the number of particles of the target enantiomer $N_1^0$, i. e.,

$$N_2(t=0) = N_2^0 = N_1^0 \qquad 4.14$$

We have made strong simplifications in order to obtain minimum number of equations that could still model isothermal PC with good approximation. As indicated in assumptions 1 and 3, in order to decrease the number of crystallization kinetic parameters, the particulate system was assumed to consist of monodispersed spheres, and all kinetic terms were grouped into the $k^{eff}$. As described in chapter 2, nucleation is an important mechanism in PC. To account for this phenomenon without the strong support of nucleation theory, assumptions III, IV and V were made. In order to approximate the model in the contamination phase of the PC process, we have introduced the parameter $t_{stop}$, along with the contamination factor $\mathrm{F}_2$. Supersaturation is the driving force for PC, which was introduced via a power law function depends only on effective order $n^{eff}$ and $S_i$ (calculated from the TPD and depicted in chapter 2).

### 4.1.3. Implementation of SCM

Set of ODEs (eqs 4.4 to 4.8) with initial conditions given in eqs. 4.10 to 4.14 can be solved simultaneously in MATLAB (Mathworks M 2017) using solver ode15s. The required parameters for the simulation are $m_{seeds}$, $\rho_S$, $m_1^0$, $m_2^0$, $m_3^0$, $R_1^0$, $R_2^0$, $w_{sat,1}^0$and $w_{sat,2}^0$. The transients of $m_1$, $m_2$, $m_3$, $R_1$ and $R_2$ are provided by the solution of the ODE equations to estimate the process characteristics such as productivity, yield or enantiomeric excess.

An illustrative description of the shortcut model is shown using figure 4.6. The mass fraction of the enantiomer 1 in the liquid phase starts at the initial concentration and depletes to the equilibrium state. The concentration of the enantiomer 2 in the liquid phase remains constant until stop time ($t_{stop}$), and its mass fraction marginally increases (top plot of figure 4.6). The reason is the reduction of the total mass of the liquid due to the crystallization of the enantiomer 1. After $t_{stop}$, very small crystals of enantiomer 2, initially inactive, start growing. It results in the drop in concentration of the enantiomer 2 until equilibrium is reached. The loss in the liquid phase concentration of the enantiomers contributes to the increase in the solid mass ($m_{S,i}$) (bottom plot of figure 4.6). The enantiomeric excess ($ee$) evolution can be

calculated from the mass fraction concentrations as described in eq. 4.15. An $ee$ can be estimated for both liquid ($ee_L$) and solid ($ee_S$) phases, as shown in figure 4.6.

$$ee = \frac{|w_2 - w_1|}{w_2 + w_1} \qquad 4.15$$

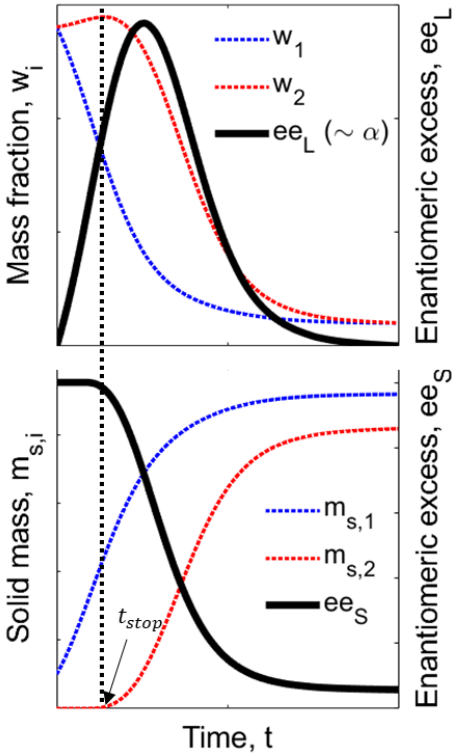


**Figure 4.6**: A descriptive analysis of PC through the SCM showcases: (a) the changes in the mass fraction and the enantiomeric excess in the liquid phase $ee_L$ (which is directly proportional with the optical rotation α), and (b) the evolution of the mass of solids and the enantiomeric excess $ee_S$ in the solid phase. According to the shortcut model, the initial "nuclei" of the counter enantiomer are considered to be virtually in existence from the beginning of PC, yet they remain inactive until the process arrives at the stop time $t_{stop}$.

In a batch isothermal PC process, the $ee_L$ at liquid phase starts at zero, since the initial feed concentration of both the enantiomers in the liquid phase is racemic (50% enantiomer 1 and 50% enantiomer 2). It reaches a maximum and depletes following the crystallization of the enantiomer 2. The enantiomer excess in the solid phase depicts product purity and falls after the $t_{stop}$ is reached. For the purpose of validating the model and estimating SCM kinetic parameters, it is important to obtain experimental data on the time progression of PC. We suggest the use of a polarimeter with online optical rotation measurements. It is simple to apply and calibrate with the relationship explained in chapter 2 using eqs. 2.14 and 2.15.

### 4.1.4. Estimation of the essential SCM parameters

It is necessary to parameterize and apply the preliminary knowledge regarding solubility and width of metastable zone (MZ) to the model in the range of potential application. Thus, as described in eqs. 4.4 to 4.9, the SCM consists of three main essential parameters: stop time ($t_{stop}$), effective crystallization rate constant ($k^{eff}$), and effective order of crystallization ($n^{eff}$). They must be determined with the help of experimental data.

SCM can be used to optimize one or more process parameters. For each process parameter, a minimum of three successful PC experiments are required to determine the free model parameters. In this work, the three experiments were performed by changing only one process parameter i.e., the initial supersaturation ($S_i^0$) while keeping the seeding strategy (i.e., mass and size) and crystallization temperature ($T_{cryst}$) constant. It will be shown that this allows parameterizing correlations for estimating $t_{stop}$ and $k^{eff}$. During the experiments, the changes in optical rotation $\alpha$ over time were measured with an online polarimeter.

In summary, we propose the following strategies for estimating the free parameters of the SCM:

1) To determine $k_\alpha$(T) by calibrating polarimeter;
2) Record the profiles of optical rotation $\alpha_I(t)$, $\alpha_{II}(t)$ and $\alpha_{III}(t)$ by performing experiments I, II and III for three different initial supersaturations ($S_I^0$, $S_{II}^0$, $S_{III}^0$ at the same $T_{cryst}$ using the same seed amounts of the same sizes);
3) For each of the three experiments: find $\alpha_{max}$, calculate $X_\alpha * \alpha_{max}$ and determine $t_{stop}$ (see below, figure 4.7 and section 4.1.4.1);
4) Apply the SCM to simulate the initial part of the three experiments until $t_{stop}$ using eqs. 4.4, 4.6 and 4.7, that is generating $\alpha_{theo_I}[0, t_{stop_I}]$, $\alpha_{theo_{II}}[0, t_{stop_{II}}]$ and $\alpha_{theo_{III}}[0, t_{stop_{III}}]$;
5) Estimate the three free parameters by minimizing the error between simulation and experiments, i. e. various sets of $n^{eff}$, $k_I^{eff}(S_I^0)$, $k_{II}^{eff}(S_{II}^0)$, $k_{III}^{eff}(S_{III}^0)$ (see objective function eq 4.16);
6) Correlate the three determined $t_{stop}$ values with the initial supersaturations $S^0$ (section 4.1.4.3);
7) Correlate the three determined $k^{eff}$ values with the initial supersaturations $S^0$ (section 4.1.4.3).

Step 2 might be broken up into two sections for the purpose of carrying out these strategies in the most effective manner: first, conduct one experiment, and then, using the findings of that experiment and the parameters of the compound or process under study, determine the subsequent initial conditions (e.g., higher or lower initial supersaturation).

In order to broaden the scope of the model's applicability even further, additional experiments with various initial solid phase areas are going to be carried out.

#### 4.1.4.1. Stop time

The stop time ($t_{stop}$) is a key parameter of the SCM. It is defined as the time until which the growth of the already present crystals of the counter enantiomer is assumed to be inactive. It provides a basis of the time window for the synthesis of the target enantiomer. The SCM simulations are exclusively seek to anticipate this region. A discrete contamination factor, $F_2$, is used to implement $t_{stop}$ in the ODE systems forming the SCM. The optical rotation reaches its maximum after the nucleation of the counter enantiomer and then decreases until it approaches zero when equilibrium has been reached. However, it is harder to determine exactly when the nucleation of the counter enantiomer first begins. This is because of the nature of the process. Therefore, in order to have a safer window in which to harvest the product, it is suggested to stop the process before it reaches the maximum enantiomeric excess of liquid phase. In this research, the value of stop time is determined by the amount of time that is necessary to reach, $X_\alpha$ = 90% of the maximum polarimetric signal $\alpha_{max}$ (figure 4.7). It is well known that nucleation, and by extension, stop time, is a parameter that is unique to a particular setup (Mersmann 2001). As a result, it is also dependent upon the scale of the process. As a result, it would be more useful to conduct the experiments at the scale that would subsequently be employed for manufacturing. If this is not possible, an additional uncertainty must be accepted.

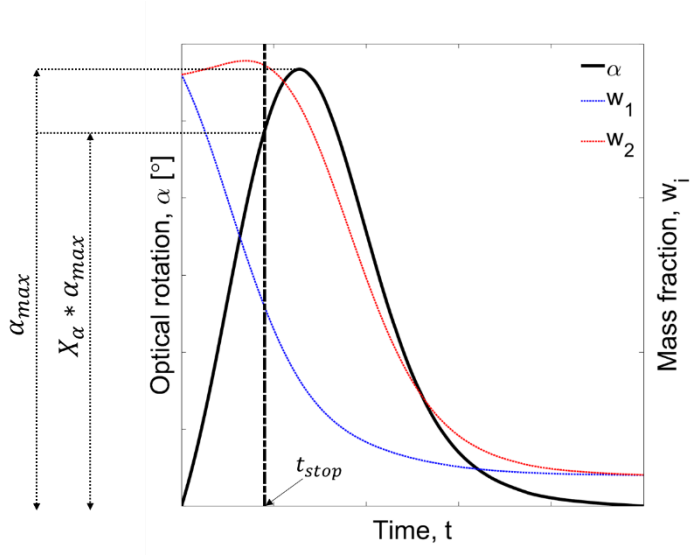


**Figure 4.7**: Depiction of the determination of stop time $t_{stop}$ for PC. The operation window for the process extends from the initial moment (t = 0) to the observed decline in solid product, which occurs mainly as the counter enantiomer begins to crystallize. The value $X_\alpha$ represents

90% of the maximum achievable optical rotation $\alpha_{max}$, chosen to ensure the purity of the final product.

#### 4.1.4.2. Effective rate constant and order of crystallization

The amount of solid that crystallizes is directly proportional to the value of a rate constant called the effective crystallization rate constant $k^{eff}$. It is accountable for the overall mass transfer that occurs as a result of both nucleation and growth. The effective order of crystallization kinetics, denoted by the notation $n^{eff}$, is the hypothetical order that represents the driving force behind the total mass transfer process. It is assumed in the SCM to be independent on initial supersaturation and to be a constant value for a specific system. Both parameters, $k^{eff}$ and $n^{eff}$, should be estimated simultaneously based on experimental results.

There are several methods for estimating model parameters. The suggested approach for obtaining the parameters utilizes a loop with two minimizations. The objective function that was minimized is given in eq. 4.16. A set of four parameters are optimized simultaneously, namely $n^{eff}$ and the three $k^{eff}$ for experiments $I$, $II$ and $III$, i.e., $k_I^{eff}$, $k_{II}^{eff}$, $k_{III}^{eff}$. Eq. 2.12 is used to calculate the polarimetric signals $\alpha_{exp}(t)$ and $\alpha_{theo}(t)$ for each experiment. Only until, $t_{stop}$ are the data values of $\alpha_{exp}$ and $\alpha_{theo}$ utilized to estimate the parameters. To reduce the inaccuracies between, $\alpha_{exp}$ and $\alpha_{theo}$, high resolution scanning was done over the four parameters.

$$
\begin{aligned}
OF\left(n^{eff}, k_I^{eff}, k_{II}^{eff}, k_{III}^{eff}\right) \\
&= \min_{n^{eff}} \left[ \min_{k_I^{eff}} \sum_{j=1}^{J} \left( \alpha_{exp_I}(t) - \alpha_{theo_j}\left(t, n^{eff}, k_{I_j}^{eff}\right) \right)^2 \right. \\
&+ \min_{k_{II}^{eff}} \sum_{j=1}^{J} \left( \alpha_{exp_{II}}(t) - \alpha_{theo_j}\left(t, n^{eff}, k_{II_j}^{eff}\right) \right)^2 \\
&\left. + \min_{k_{III}^{eff}} \sum_{j=1}^{J} \left( \alpha_{exp_{III}}(t) - \alpha_{theo_j}\left(t, n^{eff}, k_{III_j}^{eff}\right) \right)^2 \right]
\end{aligned}
\tag{4.16}
$$

#### 4.1.4.3. Correlation of $t_{stop}$ and $k^{eff}$ with initial supersaturation $S^0$

Stop time ($t_{stop}$) and effective crystallization rate constant ($k^{eff}$) are evidently functions of temperature and supersaturation and are dependent on these values at every moment in time. We suggest correlating initially only these two factors with initial supersaturation for the purpose of simplicity. The same crystallization temperature is used for the series of experiments used to evaluate the model and correlation parameters. The inclusion of temperature will be discussed towards the conclusion of this work. Lower

supersaturation levels are anticipated to cause a longer stop time, and vice versa. Eq. 4.17 describes the limiting conditions for, $t_{stop}$.

$$t_{stop} = \begin{cases} 0, & S^0 \to \infty \\ \infty, & S^0 = 1 \end{cases} \quad 4.17$$

Eq. 4.18 provides a simple empirical model for calculating $t_{stop}$. as a function of supersaturation. The correlation parameters $(a_t, b_t)$ can be determined using least-squares curve fitting of the linearized form of this equation.

$$t_{stop}(S^0) = \frac{a_t}{(S^0 - 1)^{b_t}} \quad 4.18$$

On the other hand, $k^{eff}$ may depend on $S^0$ in a number of different ways due to the fact that it combines several effects that are responsible for the mass transfer between the phases. As a result, there is a need for a dependency on the initial supersaturation that is more flexible. We chose a log-logistic distribution with three parameters $a_k$, $b_k$, $c_k$ as given by eq 4.19. In the event that the solution is not supersaturated, crystallization should not take place., i.e., $S^0 = 1$, $k^{eff} = 0$. The MATLAB fmincon function (Mathworks M 2017) was used to determine $a_k$, $b_k$, and $c_k$ from the results of three experiments with three different supersaturations.

$$k^{eff}(S^0) = a_k \frac{\left(\frac{b_k}{c_k}\right)\left(\frac{S^0 - 1}{c_k}\right)^{b_k - 1}}{\left(1 + \left(\frac{S^0 - 1}{c_k}\right)^{b_k}\right)^2} \quad 4.19$$

To account for the impact of temperature on the effective rate constant, we propose extending the correlation given in eq. 4.19 in accordance with the Arrhenius law as follows:

$$k^{eff} = k_0^{eff}\, e^{\left(\frac{-E^{eff}}{R_g T}\right)} \quad 4.20$$

$$k_0^{eff}(S^0, T) = a_{k,T} \frac{\left(\frac{b_{k,T}}{c_{k,T}}\right)\left(\frac{S^0 - 1}{c_{k,T}}\right)^{b_{k,T} - 1}}{\left(1 + \left(\frac{S^0 - 1}{c_{k,T}}\right)^{b_{k,T}}\right)^2} \quad 4.21$$

Note that $a_{k,T}$, $b_{k,T}$, $c_{k,T} \neq a_k$, $b_k$, $c_k$ from eq 4.19, since the parameters in eq 4.21 are also temperature dependent.

## 4.2. Extending the SCM to describe continuous PC

In this section, we aim to exploit the Shortcut Model (SCM) in dimensionless form to accurately depict the continuous PC at steady state. This application will exploit the principles and methodologies prevalent in chemical reaction engineering, specifically referencing literature sources (Fogler 2006; Garside and N.S. 1984; Levenspiel 1999). We will apply the well-established analogy that equates batch processing in fully agitated tanks to continuous operations in tubular reactors under steady-state plug flow conditions. This analogy will serve as the basis to develop broadly applicable dimensionless equations. Our analysis will contrast two distinct cases: the first is an idealized, optimistic scenario that disregards any back-mixing effects in both phases, thus representing an ideal plug flow situation. The second, more practical case, will extend the model to account for back-mixing occurring within each phase, offering a more comprehensive view that aligns closely with real-world applications of PC.

### 4.2.1. Dimensionless SCM: continuous spatially distributed steady-state operation

The SCM described in section 4.1 did not yet exploit the opportunity to incorporate informative and meaningful dimensionless quantities. In this section, we transform the model into a dimensionless form and expand it to explain the steady state of PC in a tubular crystallizer operating in a continuous mode. Henceforth, we will focus primarily on systems that form conglomerates. We will thus exclude enantiomers that produce racemic compounds or solvates. To develop the model equations, we will use dimensionless numbers, which have been implemented in the chemical reactions engineering (Fogler 2006; Levenspiel 1999). Before incorporating them, we will review the model's assumptions again:

a) We assume that the preferred crystallization process is entirely controlled by growth, and as a result, the number of particles does not vary along the length of the crystallizer z throughout the steady-state production period. This also implies that the flow of particles in continuous processes operating under steady-state conditions, $\dot{N}_i$, is constant at all z positions, i.e.:

$$\dot{N}_i(z) = \dot{N}_i(z=0) = \dot{N}_{i,in} = \frac{\dot{m}_{seeds}}{\frac{4}{3}\pi R_1^3 \rho_S} \quad i \in \{1,2\} \tag{4.22}$$

b) In relation to the total crystal surface area, an effective growth rate is evaluated during the production period. It is assumed that the kinetics of the target component $i$ can be characterized in a simplified fashion by a power law dependency on the supersaturation, as shown in eq. 4.23:

$$G_i^{eff} = k^{eff}\left(\frac{c_i - c_{i,sat}}{c_{i,sat}}\right)^{n^{eff}} \qquad i \in \{1,2\} \tag{4.23}$$

c) All particles are assumed to be spherical. At a certain point in time in the mixed batch vessel or at a specific spatial position in the plug flow tubular crystallizer (PFTC), these particles have same radii, $R_i$,. that vary with time and spatial position ($R_i(z)$).

d) We assume that there is the same particle number density at each position z, and this holds true for the respective particle and volumetric liquid phase steady-state fluxes: i.e.:

$$n_{i,S} = \frac{\dot{N}_i(z)}{\dot{V}_L(z)} = \frac{dN_i}{dV_L} = \frac{N_{i,tot}}{V_{L,tot}} \qquad i \in \{1,2\} \tag{4.24}$$

e) In the case of continuous operation, it is also assumed that the liquid and solid phases move with the same constant velocity $u_L = \ u_S = u$.

These assumptions allow for the derivation of the mass balances for a component $i$ in a continuous tube crystallizer, taking into account or disregarding the potential of axial back-mixing.

**Liquid phase mass balances**

The following mass balances hold true for each enantiomer in the liquid phase for a differential volume element $dV_L$:

$$\frac{dm_{i.L}}{dt} = -d\dot{m}_{L,i,conv} - d\dot{m}_{L,i,cryst} + d\dot{m}_{L,i,disp} \qquad i \in \{1,2\} \tag{4.25}$$

These dynamic balances also include expressions for convection, dispersion, and crystallization, in addition to accumulation. Similar balances hold for the solid phase, as stated in the next section.

We will explore two scenarios below, one hypothetically optimistic scenario 1 that ignores back mixing and the other more realistic scenario 2, which takes into account the impact of inevitable back mixing, assuming established steady-state conditions.

### 4.2.2. Steady-state operation with no back-mixing

Assuming a steady state and disregarding back-mixing simplifies the liquid phase mass balance eq. 4.26 for a differential volume element of a tubular crystallizer of dimension $dV_L$ to:

$$0 = -d\dot{m}_{L,i,conv} - d\dot{m}_{L,i,cryst} \qquad i \in \{1,2\} \tag{4.26}$$

The convection term is obtained by expressing the differential liquid phase volume by the cross-sectional area, $dV_L = A_C dz$:

$$d\dot{m}_{L,i,conv} = \dot{V}_L \, dc_i = A_c u dc_i \qquad i \in \{1,2\} \tag{4.27}$$

In accord with eq. 4.4 and utilizing eq. 2.1, the second term of eq. 4.25, which quantifies the influence of crystallization, can be written as follows:

$$d\dot{m}_{L,i,cryst} = -k^{eff} \dot{N}_{i,in} 4\pi R_i^2 \left( \frac{c_i - c_{i,sat}}{c_{i,sat}} \right)^{n^{eff}} \qquad i \in \{1,2\} \tag{4.28}$$

Plugging eqs. 4.27 and 4.28 into eq 4.26, dividing by $dV_L$, and using eqs. 2.1, 4.22, and 4.24 gives:

$$u \frac{dc_i}{dz} = -n_{i,s} k^{eff} 4\pi R_i^2 \left( \frac{c_i - c_{i,sat}}{c_{i,sat}} \right)^{n^{eff}} \qquad i \in \{1,2\} \tag{4.29}$$

This ordinary differential equation relates essentially to the crystallizer's mass balance (eq. 4.4). In the coming section, we will compare the performance of batch and continuous operations based on this similarity. This analogy demonstrates that matching the batch operation (real) time with the residence time provided by a continuous crystallizer operating in steady state and plug flow mode provides similar productivities.

As the concentration of the liquid phase diminishes, the radii of the crystalline particles will grow with time (starting from $R_{i,0}$ in batch processes) or along the length of the system (starting from $R_{i,in}$ in continuous operations). The particles will attain their maximum sizes under equilibrium conditions, which hypothetically correspond to an infinite duration or an infinitely long length. These maximum sizes can be calculated using the saturation concentrations in combined with the overall mass balances. This calculation in eq. 4.30 enables the estimation of the maximum solid phase volumes achievable when the supersaturation levels are entirely exhausted:

$$\left(c_{i,in} - c_{i,sat}\right) = \frac{4\pi}{3} n_{i,S} \rho_S \left(R_{i,eq}^3 - R_{i,in}^3\right) \qquad i \in \{1,2\} \tag{4.30}$$

Eq. 4.29 provides for the two enantiomers the following specific maximum radii under equilibrium conditions respecting the initial (seeded) radii $R_{i,in}$:

$$R_{i,eq} = \sqrt[3]{\frac{3}{4\pi n_{i,S}} \frac{\left(c_{i,in} - c_{i,sat}\right)}{\rho_S} + R_{i,in}^3} \qquad i \in \{1,2\} \tag{4.31}$$

In eq. 4.31, $R_{i,eq}$ represents a hypothetical maximum for the radii of the crystal formed under equilibrium conditions from particles of inlet radii, $R_{i,0}\ or\ R_{i,in}$, providing infinite time in batch or infinite length in tubes.

By normalizing the maximum values of the solid phase volume changes, we can establish the maxima of dimensionless volume ratios, denoted as $\hat{V}_i^{max}$

$$\hat{V}_{max,i} = \frac{R_{i,eq}^3 - R_{i,\mathrm{in}}^3}{R_{i,eq}^3} \qquad i \in \{1,2\} \tag{4.32}$$

it's also beneficial to define the incoming (or seeded) solid-phase mass flux of the target enantiomer 1, expressed as $\dot{m}_{1,in} = \dot{m}_{1,seeds}$. This mass flux is influenced by the incoming radius of the particles and their number flux, which is explained in eq. 4.33.

$$\dot{m}_{1,seeds} = \frac{4\pi}{3} \rho_S \dot{N}_1 R_{1,in}^3 \qquad i \in \{1,2\} \tag{4.33}$$

This mass flux can be normalized as well:

$$\hat{M}_{1,seeds} = \frac{\dot{m}_{1,seeds}}{\dot{m}_{max}} \qquad i \in \{1,2\} \tag{4.34}$$

In eq. 4.34, $\dot{m}_{max}$ describes the maximum of the mass flux of the target enantiomer achievable. This maximum can be calculated using an overall mass balance:

$$\dot{m}_{max} = \dot{V}_L \left(c_{1,in} - c_{1,sat}\right) \qquad i \in \{1,2\} \tag{4.35}$$

To quantify the crystallization rate within the system, it is practical to define characteristic crystallization rate constants. These constants combine the effective crystallization rate constants, account for the number of seed particles introduced, and include the maximum driving forces that are encountered at the inlet of the crystallizer. This approach allows for a more precise and comprehensive understanding of the crystallization kinetics:

$$k_i^{char} = n_{i,s} 4\pi k^{eff} \frac{\left(c_{i,in} - c_{i,sat}\right)^{n^{eff}-1}}{c_{i,sat}^{n^{eff}}} \qquad i \in \{1,2\} \tag{4.36}$$

The rate constant $k_i^{char}$ is introduced in this manner to indicate an inverse characteristic time of the liquid-to-solid phase mass transfer process.

To continue with the model, it is necessary to normalize the concentrations and radii using saturation and equilibrium states and the tube length as follows:

$$(a)\ \ \hat{c}_i = \frac{c_{i,in} - c_i}{c_{i,in} - c_{i,sat}} \qquad (b)\ \ \hat{R}_i = R_i / R_{i,eq} \qquad (c)\ \ \hat{z} = z/L \tag{4.37}$$

Using this constant and the introduced normalizations, the dimensional mass balance (eq. 4.29) can be rearranged as follows:

$$\frac{d\hat{c}_i}{d\hat{z}} = \frac{\frac{L}{u}}{\frac{1}{k_i^{char} R_{i,eq}^2}} \hat{R}_i^2 (1 - \hat{c}_i)^{n^{eff}} = \frac{L}{u} k_i^{char} R_{i,eq}^2 \hat{R}_i^2 (1 - \hat{c}_i)^{n^{eff}} \qquad i \in \{1,2\} \tag{4.38}$$

Additionally, we can define a residence time, $\tau_{PFTC}$, and a corresponding dimensionless time for the continuous PFTC process:

$$t_{PFTC} = \frac{L}{u} \tag{4.39}$$

The concept of residence time is crucial for introducing the dimensionless Damköhler numbers, denoted as $Da_i$ (as shown in equation 4.40). These numbers compare the actual time available for the separation process within the crystallizer to the characteristic times necessary for crystallization-based mass transfer between the phases, as summarized by the lumped crystallization mechanism. These characteristic times are in turn quantifiable by employing the characteristic crystallization rate constants (from eq. 4.36) along with the equilibrium radii (from eq. 4.31).

$$Da_i = \frac{\tau_{PFTC}}{\frac{1}{k_1^{char} R_{1,eq}^2}} = t_{PFTC} k_1^{char} R_{1,eq}^2 \qquad i \in \{1,2\} \tag{4.40}$$

The Damköhler numbers, which are different for the two enantiomers due to the seed size-dependent equilibrium radii, are less significant if substantial growth of the target enantiomer

is utilized. Focusing on the target component, we analyze the impact of its Damköhler number, $Da_i$, which governs the process performance up to a defined stopping time $t_{stop}$.

When equating the batch operation time in a stirred tank, $t_{stop}$, with the residence time in a tubular crystallizer, $\tau_{PFTC}$, the trends over the Damköhler numbers are consistent, suggesting comparable performances between these two idealized process scenarios.

By plugging equations 4.39 and 4.40 into equation 4.38, the resulting dimensionless mass balance equations for the liquid phase are given by:

$$\frac{d\hat{c}_i}{d\hat{z}} = Da_i \hat{R}_i^2 (1-\hat{c}_i)^{n^{eff}} \qquad i \in \{1,2\} \tag{4.41}$$

**Solid phase mass balances:**

Similar to eq. 4.25, the corresponding dynamic solid phase mass balances are as follows:

$$\frac{dm_{S,i}}{dt} = -d\dot{m}_{S,i,conv} + d\dot{m}_{S,i,cryst} + d\dot{m}_{S,i,disp} \qquad i \in \{1,2\} \tag{4.42}$$

We assume steady-state condition and ignore back-mixing again. Considering the previously introduced quantities derive the following dimensionless equilibrium equation:

$$d\dot{m}_{S,i,conv} = \rho_S d\dot{V}_S = \rho_S u dA_S = \rho_S u \frac{dV_S}{dz} = \rho_S u N_{i,z} 4\pi R_i^2 \frac{dR_i}{dz} \qquad i \in \{1,2\} \tag{4.43}$$

Using eqs. 4.28, 4.42 and 4.43, we get:

$$\rho_S u \dot{N}_{i,in} 4\pi R_i^2 \frac{dR_i}{dz} = \dot{N}_{i,in} 4\pi R_i^2 k^{eff} \frac{\left(c_{i,0} - c_{i,sat}\right)^{n^{eff}} (1-\hat{c}_i)^{n^{eff}}}{c_{i,sat}^{n^{eff}}} \qquad i \in \{1,2\} \tag{4.44}$$

Eq. 4.45 can be formulated dimensionless using the quantities given in the previous equations 4.37, 4.39, and 4.44:

$$\frac{d\hat{R}_i}{d\hat{z}} = \frac{\tau_{PFTC}}{\frac{1}{k_i^{char} R_{i,eq}^2}} \frac{R_{i,eq}^3 - R_{i,\text{in}}^3}{3R_{i,eq}^3} (1-\hat{c}_i)^{n^{eff}} \quad i \in \{1,2\} \tag{4.45}$$

After plugging in the Damköhler number (eq. 4.40), the following dimensionless solid phase mass balance is obtained:

$$\frac{d\widehat{R}_i}{d\hat{z}} = Da_i \frac{\widehat{V}_{max}}{3}(1-\hat{c}_i)^{n^{eff}} \qquad i \in \{1,2\} \tag{4.46}$$

#### 4.2.2.1. Boundary conditions for the liquid and solid phase mass balances

It is required to have boundary conditions in order to solve the two dimensionless mass balance equations for the liquid phase (eq. 4.41) and the solid phase (eq. 4.46). We will proceed under the assumption that the continuous processes are operated with constant inlet concentrations and radii at $\hat{z} = 0$:

$$\text{(a) } \hat{c}_i(\hat{z}=0) = \hat{c}_{i,in} \qquad (b)\ \widehat{R}_i(\hat{z}=0) = \widehat{R}_{i,in} \tag{4.47}$$

### 4.2.3. Effect of back-mixing in both phases

In order to exploit the hypothetical "ideal" plug flow scenario 1, extra dispersion factors were added to the liquid and solid phase mass balances. The back-mixing decreases crystallization driving forces and process performance. Considering classical methods applied to include second order back-mixing components in tubular reactor models (Levenspiel 1999), it is possible to formulate the following dispersion term for the liquid phase mass balance eq. 4.48:

$$d\dot{m}_{L,i,disp} = D_{ax,L} A_C \frac{dc_i}{dz} \qquad i \in \{1,2\} \tag{4.48}$$

**Liquid phase mass balances**

Now, plugging eq. 4.28 (crystallization), 4.43 (convection) and 4.48 (dispersion) in eq. 4.25, we get:

$$\frac{\partial c_i}{\partial t} = -u\frac{\partial c_i}{\partial z} + D_{ax,L,i}\frac{dc_i}{dz} - 4\pi R_i^2(z) n_{i,S} G_i^{eff}(z) \quad i \in \{1,2\} \tag{4.49}$$

Using dimensionless eqs. 4.36 and eq. 4.37, we can reduce eq. 4.49 to

$$\frac{\partial \hat{c}_i}{\partial t} = -\frac{u}{L}\frac{\partial \hat{c}_i}{\partial \hat{z}} + \frac{D_{ax,L,i}}{L^2}\frac{\partial^2 \hat{c}_i}{\partial \hat{z}^2} + k_i^{char} R_{i,eq}^2 \widehat{R}_i^2(z)\left(1-\hat{c}_i(z)\right)^{n^{eff}} \qquad i \in \{1,2\} \tag{4.50}$$

At steady state, eq. 4.50 can be expressed as:

$$\frac{d\hat{c}_i}{d\hat{z}} = \frac{D_{ax,L,i}}{uL}\frac{d^2\hat{c}_i}{d\hat{z}^2} + t_{PFTC}k_i^{char}R_{i,eq}^2\hat{R}_i^2(z)(1-\hat{c}_i(z))^{n^{eff}} \quad i \in \{1,2\} \tag{4.51}$$

It is possible to concisely describe the axial dispersion coefficient as a function of the dimensionless liquid phase Bodenstein number $Bo_L$, which indicates the ratio between the characteristic times for convection and dispersion:

$$Bo_L = \frac{\frac{1}{\frac{t_{PFTC}}{\frac{D_{ax,L}}{L^2}}}}{} = \frac{uL}{D_{ax,L}} \quad i \in \{1,2\} \tag{4.52}$$

Exploiting the normalizations introduced above allows extending eq. 4.41: The following dimensionless liquid phase mass balance equation results, which contains as additional parameter the Bodenstein number $Bo_L$:

$$\frac{d\hat{c}_i}{d\hat{z}} = Da_i\hat{R}_i^2(z)(1-\hat{c}_i(z))^{n^{eff}} + \frac{1}{Bo_L}\frac{d^2\hat{c}_i}{d\hat{z}^2} \quad i \in \{1,2\} \tag{4.53}$$

**Solid phase mass balances**

A dispersion term can be defined for the spherical particles of the solid phase in a manner that is similar to how it is formulated for the liquid phase by taking into consideration the fact that local gradients of the increasing particle surface areas or sizes are a basis for back mixing:

$$d\dot{m}_{S,i,disp} = \rho_S D_{ax,S}\frac{dA_{S,i}}{dz} = \rho_{S,i}D_{ax,S}\left(2N_{i,z}\,4\pi R_i\frac{dR_i}{dz}\right) \quad i \in \{1,2\} \tag{4.54}$$

When we plug in the terms that quantify the mass transfer that occurs as a result of crystallization (eq. 4.28), convection (eq. 4.43), and dispersion (eq. 4.54) in eq. 4.42 at steady state, we obtain the following:

$$\rho_S u\left(R_i\frac{dR_i}{dz}\right) - \rho_S D_{ax,S}\left(2\frac{dR_i}{dz}\right) = R_i\left(k_i^{eff}\frac{\left(c_{i,0}-c_{i,sat}\right)^{n^{eff}}(1-\hat{c}_i)^{n^{eff}}}{c_{i,sat}^{n^{eff}}}\right) \quad i \in \{1,2\} \tag{4.55}$$

In addition, by making use of the dimensionless quantities presented in 4.37, and 4.40, one can obtain the dimensionless solid phase mass balances that are as follows:

$$\frac{d\widehat{R}_i}{d\hat{z}} = \frac{t_{PFTC}R_{i,eq}^2}{\left(1-\frac{2}{Bo_{i,S}\widehat{R}_i}\right)} * \frac{\left(\frac{k_i^{eff}\left(c_{i,0}-c_{i,sat}\right)^{n^{eff}}(1-\hat{c}_i)^{n^{eff}}}{c_{i,sat}^{n^{eff}}}\right)}{R_{i,eq}^3\rho_{S,i}} \quad i \in \{1,2\} \qquad 4.56$$

Reducing eq. 4.56 by using eq. 4.30 and 4.36, we get:

$$\frac{d\widehat{R}_i}{d\hat{z}} = \frac{\frac{R_{i,eq}^3-R_{i,0}^3}{3R_{i,eq}^3}\left(t_{PFTC}R_{i,eq}^2k_i^{char}\right)(1-\hat{c}_i)^{n^{eff}}}{\left(1-\frac{2}{Bo_{i,S}\widehat{R}_i}\right)} \quad i \in \{1,2\} \qquad 4.57$$

The degree of back-mixing in the solid phase described in this manner can be now also quantified introducing the following dimensionless number, which we designate as the solid phase Bodenstein number $Bo_S$:

$$Bo_S = \frac{uR_{i,eq}}{D_{ax,S}} \quad i \in \{1,2\} \qquad 4.58$$

By plugging eq 4.32 and 4.58, we can rewrite eq. 4.57 as:

$$\frac{d\widehat{R}_i}{d\hat{z}} = Da_i\frac{V_{max,i}}{3}(1-\hat{c}_i)^{n^{eff}}\left(\frac{\widehat{R}_i}{\widehat{R}_i-2/Bo_S}\right) \quad i \in \{1,2\} \qquad 4.59$$

#### 4.2.3.1. Impact and comparison of the Bodenstein numbers

In comparison to eqs. 4.41 and 4.46, eqs. 4.53 and 4.59 introduce two Bodenstein numbers as extra model parameters. These numbers are denoted by the notations $Bo_L$ and $Bo_S$. Higher values of these Bodenstein numbers indicate that the rate of back-mixing along the z-direction is much slower than the corresponding mass transport by convection, whereas lower values of these Bodenstein numbers indicate that the mixing rate is much faster than the rate at which the mass is being transported by convection. Eqs. 4.53 and 4.59 will converge to the plug flow situation if the Bodenstein numbers approach closer to infinity (eqs. 4.41 and 4.46).

#### 4.2.3.2. Boundary conditions (BC) for the liquid and solid phase mass balances

The Dankwerts (Danckwerts 1953; Westerterp et al. 1984) BC is able to capture the mixing that takes place at the inlet. An extra condition needs to be considered for the outlet as a

result of the introduction of the second order term in the liquid phase mass balance. The following BC are the final steps in the development of the SCM:

**At liquid phase:**

$$uc_{i,in} = uc_{i,0} - D_{ax,L,i}\left(\frac{dc_i}{dz}\right)_{z=0} \qquad i \in \{1,2\} \tag{4.60}$$

By using dimensionless parameters of eq. 4.37, we get:

$$c_{i,0} - \hat{c}_{i,in}\left(c_{i,0} - c_{i,sat}\right) = c_{i,0} - \hat{c}_{i,0}\left(c_{i,0} - c_{i,sat}\right) + \left(c_{i,0} - c_{i,sat}\right)\frac{D_{ax,L,i}}{uL}\left(\frac{d\hat{c}_i}{d\hat{z}}\right)_{\hat{z}=0} \qquad i \in \{1,2\} \tag{4.61}$$

Boundary conditions for the liquid phase are:

$$\hat{c}_i(\hat{z}=0) = \hat{c}_{i,in} + \frac{1}{Bo_L}\left(\frac{d\hat{c}_i}{d\hat{z}}\right)_{\hat{z}=0} \qquad \left(\frac{d\hat{c}_{i,n}}{d\hat{z}}\right)_{\hat{z}=1} = 0 \tag{4.62}$$

**At solid phase:**

At $z = 0$

$$\dot{m}_{S,i,in} = \dot{m}_{S,i,0} - \rho_{S,i} D_{ax,S,i}\left(\frac{dA_{S,i}}{dz}\right)_{z=0} \qquad i \in \{1,2\} \tag{4.63}$$

$$\frac{\dot{N}_{S,i,IN}}{N_i}\frac{4}{3}\pi R_{i,IN}^3 \rho_{S,i} = \frac{\dot{N}_{S,i,0}}{N_i}\frac{4}{3}\pi R_{i,0}^3 \rho_{S,i} - 2\rho_{S,i} D_{ax,S,i}\left(4\pi R_{i,0}\frac{N_i}{N_i}\right)\left(\frac{dR_i}{dz}\right)_{z=0} \qquad i \in \{1,2\} \tag{4.64}$$

This reduces eq. 4.64 to eq. 4.65 by incorporating eq. 4.37 and eq. 4.58. It provides us the BC for the solid phase:

$$\hat{R}_i^3(\hat{z}=0) = \hat{R}_{i,in}^3 + \frac{6\hat{R}_{i,0}}{Bo_S}\left(\frac{d\hat{R}_i}{d\hat{z}}\right)_{\hat{z}=0} \qquad i \in \{1,2\} \tag{4.65}$$

An essential parameter of the model defines for both batch and continuous preferential crystallization is the onset of the nucleation of the unwanted counter enantiomer. In the previous section 4.1.4.1, we introduced a characteristic stop-time, $t_{stop}$, for batch operations, which triggers the growth of very small initially already present crystals of the counter enantiomer. At this time solid-phase contamination begins, and a batch process must be stopped if high purity requirements need to be reached. This stop time is also a very important

parameter in continuous operation and useful for normalizing local residence times as follows:

$$\hat{\tau}(u,z) = \frac{\frac{z}{u}}{t_{stop}} \tag{4.66}$$

Thus, nucleation of the unwanted enantiomers starts at $\hat{\tau} = 1$. This defines for a given velocity $u^*$ a characteristic stop length $z_{stop}$ at which the switch parameter $F_2$ (eq. 4.9) becomes 1:

$$z_{stop} = t_{stop} u^* \tag{4.67}$$

This length can be also expressed in a dimensionless way:

$$\hat{z}_{stop} = t_{stop} \frac{u^*}{L^*} = \frac{t_{stop}}{t_{PFTC}} \tag{4.68}$$

Inversely, to avoid contamination of the product in a given crystallizer of length, it is essential to run the process at a velocity which exceeds:

$$u_{stop} = \frac{L^*}{t_{stop}} \tag{4.69}$$

## 4.3. SCM for batch PC coupled with racemization

The integration of racemization with Preferential Crystallization (PC) presents a promising path to enhance the efficiency of producing pure enantiomers. This chapter investigates into extending the shortcut model (SCM) to incorporate this process integration, enabling the assessment of key performance indicators for the combined system (Bhandari et al. 2022). In the previous sections, we outlined all of the fundamental characteristics of the shortcut model that we have implemented directly in this work. Section 4.1.1 provides a full explanation of assumptions such as the application of a stop time ($t_{stop}$) and an effective crystallization rate constant ($k^{eff}$) (lumping of nucleation and growth).

### 4.3.1. Possible coupled process schemes

Several methodologies exist through which the racemization step can be combined with the process of preferential crystallization. In this chapter, a pair of distinct configuration approaches are examined: one involving spatial integration and the other consisting spatial segregation. In configurations characterized by spatial integration, the processes of racemization and crystallization occur within a same reactor system. Conversely, the spatial

segregation involves racemization and crystallization to take place within separate dedicated units. In order for the racemization reaction to take place, a racemizing agent is required. As previously indicated, our current study is centered upon the utilization of biocatalytic agents to enhance the efficiency of preferential crystallization.

Catalytic processes may be implemented via two major strategies: homogeneous catalysis employing enzymes in their soluble form, and heterogeneous catalysis involving enzymes immobilized onto surfaces. Additionally, there are selections to be made regarding the enzyme's spatial arrangement: it can be introduced within the same vessel where crystallization takes place, or alternatively, placed within a separate vessel.

Two specific approaches involving the incorporation of either free or immobilized enzymes into the crystallization apparatus are depicted in figure 4.8. This approach is attractive considering the amount of equipment required. However, it is important to acknowledge the potential drawbacks, notably the increased complexity of downstream processing required to effectively isolate the valuable enzyme from the residual solution at the end of the batch process. Furthermore, another limitation is the necessity for the operational temperature of the racemization process to align with the crystallization temperature.

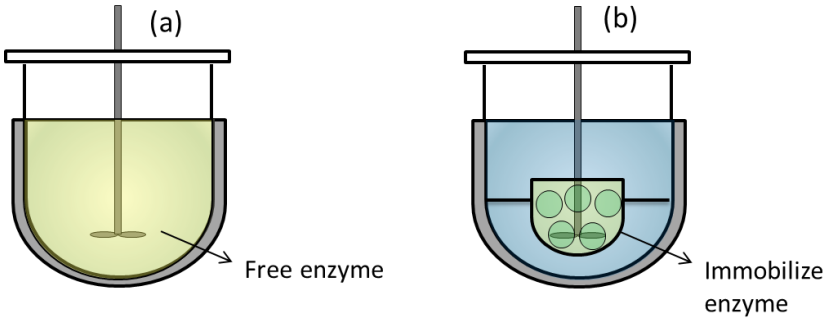


**Figure 4.8.** Depiction of simultaneous PC and racemization in a single, thoroughly mixed container. Part (a): A free enzyme, dissolved in the mixture, serves as a catalyst for racemization. Part (b): The enzyme is bound to a structure resembling a basket, which is attached to the mixing device.

Strategies for spatially segregation are outlined in figure 4.9. The crystallizer used for preferential crystallization (PC) is integrated with an external racemization module through a cyclic recycling loop. Three distinct variants of racemization reactors are investigated: a single stirred tank reactor (STR) utilizing free enzymes, an STR featuring immobilized enzymes, and a tubular fixed-bed reactor. The latter configuration can be represented as an arrangement of consecutive stirred tank reactors. It is important to note that the racemization units can be operated at higher temperatures relative to the PC process, thereby enhancing reaction kinetics and avoiding undesired crystallization in the connections outside of the crystallizer.

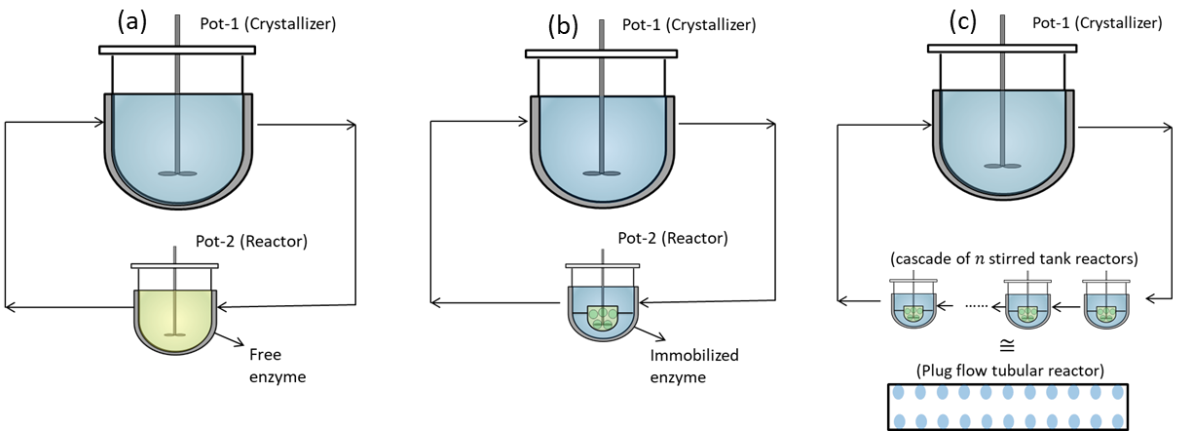


**Figure 4.9**. Graphic representation of selective crystallization in one well-stirred vessel, with racemization occurring in another vessel. (a) shows racemization occurring with a free enzyme in a stirred tank reactor. (b) depicts racemization with an enzyme that is immobilized within a stirred tank reactor. (c) illustrates racemization with an enzyme immobilized in a tubular reactor, which functions like a series of connected stirred tank reactors.

In the next sections, we will provide a model for describing the rates of enzyme racemization and model equations capable of characterizing all the reactor types depicted in figures 4.8 and 4.9.

### 4.3.2. Quantifying the rate of racemization reactions

In order to quantitatively assess the interconnected methodologies depicted in figures 4.8 and 4.9, an additional model is required, describing the rate of the racemization process involving the two mirror-image enantiomers (D, L or 1, 2), denoted as D⇌L. This reaction, catalysed by a racemase catalyst, changes the composition of the liquid phase. Consequently, the system approaches an equilibrium composition (racemic equilibrium).

While a simple approach involves applying first-order rate models to describe the forward and reverse reactions, the reaction mechanisms become more complex when enzymes are employed. Enzymatic mechanisms include the generation of intermediate complexes involving both reactants and products in conjunction with the biocatalyst. Moreover, enzyme-mediated reactions manifest substrate saturation at elevated substrate concentrations in relation to the catalyst quantity, and they may exhibit suboptimal binding affinities, leading to inhibited kinetics. Eq. 4.8 describes the kinetics of the formation of the desired enantiomer (denoted as 1) and the corresponding rate at which the opposing enantiomer is consumed, a process facilitated by a racemase (Petruševska-Seebach 2012).

$$r_{Rac} = \frac{1}{V_R}\frac{dm_1}{dt} = D_C \frac{\nu_{\max}\ \rho_L(w_2 - w_1)}{K_M + \rho_L(w_1 + w_2) + K_I\rho_L^2 w_2(w_1 + w_2)} \qquad 4.70$$

In eq. 4.70, $V_R$ signifies the volume of the reaction considered for scaling purposes, and $D_c$ represents the administered dosage or concentration of catalyst, measured in units of milligrams of enzyme per litre or grams of support material per litre, expressed respectively to the cases of free and immobilized enzyme forms. Additionally, $v_{max}$ and $K_M$ constitute parameters specific to a given enzyme operating within distinct conditions, such as factors like the reactant properties and the temperature range. A third enzyme-specific parameter, $K_I$, can be introduced in situations where enzyme inhibition occurs, consequently causing modifications in the catalytic behaviour of the enzyme. Lastly, $\rho_L$ corresponds to the density of the liquid phase.

When appropriately calibrated, eq. 4.70 can be effectively employed to characterize the reaction rates for both free and immobilized enzyme configurations.

## 4.3.3. Extension of SCM for different variants of coupling PC with racemization

### 4.3.3.1. Process integration in the same vessel

The quantification of the combination of preferential crystallization and racemization occurring in the same vessel (refer to figure 4.8) can be achieved by extending the SCM of preferential crystallization. The following assumptions are used when developing the equations:

- The racemization unit utilized in this study is of the stirred tank type.
- The reactor maintains a consistent temperature and volume throughout the process.
- The enzyme was well mixed inside the reaction vessel to ensure optimal homogeneity.
- The solubility of the enantiomers remains unaffected by the presence of the enzyme.

The reductions in the mass of the preferred enantiomer in the liquid phase within the Crystallizer-Reactor (C+R) can be attributed to the collective effects of crystallization and racemization, as described by eq. 4.70. Eqs. 4.71 and 4.72 characterize the changes in the mass in the liquid phase of the target enantiomer and the counter enantiomer, respectively. The process of crystallization is the sole factor responsible for the rate of change in solid mass. Hence, the mass balance equation for the solid phase stays unchanged, as stated in eqs. 4.7 and 4.8. The stoichiometric coefficients ($\nu_i$ = -1 or 1) necessary for the reaction term are also incorporated in the equations that follow.

$$\frac{dm_{1,C+R}}{dt} = -k^{eff} 4\pi N_1 R_1^2 (S_1 - 1)^{n^{eff}} + \nu_1 r_{Rac} \quad 4.71$$

$$\frac{dm_{2,C+R}}{dt} = -F_2 k^{eff} 4\pi N_2 R_2^2 (S_2 - 1)^{n^{eff}} + \nu_2 r_{Rac} \quad 4.72$$

Both the application of a free or an immobilized enzyme can be accurately represented by utilizing the correct equation, namely eq. 4.70, to determine the rate of reaction.

#### 4.3.3.2. Spatially segregated processes of PC and racemization

**Racemization in a well-mixed reactor**

The integration of batch preferential crystallization with an external enzymatic reactor is achieved in a spatially segregated system with the implementation of a recycling loop for the liquid phase. This study aimed to examine two distinct reactor designs for the enzymatic reactor, namely a single stirred tank reactor and a cascade of n stirred tank reactors. In an approach similar to the process scheme explained in the preceding section, the shortcut model is extended to include both of the spatially segregated systems. As seen in figure 4.9, a recycling stream free of solids flows through the racemization reactor for a specific residence time. The liquid phase, which is enriched in the desired enantiomer, is reintroduced into the crystallizer. The process design is based on the following assumptions:

- The crystallization process is represented by a stirred tank model, whereas the enzymatic reactor is represented by either a single stirred tank or a cascade of stirred tanks.
- The mass flow rate from all units is maintained at a constant value.
- All streams are free of crystals and enzyme.
- The free enzyme is well mixed inside the reaction volume.

The modified rate equations of the crystallizer setup must incorporate the input and output flow, as shown by eqs. 4.73 to 4.75:

$$\frac{dm_{1,C}}{dt} = -k^{eff} 4\pi\, N_1 R_1^2 (S_1 - 1)^{n^{eff}} + \dot{m}(w_{1,R} - w_{1,C}) \tag{4.73}$$

$$\frac{dm_{2,C}}{dt} = -F_2 k^{eff} 4\pi\, N_2 R_2^2 (S_2 - 1)^{n^{eff}} + \dot{m}(w_{2,R} - w_{2,C}) \tag{4.74}$$

$$\frac{dm_{3,C}}{dt} = -\left(k^{eff} 4\pi\, N_1 R_1^2 (S_1 - 1)^{n^{eff}} + F_2 k^{eff} 4\pi\, N_2 R_2^2 (S_2 - 1)^{n^{eff}}\right)\left(\frac{M_{Solvate}}{M_i} - 1\right) + \dot{m}(w_{3,R} - w_{3,C}) \tag{4.75}$$

The mass flow rate, denoted as $\dot{m}$, is measured in g/h. The variables $w_{1,R}$ and $w_{1,C}$ represent the mass fraction compositions of the streams exiting the reactor and the crystallizer, respectively.

The liquid phase, which has a lower concentration of the desired enantiomer, flows through the enzymatic reactor. The mass balance equations for a single stirred tank racemization reactor can be derived from the reaction kinetics specified in eq. 4.70. These equations are represented by eqs. 4.76 to 4.78.

$$\frac{dm_{1,R}}{dt} = V_R D_C \left( \frac{\nu_{\max}\ \rho_L (w_2 - w_1)}{K_M + \rho_L (w_1 + w_2) + K_I \rho_L^2 w_2 (w_1 + w_2)} \right) - \dot{m}(w_{1,R} - w_{1,C}) \quad 4.76$$

$$\frac{dm_{2,R}}{dt} = -V_R D_C \left( \frac{\nu_{\max}\ \rho_L (w_2 - w_1)}{K_M + \rho_L (w_1 + w_2) + K_I \rho_L^2 w_2 (w_1 + w_2)} \right) - \dot{m}(w_{2,R} - w_{2,C}) \quad 4.77$$

$$\frac{dm_{3,R}}{dt} = -\dot{m}(w_{3,R} - w_{3,C}) \quad 4.78$$

**Racemization in a cascade of well-mixed reactors**

In a cascade of n stirred tank reactors, the recycle flow originating from the crystallizer is sequentially directed through $n$ identical reactors arranged in series ($j = 1,2, \dots n$, with the total volume of this arrangement being equivalent to that of a single tank. At the start of this series, the initial concentration of the liquid phase in the first reactor equals the concentration leaving the crystallizer ($w_{1,0} = w_{1,C}$). The series of racemizing reactors effectively generates a stream that is enriched in the desired enantiomer, subsequently reintroduced into the crystallizer. The mass balance equations for target enantiomer over the span of these n reactors, as depicted in fig 4.10, are provided by eqs. 4.79 to 4.81.

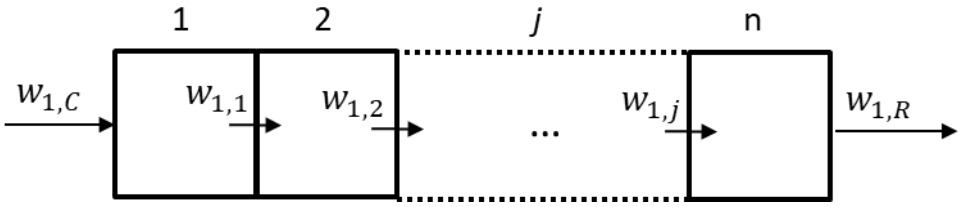


**Figure 6.3**. Diagram to represent flow of a selected enantiomer 1 in a cascade of $n$ stirred tank reactors connected in series (see figure 4.9c).

$$\frac{dm_{1,R,1}}{dt} = \nu_1 V_R D_C \left( \frac{\nu_{\max}\ \rho_L (w_{2,1} - w_{1,1})}{K_M + \rho_L (w_{1,1} + w_{2,1}) + K_I \rho_L^2 w_2 (w_{1,1} + w_{2,1})} \right) - \dot{m}(w_{1,1} - w_{1,0}) \quad 4.79$$

$$\frac{dm_{1,R,j}}{dt} = \nu_1 V_R D_C \left( \frac{\nu_{max}\ \rho_L (w_{2,j} - w_{1,j})}{K_M + \rho_L (w_{1,j} + w_{2,j}) + K_I \rho_L^2 w_2 (w_{1,j} + w_{2,j})} \right) - \dot{m}(w_{1,j} - w_{1,j-1}) \quad 4.80$$

$$j \in \{2,3, \dots, n-1\}$$

$$\frac{dm_{1,R,n}}{dt} = \nu_1 V_R D_C \left( \frac{\nu_{\max}\ \rho_L (w_{2,n} - w_{1,n})}{K_M + \rho_L (w_{1,n} + w_{2,n}) + K_I \rho_L^2 w_2 (w_{1,n} + w_{2,n})} \right) - \dot{m}(w_{1,R} - w_{1,n-1}) \quad 4.81$$

Similar equations eq. 4.82 to 4.84 also apply for counter enantiomer,

$$\frac{dm_{2,R,1}}{dt} = \nu_2 V_R D_C \left( \frac{\nu_{\max}\ \rho_L (w_{2,1} - w_{1,1})}{K_M + \rho_L (w_{1,1} + w_{2,1}) + K_I \rho_L^2 w_2 (w_{1,1} + w_{2,1})} \right) - \dot{m}(w_{2,1} - w_{2,0}) \quad 4.82$$

$$\frac{dm_{2,R,j}}{dt} = \nu_2 V_R D_C \left( \frac{\nu_{max}\ \rho_L (w_{2,j} - w_{1,j})}{K_M + \rho_L (w_{1,j} + w_{2,j}) + K_I \rho_L^2 w_2 (w_{1,j} + w_{2,j})} \right) - \dot{m}(w_{2,j} - w_{2,j-1}) \quad 4.83$$

$$j \in \{2,3,\dots,n-1\}$$

$$\frac{dm_{2,R,n}}{dt} = \nu_2 V_R D_C \left( \frac{\nu_{\max}\ \rho_L (w_{2,n} - w_{1,n})}{K_M + \rho_L (w_{1,n} + w_{2,n}) + K_I \rho_L^2 w_2 (w_{1,n} + w_{2,n})} \right) - \dot{m}(w_{2,R} - w_{2,n-1}) \quad 4.84$$

Maintaining the solvent balance eq. 4.85 to 4.87:

$$\frac{dm_{3,R,1}}{dt} = -\dot{m}(w_{3,1} - w_{3,0}) \quad 4.85$$

$$\frac{dm_{3,R,j}}{dt} = -\dot{m}(w_{3,j} - w_{3,j-1}) \qquad j \in \{2,3,\dots,n-1\} \quad 4.86$$

$$\frac{dm_{3,R,n}}{dt} = -\dot{m}(w_{3,R} - w_{3,n-1}) \quad 4.87$$

Having laid the theoretical groundwork for the Shortcut Model (SCM) in this chapter, the next chapter transitions to detailing the experimental parameters crucial for model development and validation. It serves as a bridge, shifting focus from theoretical development to practical application, by introducing two sets of experiments: one based on simulated data for the D-/L-threonine in water system and another involving actual experiments with the D-/L-asparagine monohydrate in water system. These experiments are foundational for the upcoming simulation results presented in Chapter 6, providing the basis needed to evaluate the SCM's effectiveness.

# 5. Experimental data used for case studies

In this chapter, we summarize important parameters that are required to apply the Shortcut Model's (SCM) development and validation. These experiment performed to determine the thermodynamic and kinetic parameters for two chiral systems were carried out in independent work as described by (Eicke 2016) and (Carneiro et al. 2019). Additionally, this chapter also demonstrate the racemization kinetics derived by Carneiro (Carneiro et al. 2020), which are needed to test the SCM for coupling racemization with PC. This experimental and parametrical basis is preparing the ground for the various sets of simulation results discussed in Chapter 6.

## 5.1. Experiments considered for model development and validation

To illustrate and validate the Shortcut model (SCM), two sets of experiments were used. First set are simulated "experiments" produced by employing an available fully parametrized population balance model (PBM) for the compound D-/L-threonine in water applying the kinetic parameters illustrated in table 5.1 (Eicke 2016). In the second set, actual experiments were carried out independently by Thiane Carneiro using the D-/L-asparagine monohydrate in water system, published in (Carneiro et al. 2019). The L enantiomer was considered the target molecule in both cases. These experiments are reported in the following subsections. Detailed solubility data and information on the metastable zone for threonine (Lorenz, Perlberg, et al. 2006; Sapoundjiev, Lorenz, and Seidel-Morgenstern 2006) and asparagine (Petruševska-Seebach 2012; Petruševska-Seebach, Seidel-Morgenstern, and Elsner 2011; Temmel et al. 2018) are already available. Both compounds exhibit almost ideal solubility behavior. For threonine, the solubility was assumed to be perfectly ideal, therefore $w_\alpha$ = 2 (eq 2.4). Using the existing solubility equation, $w_\alpha$ = 2.07 was obtained for asparagine monohydrate in the temperature range of application (Temmel et al. 2018). Table 5.2 describes the experimental conditions for both set of experiments.

**Table 5.1**. Kinetic parameters for population balance model of system D-/L-threonine in water (Eicke 2016).

| Kinetics | Symbol | Value | Unit |
|---|---|---|---|
| Growth | $k_{g,0}$ (eq. 2.11) | $1.32 \times 10^{10}$ | $\mathrm{m\,h^{-1}\,h^{n_g}}$ |
| | $E_{Ag}$ (eq. 2.11) | 76.1 | $\mathrm{kJ\,mol^{-1}}$ |
| | $g$ (eq. 2.10) | 1.5 | – |
| | $k_{bsec,0}$ (eq. 3.11) | $4.46 \times 10^{24}$ | $\mathrm{h^{-1}\,(m^3)^{-n_{\mu 3}}}$ |

| | | | |
|---|---|---|---|
| Secondary nucleation | $b_{sec}$ (eq. 3.11) | 4.33 | – |
| | $n_{\mu 3}$ [a] (eq. 3.11) | 0.83 | – |
| Primary nucleation | $k_{bprim1}$ (eq. 3.13) | $4.45 \times 10^{-2}$ | $h^{-1}\ K^{-1}\ m^{7}\ kg^{-(7/3)}$ |
| | $k_{bprim2}$ (eq. 3.13) | $4.65 \times 10^{-4}$ | – |
| | $A_{prim}$ (eq. 3.13) | $1.88 \times 10^{4}$ | $(m^2)^{-n_{\mu 2}}$ |
| | $n_{\mu 2}$ [b] (eq. 3.14) | 1.68 | – |

[a,b] Exponents of primary and secondary nucleation empirical kinetics, respectively.

**Table 5.2.** Summary of experimental conditions for both sets of experiments. Experiments $I_{(1)}$-$III_{(1)}$ and $I_{(2)}$-$III_{(2)}$ were used for parameter estimation. Experiments $IV_{(1)}$-$V_{(1)}$ were used to validate the range of application of the model and experiment $IV_{(2)}$ to study the influence of temperature in SCM parameters. In experiment 1: $m_{seeds}$ = 1 g and $V_L$ = 0.5 l; and in experiment 2: $m_{seeds}$ = 0.2 g, $V_L$ = 0.2 l. $w_1^0$ = initial conc. of target enantiomer (solubility at $T_{sat}$); $w_{sat,1}^0$ was calculated from the TPD (section 3.2) using $w_\alpha$. The initial solution was always racemic ($w_1^0 = w_{12}(T_{sat})/2$).

| **Model Compounds** | **Experiments** | $w_1^0$ [$10^2$ g g$^{-1}$] | $w_{sat,1}^0$ [$10^2$ g g$^{-1}$] | $S^0$ [-] | $T_{cryst}$ [°C] | $T_{sat}$ [°C] |
|---|---|---|---|---|---|---|
| 1[a]: threonine in water | $I_{(1)}$ | 8.10 | 7.40 | 1.09 | 18 | 24.5 |
| | $II_{(1)}$ | 8.39 | 7.40 | 1.14 | 18 | 27.5 |
| | $III_{(1)}$ | 8.71 | 7.40 | 1.17 | 18 | 30.5 |
| | $IV_{(1)}$ | 8.88 | 7.40 | 1.20 | 18 | 33 |
| | $V_{(1)}$ | 10.14 | 7.40 | 1.37 | 18 | 44 |
| 2[b]: asparagine monohydrate in water | $I_{(2)}$ | 4.56 | 3.68 | 1.24 | 30 | 35 |
| | $II_{(2)}$ | 4.95 | 3.68 | 1.34 | 30 | 37 |
| | $III_{(2)}$ | 5.57 | 3.68 | 1.51 | 30 | 40 |
| | $IV_{(2)}$ | 3.68 | 2.93 | 1.26 | 25 | 30 |

[a] experiments simulated with PBM.

[b] experimental procedure described in (Carneiro et al. 2019).

In all three experiments, the solution was seeded with $m_{seeds} = 0.2$ g L-asparagine monohydrate thoroughly sieved to the fraction 90-125 µm, after reaching $T_{cryst}$. In the

shortcut model, the mean size is characterized as the diameter of the particles, hence, $R_1^0$ = 53.7 microns.

## 5.2. Racemization kinetics

The model enzyme employed in this study is an amino acid racemase (AAR). Previous research (Carneiro et al. 2020) provided insights into the reaction kinetics of racemization both in a freely soluble state and when immobilized. Additionally, the practical application of the AAR was demonstrated under the operating conditions of PC. Notably, the amino acid racemase sourced from Pseudomonas putida was immobilized onto the commercial support material Purolite ECR 8309. This immobilized racemase has proven successful as a racemization agent in temperature cycling deracemization (Intaraboonrod, Harriehausen, et al. 2020) and has been explored for enhancing enantioselective chromatography (Kaspereit, Swernath, and Kienle 2011). Experimental kinetic data necessary for modelling an enzymatic reactor were obtained for both soluble and immobilized preparations (Petruševska-Seebach 2012). The racemization kinetics of asparagine racemization for both free and immobilized amino acid racemase are shown in Table 5.3.

**Table 5.3**. Kinetic parameters of asparagine racemization using free and immobilized amino acid racemase (Carneiro et al. 2020). The immobilized material was prepared with enzyme load of 35 mg-enzyme/g-support.

| **Type** | **T [°C]** | $\boldsymbol{\nu_{max}}$ **[$10^2$ gh$^{-1}$ mg-enzyme$^{-1}$]** | $\boldsymbol{K_M}$ **[$10^2$ gml$^{-1}$]** | $\boldsymbol{K_I}$ **1/ [$10^2$ gml$^{-1}$]** | **$D_C$ [mg-enzyme ml$^{-1}$]** |
|---|---|---|---|---|---|
| Free | 30 | 18 | 0.6 | 0.3 | 30 |
| Free | 40 | 24 | 0.3 | 0.1 | 30 |
| Immobilized | 40 | 30[a] | 2.6 | 0 | 30[b] |

[a] Calculated from enzyme load on the immobilization support, corresponds to $\nu_{max} = 1038$ [$10^2$ gh$^{-1}$g-support$^{-1}$].

[b] Calculated from characteristic of the column packing, corresponds to $D_C = 0.9$ [g-support ml$^{-1}$].

# 6. Results and discussion

The findings presented in this chapter describe predictions related to isothermal PC processes capable to separate conglomerate forming systems. The chapter is organized into three primary sections. In the first section, the application of the SCM developed in this thesis is discussed with respect to batch-wise PC. This involves comparing SCM predictions to experimental results, discussed considering two different case studies. For the first case study, the Population Balance Model (PBM) as described in Chapter 3 was used to create theoretical profiles for simulated experiments described in chapter 5 (part 1 of Table 5.2). In the second case study, real experimental data involving enantiomers of asparagine monohydrate were used as indicated in chapter 5 (part 2 of Table 5.2).

The second section presents the results of detailed sensitivity studies using the dimensionless version of SCM for the steady state of a continuous PC process. The reference parameters for these studies were partly based on the simulated experimental data from the previous section. The aim here is to qualitatively understand the influence of various thermodynamic, kinetic, and operational parameters on the course of this separation process.

The final third section reports on the use of SCM in developing process strategies for different configurations of PC integrated with the racemization process. This part utilizes the experimental data from the first section and the racemization kinetics illustrated in Table 5.3.

## 6.1. SCM predictions for batch PC

### 6.1.1. Case study 1: D-/L-threonine in water

Three simulated "experiments" were generated by combining a thorough population balance model with previously described crystallization kinetics (Table 5.1 of chapter 5). We have used higher resolution numerical schemes (Koren 1993) explained in detail in chapter 3 to solve the PBEs.

#### 6.1.1.1. Parameter estimation

For different initial supersaturations, three “simulated” experiments were developed based on the PBE model. The crystallization temperature $T_{cryst}$ was fixed at 18°C. Three supersaturations were generated by three distinct, $T_{sat}$ and thus, different initial saturation concentrations. The findings of Table 5.2's "experiments" $I_{(1)}$ − $III_{(1)}$ were used to estimate, $t_{stop}$ and, $k^{eff}$. Figures 6.1 and 6.2 illustrate the results of this analysis. For validation, additional simulated "experiments" $IV_{(1)}$ and $V_{(1)}$ were developed; they will be discussed in more detail later in this study. The methods outlined in section 4.1.4 for estimating the free parameters of SCM was used. Table 6.1 shows the corresponding parameters, and figure 6.1

depicts the correlations. As anticipated, $t_{stop}$ reduces with increasing, $S^0$ since a comparatively higher driving force for crystallization enables the main nucleation of the non-target enantiomer to occur earlier. Since it was observed that the order of crystallization kinetics, $n^{eff}$ was close to unity, $n^{eff}$ = 1 was employed in the SCM. This simplifies minimization for parameter estimation, as only the effective crystallization rate constant must be separately fitted to each experiment. Using equation 27, the values of $k^{eff}$ were connected with initial supersaturation. Table 6.1 contains all estimated parameters. In the range covered by the "experiments," the effective crystallization rate increased proportionately with initial supersaturation, confirming the assumption of, $n^{eff}$ = 1 and the linear relationship on supersaturation.

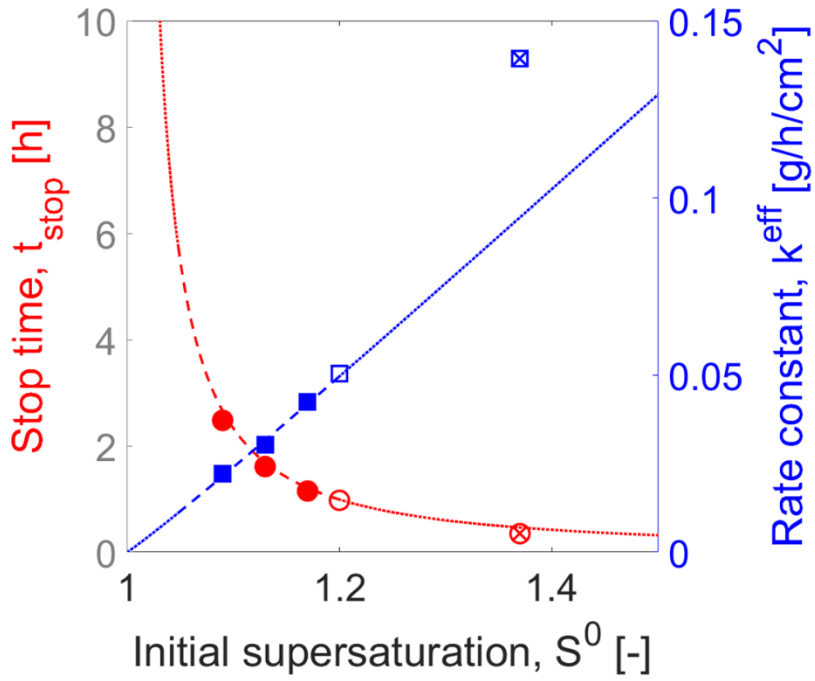


**Figure 6.1**. Case Study 1: The figure illustrates the relationship between the SCM parameters: stop time $t_{stop}$ and the effective rate constant $k^{eff}$, with respect to the initial supersaturation $S^0$. The curves represent correlation functions detailed in equations 4.18 and 4.19, while the symbols indicate results from simulated "experiments" using a PBM as shown in Table 5.2 of chapter 5 for experiments $I_{(1)}$ to $III_{(1)}$. The red line with circles corresponds to the $t_{stop}$, and the blue line with squares denotes the effective rate constant $k^{eff}$. Symbols that are empty or crossed signify additional PBM experiments conducted for validation when $S^0$ is near the limit or beyond the range of the MZ, corresponding to experiments $IV_{(1)}$ and $V_{(1)}$ in Table 5.2 of chapter 5. The dashed lines show the operational range of the SCM up to the MZ. All "PBM experiments" were performed at a crystallization temperature ($T_{cryst}$) of 18°C and with seed mass ($m_{seeds}$) of 1.0 g.

**Table 6.1**. Shortcut model parameters for case study 1: simulated “experiments” with system D-/L-threonine in water. Parameters were estimated following the strategy described in chapter 4 (section 4.1.4). The table was divided in three sections corresponding to preliminary

calibration, estimated parameters ($t_{stop}$, $k^{eff}$ and $n^{eff}$ ) and correlation parameters (eq 4.18 and 4.19).

| Parameter | Experiment[a] | Value | Unit |
|---|---|---|---|
| $k_\alpha$ | | 0.068 | $\mathrm{g\,g^{-1}}$ |
| $t_{stop}$ | $\mathrm{I_{(1)}}$ | 2.65 | h |
| | $\mathrm{II_{(1)}}$ | 1.69 | h |
| | $\mathrm{III_{(1)}}$ | 1.21 | h |
| $n^{eff}$ | | 1.0 | – |
| $k^{eff}$ | $\mathrm{I_{(1)}}$ | 0.022 | $\mathrm{g\,h^{-1}\,cm^{-2}}$ |
| | $\mathrm{II_{(1)}}$ | 0.030 | $\mathrm{g\,h^{-1}\,cm^{-2}}$ |
| | $\mathrm{III_{(1)}}$ | 0.042 | $\mathrm{g\,h^{-1}\,cm^{-2}}$ |
| $a_t$ | | 0.14 | h |
| $b_t$ | | 1.23 | – |
| $a_k$ | | 6.182 | $\mathrm{g\,h^{-1}\,cm^{-2}}$ |
| $b_k$ | | 2.053 | – |
| $c_k$ | | 6.513 | – |

[a] Experimental conditions were described in chapter 5 (Table 5.2).

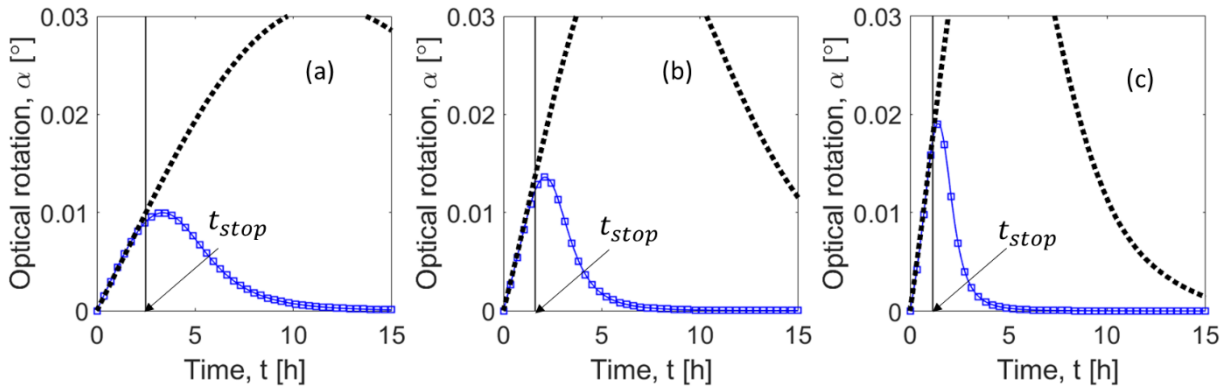


**Figure 6.2**. Case Study 1: Plot presents a side-by-side evaluation of SCM simulations against "experimental" data. PC profiles were constructed using a PBM depicted with blue lines and squares, for varying levels of initial supersaturation $S^0$: (a) 1.09, (b) 1.13, and (c) 1.17, as detailed in Table 5.2 of chapter 5 for experiments $\mathrm{I_{(1)}}$ through $\mathrm{III_{(1)}}$. The solid black curves represent the outcomes from the SCM up to the designated stop time $t_{stop}$, which is

highlighted by an arrow; the dotted curves offer an extrapolation of SCM predictions past the stop time. All PBM-generated profiles were calculated with a crystallization temperature ($T_{cryst}$) of 18°C and a seed mass ($m_{seeds}$) of 1.0 g.

#### 6.1.1.2. Illustration and validation

Figure 6.2 depicts a comparison of transients predicted by the PBM and the SCM. When crystallization of the counter enantiomer is prevented and product purity is retained, SCM exhibits extremely excellent agreement with PBM within the time frame of interest. Simulations beyond $t_{stop}$, represented in dotted curves, indicate higher variances, as predicted. Only data until $t_{stop}$ were utilized to optimize the shortcut model's parameters.

To assess the scope of application of the correlations, two further PBM simulation experiments were generated. Table 5.2 of chapter 5 presents the process conditions of experiments $IV_{(1)}$ and $V_{(1)}$. The results of experiment $IV_{(1)}$ (figure 6.1 empty symbols) demonstrated a good agreement between the correlation functions of the PBM-simulated experiment and those of the SCM. This validates the correlation's application to somewhat comparatively higher initial supersaturation values. Experiment $V_{(1)}$ results (crossed symbols in figure 6.1) were much more at contrast with SCM correlations, which was especially evident for the value of the effective rate constant $k^{eff}$. These results are also depicted in the time profiles of figure 6.3 (a) and (c). The model fits the "experiments" well when the correlations are not used and the parameters are determined directly by new fit of the SCM to PBM-generated transients (figures 6.3 (b) and (d)). It is important to note that the success of the simulated experiment $V_{(1)}$ can be attributed only to the fact that it was modeled using the population balance model. For initial supersaturations of threonine greater than 1.2, it is known that the process surpasses the metastable zone width (Lorenz, Perlberg, et al. 2006) and results in primary nucleation of the counter enantiomer. For experiment $V_{(1)}$, $S^0$ was measured to be 1.37, which exceeds the MZ limit.

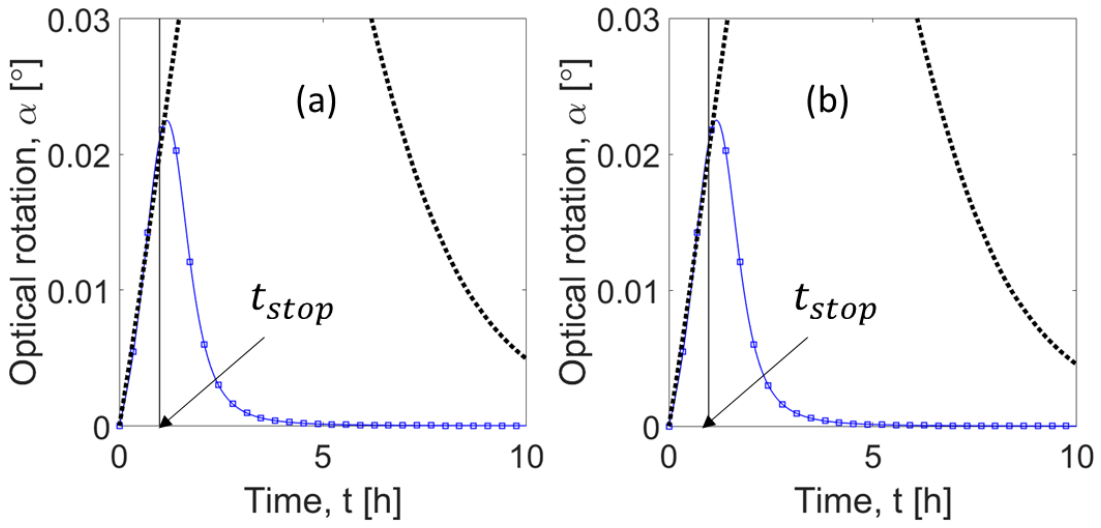

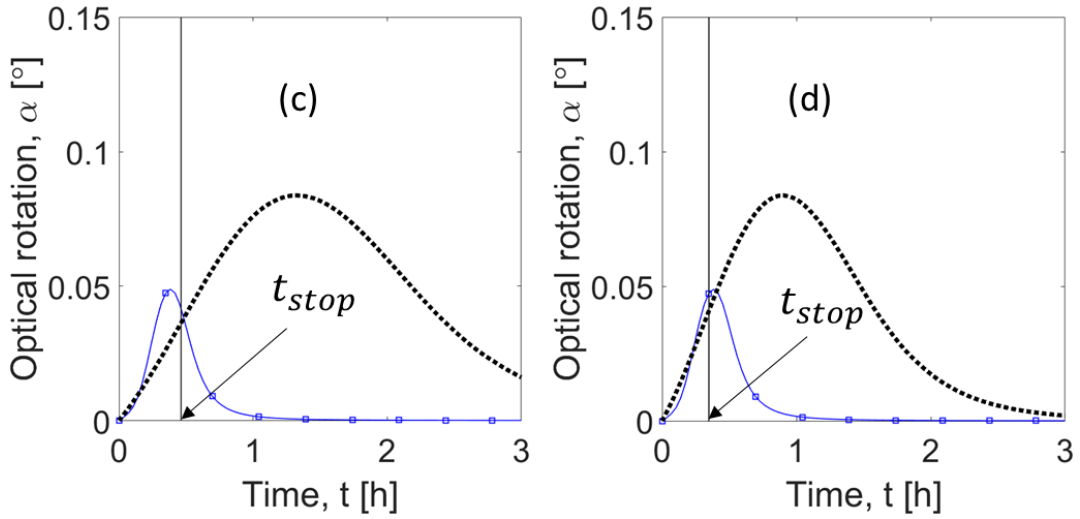


**Figure 6.3.** Case Study 1: The figure defines the application boundaries of the SCM by contrasting its outcomes with supplementary "experimental" observations. Profiles of PC were generated utilizing a PBM, shown by blue lines with circles. The simulations were conducted for supersaturations $S^0$ = 1.20 in plots (a) and (b) (as indicated in Table 5.2 of chapter 5, experiment $IV_{(1)}$), and $S^0$ = 1.37 in plots (c) and (d) as (in Table 5.2 of chapter 5, experiment $V_{(1)}$). The SCM findings are presented in plots (a) and (c) using previously determined parameters (refer to Table 6.1), and in (b) and (d) using parameters recalculated through a new fitting. All PBM profiles were generated under a uniform crystallization temperature ($T_{cryst}$) of 18°C and seed mass ($m_{seeds}$) of 1.0 g.

### 6.1.1.3. Evaluation of productivity

SCM was then used to estimate the influence of seed mass on productivity for a range of initial supersaturations in order to demonstrate the model's potential. The assumed dead time between two batches ($t_{dead}$ in eq. 3.40) was 1 hour. Figure 6.4 shows the results. For comparable results, the mass of seeds was measured relative to the highest theoretical product mass ($m_{max}$) that can be thermodynamically obtained. $m_{max}$ is dependent on the solubility of the compound in its initial and saturation states, as described in eq. 3.42. The seed mass range was set between 1 to 10 % of the maximum theoretical product.

As predicted, raising the ratio $m_{seed}/m_{max}$, will result in higher productivity. To develop a cost-effective process, it is essential to consider the tradeoff between a higher investment in seeds, an increase in productivity, and a reduction in process robustness, since the faster concentration depletion raises the risk of uncontrollable fast nucleation. Figure 6.4's profiles also demonstrate that productivity rises with increasing $S^0$. In practice, relatively high initial supersaturations are difficult to execute, which is a constraint when designing PC. Clearly, a significant factor in this kinetically driven process is the width of the metastable zone (MZ). This property is unique to the specific compound and process conditions. The MZ limits of threonine (Lorenz, Perlberg, et al. 2006; Sapoundjiev et al. 2006) are indicated by the dashed curves for initial supersaturations greater than 1.2 in figure 6.4. Exceeding this empirical range

increases the risk of primary nucleation, lowering product purity and reducing process predictability. Productivity can only be evaluated based on the range of experiments performed for parameter estimation. In this case study, all process transients evaluated for parameter estimation were produced at the same crystallization temperature. Thus, the limit of the metastable zone remains constant. To evaluate the process at a different temperature, further experimental data are required. In this region, the productivity of PC for resolving enantiomers of threonine in batch mode ranges from $Pr$ = 0.2 – 2.0 g $h^{-1}$ $l^{-1}$ (eq 3.40).

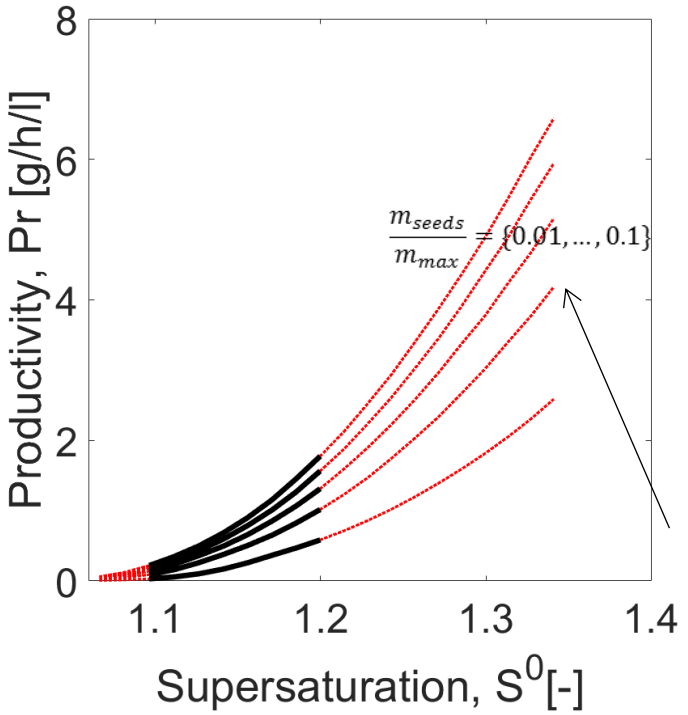


**Figure 6.4**. Case Study 1: Productivity is calculated via the SCM using eq. 3.40, with a focus on the effect of seed mass. The solid black curves illustrate the applicable range of the SCM under the experimental conditions examined, where its lower boundary is defined by the range of initial supersaturation $S^0$ studied in the "experiments" and its upper boundary is constrained by the MZ, represented by red dotted curves. The crystallization temperature ($T_{cryst}$)) was maintained at 18°C, and the ratios of seed mass to maximum mass ($m_{seeds}/m_{max}$) varied across the series: 0.010, 0.032, 0.055, 0.077, and 0.100.

In this analysis, it is assumed that $t_{stop}$ is independent of $m_{seeds}$. This appears to be valid only within a narrow deviation range from the reference experiment. This is a rather crude assumption that may be simply relaxed if additional data from experiments changing the initial crystal radius, initial crystal number, or both are provided. This analysis is beyond the scope of this research.

### 6.1.2. Case study 2: D-/L-asparagine monohydrate in water

Experiments were conducted and presented in table 5.2 of chapter 5 with asparagine monohydrate to further validate the model. Since this compound forms a hydrate, the relevant ternary phase diagram, shown in figure 3.1 (b), was considered while calculating driving forces. In addition, eq. 4.6 makes a significant contribution as it accounts for the transit of solvent molecules from the liquid to the solid phase.

### 6.1.2.1. Parameter estimation

Figure 6.5 illustrates the stop time over initial supersaturation for experiments $I_{(2)}$ – $III_{(2)}$ (Table 5.2 of chapter 5). As predicted and observed in case 1, the greater the initial supersaturation values, the shorter the stop time. Eq 4.18 was used to correlate $t_{stop}$ and $S^0$. Table 6.2 shows the resulting parameters. In addition, the table provides estimated values for effective crystallization order and effective rate constant. Unlike the last case $n^{eff}$ is significantly more than 1. This indicates a deviation from linearity with respect to supersaturation, which is also evident in the correlation between the effective rate and initial supersaturation (blue curves in Figure 6.1 and Figure 6.5). In contrast to the previous case, the effective crystallization rate constant for asparagine falls as initial supersaturation increases within the investigated range. $k^{eff}$ vs. $S_0$ has a profile that is more complicated than the linear profile seen for threonine. For this case all four parameters ($n^{eff}, k_I^{eff}, k_{II}^{eff}, k_{III}^{eff}$) are fitted together and $n^{eff}$ is estimated as a compromise considering all experimental results. The effectiveness of the correlations indicates that the model is capable of accounting for more complex nonlinear kinetics.

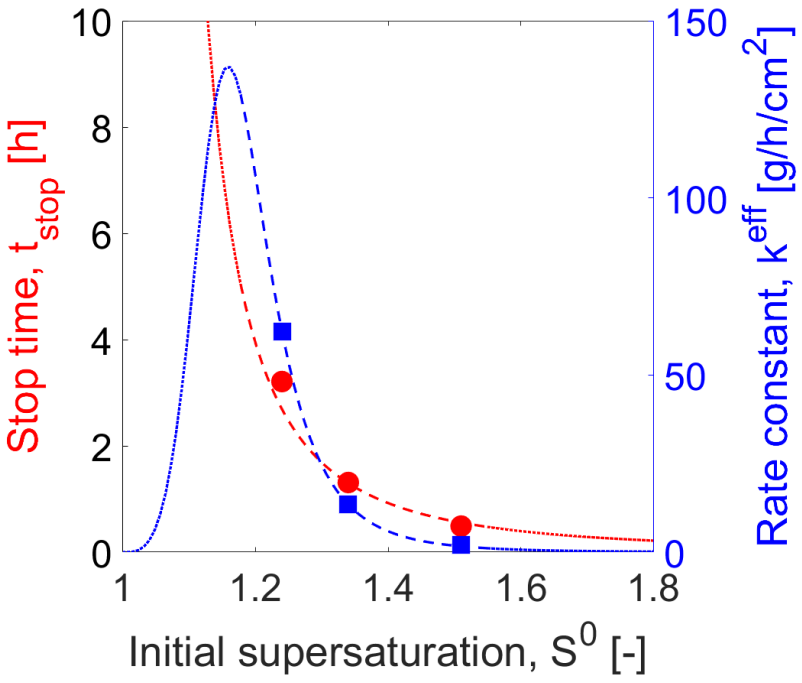


**Figure 6.5**. Case Study 2: The figure analyzes the relationship between the SCM parameters stop time $t_{stop}$ and the effective rate constant $k^{eff}$ in relation to the initial supersaturation $S^0$. The solid symbols represent empirical data derived from experiments $I_{(2)}$ to $III_{(2)}$ as

detailed in Table 5.2 of chapter 5. The lines correspond to the correlation functions expressed in eqs. 4.18 and 4.19. red curves with circles signify the stop time $t_{stop}$, while blue curves with squares indicate the effective rate constant $k^{eff}$. The dashed lines define the operational domain of the SCM. All experiments were carried out at a crystallization temperature ($T_{cryst}$) of 30°C, with a uniform seed mass ($m_{seeds}$) of 0.2 g.

**Table 6.2**. Shortcut model parameters for case study 2, system D-/L-asparagine monohydrate in water. Parameters were estimated following the strategy described in chapter 4, section 4.1.4. The table was divided in three sections corresponding to preliminary calibration, estimated parameters ($t_{stop}$, $k^{eff}$ and $n^{eff}$ ) and correlation parameters (eq 4.18 and 4.19).

| Parameter | Experiment[a] | Value | Unit |
|---|---|---|---|
| $k_\alpha$ | | 0.048 | $\mathrm{g\,g^{-1}}$ |
| $t_{stop}$ | $\mathrm{I_{(2)}}$ | 3.14 | h |
| | $\mathrm{II_{(2)}}$ | 1.37 | h |
| | $\mathrm{III_{(2)}}$ | 0.48 | h |
| $n^{eff}$ | | 6.10 | – |
| $k^{eff}$ | $\mathrm{I_{(2)}}$ | 62.3 | $\mathrm{g\,h^{-1}\,cm^{-2}}$ |
| | $\mathrm{II_{(2)}}$ | 13.4 | $\mathrm{g\,h^{-1}\,cm^{-2}}$ |
| | $\mathrm{III_{(2)}}$ | 1.97 | $\mathrm{g\,h^{-1}\,cm^{-2}}$ |
| $a_t$ | | 0.095 | h |
| $b_t$ | | 2.46 | – |
| $a_k$ | | 20.8 | $\mathrm{g\,h^{-1}\,cm^{-2}}$ |
| $b_k$ | | 4.41 | – |
| $c_k$ | | 0.17 | – |

[a] Experimental conditions were described in Table 5.2.

### 6.1.2.2. Illustration and validation

Figure 6.6 illustrates a comparison between the asparagine monohydrate experiments and the SCM simulations. Again, the dotted lines represent the extrapolation of the shortcut model after the stop time, which incorporates eq. 4.5 and 4.8. They are shown for reference only and are not intended to fit experimental data. Experiments and simulations match well in the region of interest, with a relatively conservative estimation of the transient profile for

larger values of $S^0$. This indicates a minor underestimating of productivity, which is favorable for the design of processes. The profile (a) with a lower initial supersaturation value resulted in a better model-to-experiment fit. This variation in fitting between profiles (a)−(c) is partially due to the fact that all parameters, reaction rates $k_I^{eff}$, $k_{II}^{eff}$, $k_{III}^{eff}$ and order $n^{eff}$ are simultaneously optimized (eq. 4.16).

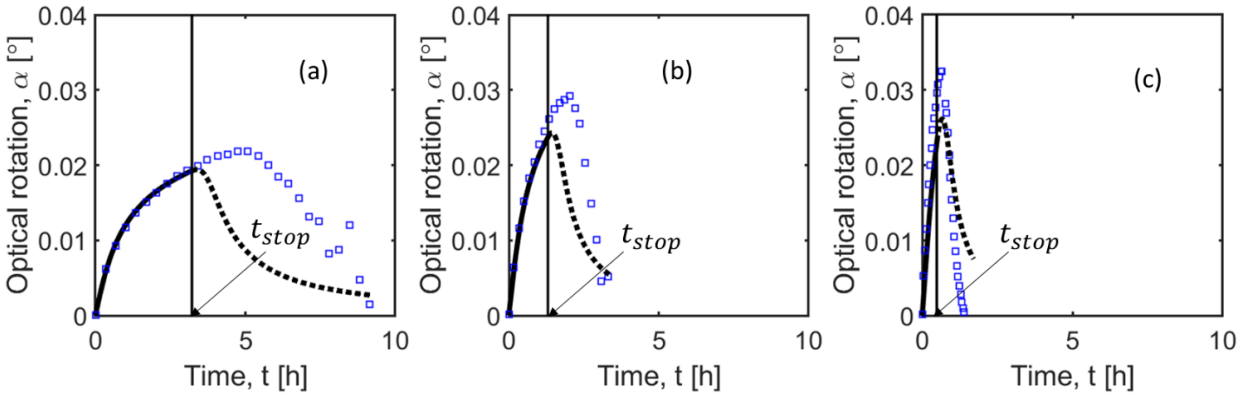


**Figure 6.6**: Case Study 2: This comparison reveals the alignment between SCM simulations and experimental data. The experimental profiles are represented by blue squares for different initial supersaturations $S^0$: (a) 1.24, (b) 1.34, and (c) 1.51, with the specific conditions detailed in Table 5.2 of chapter 5 for experiments $I_{(2)}$ to $III_{(2)}$. The SCM's predictions are depicted by the solid black curve, which continues up to the stop time $t_{stop}$, marked by an arrow. For illustrative purposes, dotted lines project the SCM outcomes beyond the stop time. All the experiments were conducted at a crystallization temperature ($T_{cryst}$) of 30°C with seed mass ($m_{seeds}$) set at 0.2 g.

### 6.1.2.3. Evaluation of productivity

Figure 6.7 shows the results of computing the productivity of PC to resolve asparagine monohydrate as predicted by SCM for various initial supersaturation. Similar to the previous case study, the effect of normalized seed mass was studied. Similar to the trends seen in Figure 6.4 for threonine, the productivity improves with an increase in seed mass or initial supersaturation. For comparable initial supersaturation values, threonine provides higher productivity. However, due to its solubility and metastable zone limitations, asparagine can provide higher initial supersaturation levels. Considering the individual temperature ranges evaluated for each compound, threonine is more strongly limited by the metastable solubility (Figure 6.4). Such high $S^0$ conditions as those applied in asparagine experiments are unlikely to be successful with threonine. The MZ limits of asparagine monohydrate at $T_{cryst}$ = 30°C extend beyond the initial supersaturation values of 1.5. At $T_{cryst}$ = 30°C, the productivity range for asparagine monohydrate is $Pr$ = 0.5 – 4.0 g $h^{-1}$ $l^{-1}$.

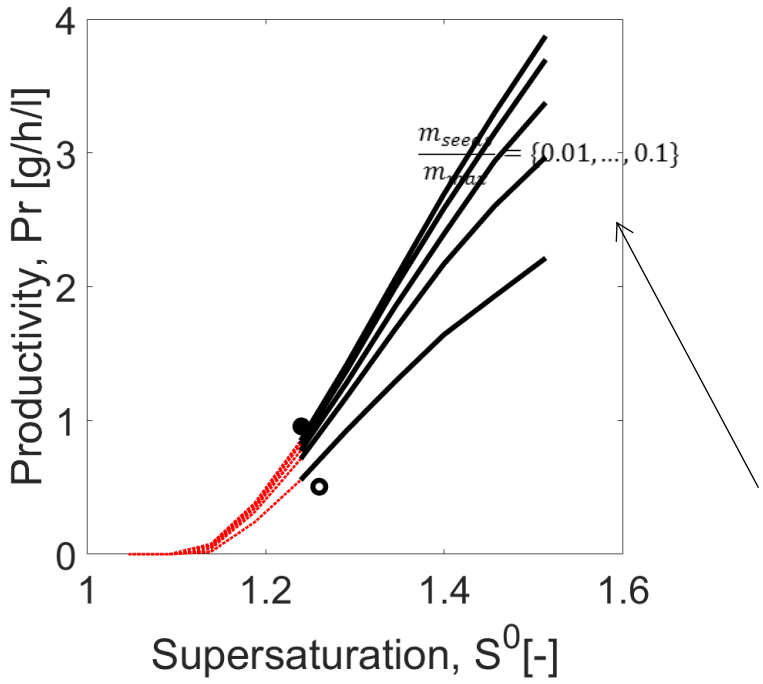


**Figure 6.7.** Case Study 2: The figure explores the estimated productivity as predicted by the SCM, with a focus on the influence of varying seed mass. The solid curves show the scope of the SCM under the experimental conditions considered, while the red dotted lines mark the lower boundary of initial supersaturation $S^0$ addressed in the experiments. The crystallization temperature ($T_{cryst}$) is set at 30°C, with the ratios of seed mass to maximum mass ($m_{seeds}/m_{max}$) indicated by values: 0.010, 0.032, 0.055, 0.077, and 0.100. Full circles correspond to productivity estimates at $T_{cryst}$ = 30°C from experiment $I_{(2)}$, and empty circles represent those at 25°C from experiment $IV_{(2)}$, illustrating the productivity at different crystallization temperatures

### 6.1.2.4. Including temperature effects in the SCM

Three experiments and simulations have thus far been described utilizing isothermal batch PC with identical crystallization temperatures, 18°C for threonine and 30°C for asparagine monohydrate. The proposed correlations for $t_{stop}$ (eq 4.18) and $k^{eff}$ (eq 4.19) are dependent only on initial supersaturation. For process conditions where $T_{cryst}$ varies, the effective rate and stop time will also change with temperature.

To determine the effect of temperature on the SCM's parameters, an extra PC experiment was conducted at a lower crystallization temperature. Its conditions were shown in number $IV_{(2)}$, Table 5.2 of chapter 5. This is an additional experiment to those proposed in step 2 of section 4.1.4. On the basis of solubility data, the experimental conditions were selected with $S^0$ = 1.26, equivalent to $S^0$ = 1.24 in experiment $I_{(2)}$, but with a lower crystallization temperature $T_{cryst}$ of 25°C. In both cases the $\Delta T = T_{sat} - T_{cryst}$ was equal to 5 K. Therefore, we assumed that initial supersaturation values were sufficiently close such that the influence

of this parameter could be neglected and temperature effects could be evaluated. Figure 6.8 depicts the experimental profiles and simulations of experiments $I_{(2)}$ and $IV_{(2)}$. The SCM plot (solid and dotted curves) for experiment $I_{(2)}$ is identical to the one shown in Figure 6.6 (a). For experiment $IV_{(2)}$, $t_{stop}$ was estimated as shown in section 4.1.4.1 and $k^{eff}$ was determined from the experimental data again using the MATLAB fmincon function. The values are shown in Table 6.3. As predicted, the process with a higher $T_{cryst}$ exhibited a higher $k^{eff}$ and a lower $t_{stop}$ for similar initial supersaturation values. The effective rate constant for experiment $I_{(2)}$ was over three times that of experiment $IV_{(2)}$, although the process reached $t_{stop}$ in around half the time. Using eq. 4.20 along with $k^{eff}$ and $T_{cryst}$ from experiments $I_{(2)}$ and $IV_{(2)}$, the effective activation energy $E^{eff}$ and the pre factor, $k_0^{eff}$ values were calculated. The results are shown in Table 6.3.

A minimum of three experiments in a range of $T_{cryst}$ would be required to further analyze the correlation parameters and assess quantitatively the temperature dependence in $t_{stop}$. The objective of experiment $IV_{(2)}$ was to determine the behavior of the trends of parameters at different crystallization temperatures. In this paper, these affects will not be explored in detail. However, the productivity of experiments $I_{(2)}$ and $IV_{(2)}$ was assessed to compare the two processes, as shown in figure 6.7. $Pr$ = 0.95 g $l^{-1}$ $h^{-1}$ for experiment $I_{(2)}$ (solid circle) and $Pr$ = 0.50 g $l^{-1}$ $h^{-1}$ for experiment $IV_{(2)}$ (empty circle) are the corresponding values. For processes with similar initial supersaturation $S^0$, the crystallization rate rises with an increase in crystallization temperature $T_{cryst}$, resulting in improvement in productivity.

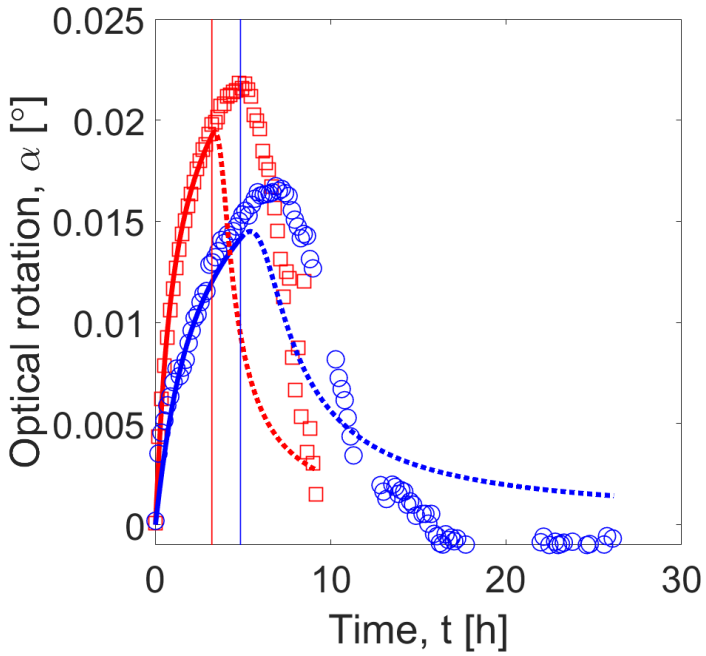


**Figure 6.8**. Case Study 2: This figure assesses the impact of crystallization temperature on SCM parameters. red squares represent data from experiment $I_{(2)}$ with an initial supersaturation $S^0$ of 1.24 and a crystallization temperature $T_{cryst}$ of 30°C; blue circles correspond to data from experiments $IV_{(2)}$ with $S^0$ of 1.26 at a lower $T_{cryst}$ of 25°C. Solid

curves illustrate the SCM simulations up to the determined stop time $t_{stop}$, while dotted curves extend the simulation predictions beyond $t_{stop}$, offering insight into the potential trajectory of the crystallization process under different temperature conditions.

**Table 6.3**. Shortcut model parameters for system D-/L-asparagine monohydrate in water. Experiments were performed at different crystallization temperatures, $T_{cryst}$: experiment $I_{(2)}$ at 30°C and experiment $IV_{(2)}$ at 25°C.

| Parameter | Experiment[a] | Value | Unit |
|---|---|---|---|
| $t_{stop}$ | $I_{(2)}$ | 3.14 | h |
| | $IV_{(2)}$ | 4.85 | h |
| $k^{eff}$ | $I_{(2)}$ | 62.3 | $\mathrm{g\ h^{-1}\ cm^{-2}}$ |
| | $IV_{(2)}$ | 16.3 | $\mathrm{g\ h^{-1}\ cm^{-2}}$ |
| $E^{eff}$ | | 201 | $\mathrm{kJ\ mol^{-1}}$ |
| $k_0^{eff}$ | | $3.27 \times 10^{36}$ | $\mathrm{g\ h^{-1}\ cm^{-2}}$ |

[a] Experimental conditions indicated in Table 5.2 of chapter 5.

## 6.2. Dimensionless SCM predictions for continuous PC

In the section, we will present key findings of the SCM model that was introduced in a systematical parametric study in section 4.2 of chapter 4 to demonstrate the effects of specific key parameters on the progression of the steady state of a continuous PC process carried out in an isothermal tubular crystallizer.

### 6.2.1. Selection of parameters for dimensionless SCM

Table 6.4 illustrates the reference data utilized in simulations with the SCM derived in section 4.2 of chapter 4. These data were selected in part based on Table 5.2 of chapter 5, devoted to the crystallization of threonine enantiomers. The process parameters selected for a systematic study are listed in Tables 6.4 and 6.5. Table 6.5 is a summary of dimensionless parameters considered to conduct various simulation experiments.

It should be noted that for the two enantiomers, the Damköhler numbers and the solid phase Bodenstein numbers vary due to differences in the seed size-dependent equilibrium radii (eq. 4.31). The relationship between the Damköhler numbers for both enantiomers can be expressed as follows:

$$Da_2 = Da_1 \left( \frac{R_{eq,2}}{R_{eq,1}} \right)^2 \quad 6.1$$

Furthermore, for a specific value of $D_{ax,S}$, which measures the back-mixing in the solid phase, there exists a consistent relationship between $Bo_{S,1}$ and $Bo_{S,2}$:

$$Bo_{S,2} = Bo_{S,1} \left( \frac{R_{eq,2}}{R_{eq,1}} \right) \quad 6.2$$

In our specific case, using the selected parameters (table 6.4), both sets of numbers - the Damköhler numbers (eq. 4.40) and the solid phase Bodenstein numbers (eq. 4.58) - show a high degree of similarity. Given that their influence on the process is significant only until $t_{stop}$, we further simplified the parameter set by equating $Da_2 = Da_1$ and $Bo_{S,2} = Bo_{S,1}$.

**Table 6.4.** Thermodynamic and kinetic parameters (related to the date given in Table 5.2 of chapter 5 for D-/L-Threonine in water) complemented by reference process parameters:

| **Parameters** | **Reference Values** |
|---|---|
| $T$ | 18 °C |
| $\rho_L$ | 1.00 $g\ cm^{-3}$ |
| $\rho_S$ | 1.25 $g\ cm^{-3}$ |
| $c_{sat}$ | 0.074 $g\ cm^{-3}$ |
| $k^{eff}$ (SCM parameter) | 0.03 $g\ h^{-1}\ cm^{-2}$ |
| $n^{eff}$ (SCM parameter) | 1 |
| $t_{stop}$ (SCM parameter) | 1.7 $h$ |
| $c_{1,in} = c_{2,in}$ | 0.0925 $g\ cm^{-3}$ |
| $R_{1,in}$ | 0.005 cm |
| $R_{2,in}$ | 1e-8 cm |
| $R_{1,eq}$ | 0.0110 cm |
| $R_{2,eq}$ | 0.0108 cm |
| $L$ | 5100 $cm$ |
| $u$ | 1000 $cm\ h^{-1}$ |
| $t_{PFTC}$ | 5.1 $h$ |
| $z_{stop}$ (eq. 5.46) | 1700 $cm$ |
| $\hat{z}_{stop}$ (eq. 5.47) | 0.333 |
| $u_{stop}$ (eq. 5.48) | 3000 $cm\ h^{-1}$ |
| $n_{1,S} = n_{2,S}$ (eq. 5.3) | 2825 $(cm^{-3})$ |
| $k_1^{char} = k_2^{char}$ (eq. 5.15) | 14000 $(h^{-1}\ cm^{-2})$ |
| $\dot{m}_{1,seeds}$ (eq. 5.12) | 0.37 g $h^{-1}$ |
| $\dot{m}_{max}$ (eq. 5.14) | 3.7 g $h^{-1}$ |

| **Dimensionless parameters** | |
|---|---|
| $S_{1,in} = S_{2,in} = S_{in}$ | 1.25 |
| $Da_1$ (eq. 5.19) | 9.1 |
| $\hat{c}_{1,\mathrm{in}}$ (eq. 5.26) | 0 |
| $\hat{c}_{2,\mathrm{in}}$ (eq. 5.26) | 0 |
| $\hat{R}_{1,\mathrm{in}}$ (eq. 5.26) | 0.45 |
| $\hat{R}_{2,\mathrm{in}}$ (eq. 5.26) | 1e-6 |
| $\hat{V}_{max,1}$ (eq. 5.11) | 0.30 |
| $\hat{V}_{max,2}$ (eq. 5.11) | 0.33 |
| $Bo_{i,L}$ (eq. 5.31) | 100 |
| $Bo_{1,\mathrm{S}}$ (eq. 5.37) | 100 |

**Table 6.5.** Simulation parameters for the studies described in section 6.2.2. Studies 1-5 shows the effect of changing key model parameters on the performance of the process. Study 6 illustrates the effect of dispersion in both the liquid and solid phase, respectively.

| **Case Studies** | **Parameter** | **Value** | **Comments** |
|---|---|---|---|
| Study 1 "$Da_1$" | $Da_1$ | 0.1, 1, 3, 6, **9.1**, 20 | To study the effect of Damköhler number |
| Study 2 "$k^{char}$" | $k^{char}$ $[h^{-1}\ cm^{-2}]$ | 7000, **14000**, 28000 | To study the effect of characteristic crystallization rate constant |
| Study 3 "$n^{eff}$" | $n_i^{eff}$ | 0.5, **1**, 2 | To study the effect of effective order of crystallization |
| Study 4 "$S_{in}$" | $S_{in}$ | 1.12, **1.25**, 1.38 | To study the effect of initial concentration |
| Study 5 "$\widehat{M}_{seeds}$" | $\widehat{M}_{seeds}$ | 0.05, **0.1**, 0.15 | To study the effect of initial seed mass (Eq. 23) |
| Study 6 "Back-mixing" | $Bo_{i,L}$ | 1, 5, 10, **100**, ∞ | To study the effect of dispersion in the liquid phase |
| | $Bo_{1,S}$ | ∞**, 100**, 10, -10, -100 | To study the effect of dispersion in the solid phase |

**Reference parameters in bold**

## 6.2.2. Numerical solution and results of parametric study

The overall mass balance equations of the SCM for continuous steady-state Plug Flow type Crystallization (PFTC), which takes into account the different mixing behaviour, were

methodically analysed. Eqs. 4.53 and 4.59, were combined with the boundary conditions given in eqs. 4.62 and 4.65. For this analysis, the length of the crystallizer was segmented into 200 equal parts, which was found to be sufficient to precisely solve the resulting non-linear algebraic equations as described in appendix A1 where the derivation is thoroughly explained. This was solved using the "fsolve" function, a component of MATLAB (Mathworks M 2017) optimization toolbox.

Furthermore, we addressed the mass balance equations relevant to scenarios with no back-mixing (eqs. 4.41 and 4.46), applying boundary conditions from eq. 4.47 and employing the "ODE 15s" solver in MATLAB (Mathworks M 2017).

The subsequent section of the study presents initial predictions for various cases, where the degree of back-mixing remains constant but other key parameters are changed. These parameters include the Damköhler number ($Da_1$), the characteristic rate constant for crystallization ($k^{char}$), the initial supersaturation level ($S_{in}$), the effective order of crystallization ($n^{eff}$), and the mass of the seed crystals ($\widehat{M}_{seeds}$). Following this, the study explores the impact of varying the Bodenstein numbers in both liquid and solid phases. This is compared against an ideal theoretical model that neglects back-mixing. The results focus on variations in concentration, crystal radii, and purity, and are presented in relation to the Damköhler number ($Da_1$, as per eq. 4.40) or the dimensionless time $\hat{\tau}$ (as per eq. 4.66).

### 6.2.2.1. Study "$\boldsymbol{Da_1}$" Effect of Damköhler number

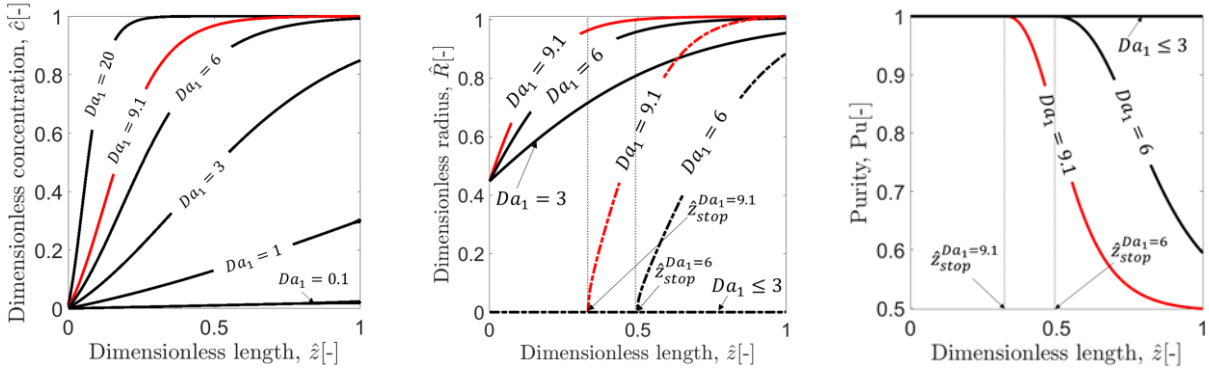


**Figure 6.9**. Left Plot: Shows the dimensionless concentrations ($\hat{c}$) of the target enantiomer across dimensionless length ($\hat{z}$), (eq. 4.37c). This plot illustrates variations for different Damköhler numbers ($Da_1$). Middle and Right Plot: Depict the dimensionless radii ($\hat{R}$) and Purity ($Pu$), respectively, for both enantiomers along the dimensionless length ($\hat{z}$). These plots are generated by keeping all parameters constant with only varying the velocity ($u$) at $Da_1 = 9.1,\ 6\ and\ 3$. The solid curve represents the preferred enantiomer, while the dashed curve corresponds to the counter enantiomer. The red curve represents the reference case.

The study investigates the impact of varying Damköhler numbers ($Da_1$) on the productivity and purity of the crystallization process, as illustrated in figure 6.9. The Damköhler number is

proportional to the residence time ($\hat{\tau}$) in the crystallizer. By modifying $Da_1$, which is achieved by altering the flowrate of both phases for a given crystallizer length, we can observe different outcomes in the crystallization process. The left section of figure 6.9 demonstrates that higher Damköhler numbers, correlating to lower flowrates, allow more time for the growth of the seeded particles of the desired enantiomer. This results in higher process productivity. This is linked to an accelerated increase in the dimensionless liquid phase concentration for larger $Da_1$ values. However, exceeding a certain threshold in terms of residence time leads to the undesired nucleation of the unwanted enantiomer, which then decreases the purity of the solid phase.

The middle plot of the figure highlights the evolution of crystal radii for both enantiomers at selected Damköhler numbers. Taking the reference case with $Da_1 = 9.1$ as an example, eq. 4.59 predicts the onset of counter enantiomer nucleation at a dimensionless position $\hat{z}_{stop}^{Da_1=9.1} = 0.33$. Beyond this point, the counter enantiomer also starts to grow, leading to a decline in purity, as shown in the right plot. To ensure high purity of the product at the end of the crystallizer of length $L$, it is necessary to adjust the Damköhler number. For a fixed length of the crystallizer, this involves increasing the flowrate. Reducing $Da_1$ to 6 prolongs the delay in counter enantiomer nucleation to $\hat{z}_{stop}^{Da_1=6}$=0.5, though at the expense of lower productivity. Completely avoiding the nucleation of the counter enantiomers within the crystallizer requires further increasing the velocity to the stop velocity ($u_{stop}$), as per eq. 4.69. In this scenario, a Damköhler number of $Da_1$ ≤ 3 ensures 100% purity but with reduced productivity.

The ideal operation point is thus at the highest possible Damköhler number that still maintains a velocity slightly above $u_{stop}$, balancing between maximizing productivity and ensuring the desired purity of the product.

#### 6.2.2.2. Study "$\boldsymbol{k^{char}}$": Effect of characteristic crystallization rate constant

In this study, the effect of varying the characteristic crystallization rate constant ($k^{char}$) on the crystallization process was explored through three different cases, each characterized by a distinct value of $k^{char}$ as detailed in Table 6.5. The characteristic crystallization rate constant is a crucial parameter that varies with each compound and solvent combination. To examine its impact, the reference value of $k^{char} = 14000\ h^{-1}\ cm^{-2}$ was modified by factors of 0.5 and 2, leading to changes in the Damköhler number ($Da_1$) for a constant tube length and flowrate. Consequently, the Damköhler numbers for these cases are $Da_1 = 4.5, 9.1$ and $17.8$ respectively.

As discussed in the previous section, in all these scenarios, the value of $Da_1$ exceeds 3, indicating that nucleation of the unwanted enantiomer will occur within the crystallizer. This

nucleation event, using the dimensionless residence time ($\hat{\tau}$) (eq. 4.66) as the process coordinate, happens at $\hat{\tau} = 1$, which is associated with a decline in purity for larger values.

Figure 6.10 in the study illustrates that larger $k^{char}$ values, which correspond to a faster transfer of the desired enantiomers from the liquid to the solid phase, result in steeper concentration gradients. However, these larger rate constants also lead to a more rapid decrease in purity once nucleation of the undesired enantiomer occurs, as depicted in the right part of figure 6.10.

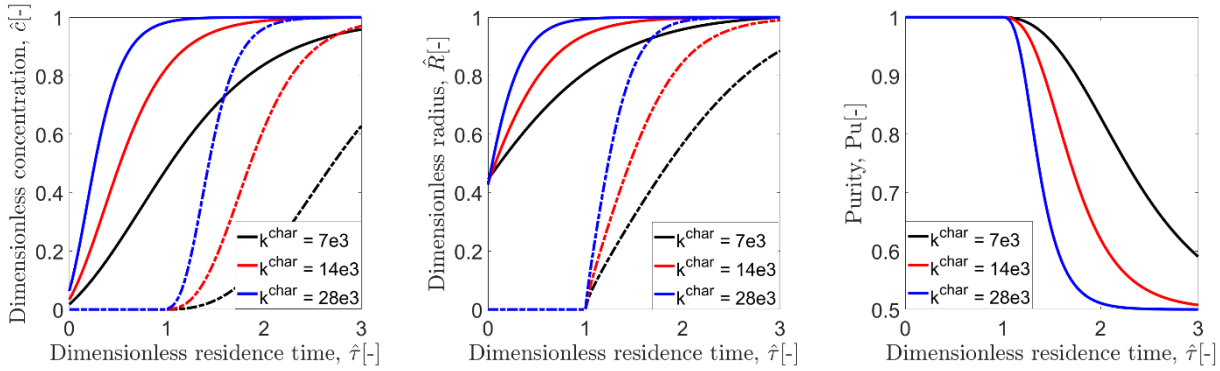


**Figure 6.10.** Dimensionless concentration ($\hat{c}$), radii ($\hat{R}$) and purity ($Pu$) estimated using SCM as a function of dimensionless residence time for different characteristic crystallization rate constant. Black curve: $k^{char} = 7000\ h^{-1}\ cm^{-2}$. Red curve: $k^{char} = 14000\ h^{-1}\ cm^{-2}$ . Blue curve: $k^{char} = 28000\ h^{-1}\ cm^{-2}$. Solid curve: Preferred enantiomer. Dashed curve: Counter enantiomer.

### 6.2.2.3. Study "$\boldsymbol{n^{eff}}$": Effect of effective growth rate order

The study involved examining three scenarios with varying effective orders of crystallization rate, analogous to the order of a reaction rate law commonly explored in reaction engineering. In reaction engineering, a higher reaction order typically leads to a more rapid decrease in reaction rate. Similarly, in the context of crystallization, a higher effective order of crystallization results in a quicker drop in the crystallization rate, as depicted in Figure 6.11.

During these analyses, the potential impact of effective growth kinetics on the stop time $t_{stop}$ was not considered. However, the results reveal that when nucleation occurs, maintaining larger crystallization rates for smaller orders effectively narrows the window for harvesting the product. This is due to the impact of the crystallization of the unwanted enantiomers on the overall process, particularly noticeable in the right part of the figure. As mentioned, these plots offer an analogy to the effect of reaction orders in chemical reaction engineering as described by (Garside and N.S. 1984).

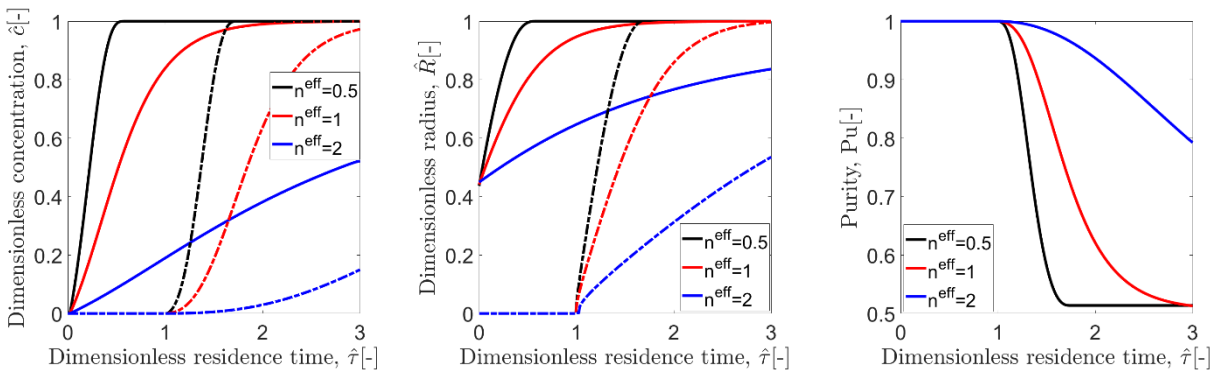


**Figure 6.11**. Dimensionless concentration ($\hat{c}$), radii ($\hat{R}$) and purity ($Pu$) estimated using SCM as a function of dimensionless length ($\hat{z}$) varying the order of crystallization ($n^{eff}$). Black curve: $n^{eff} = 0.5$. Red curve: $n^{eff} = 1$ and blue curve: $n^{eff} = 2$. Solid curve: Preferred enantiomer. Dashed curve: Counter enantiomer.

### 6.2.2.4. Study "$S_{in}$": Effect of initial supersaturation

In the process of preferential crystallization, one of the critical operating parameters is the initial supersaturation level at the crystallizer inlet. This factor serves as the driving force for transitioning the desired enantiomers from the liquid to the solid phase. Figure 6.12 shows results for three distinct initial supersaturation levels. These results incorporate the impact of supersaturation on the stop time $t_{stop}$ based on an empirical relationship described in eq 4.18(Carneiro et al. 2019). Adjusting the reference value for initial supersaturation by ±50% is correlated with a corresponding change in the reference $t_{stop}$ by approximately ±25%. This modification is in line with the experimental observations reported in table 6.1 of section 6.1.1.1.

The data in figure 6.12 are plotted against the dimensionless residence time (eq. 4.66). It is observed that higher initial supersaturation levels lead to quicker crystallization of the target enantiomers. However, this faster rate is coupled with a reduction in $t_{stop}$ and, consequently, an earlier increase in the dimensionless concentrations of the non-target enantiomers. This is evident from the left part of the figure, which shows a rise in counter enantiomers' concentration, and the middle and right parts, which indicate contamination in the solid product phase.

Therefore, operating at higher initial supersaturation not only speeds up the crystallization of the desired enantiomers but also increases the risk of early nucleation and growth of unwanted enantiomers. This can potentially compromise the purity of the final product. The study thus highlights a trade-off inherent in the process: while higher supersaturation can enhance productivity, it also carries a heightened risk of reducing product purity, underscoring the need for careful optimization of supersaturation levels in preferential crystallization processes.

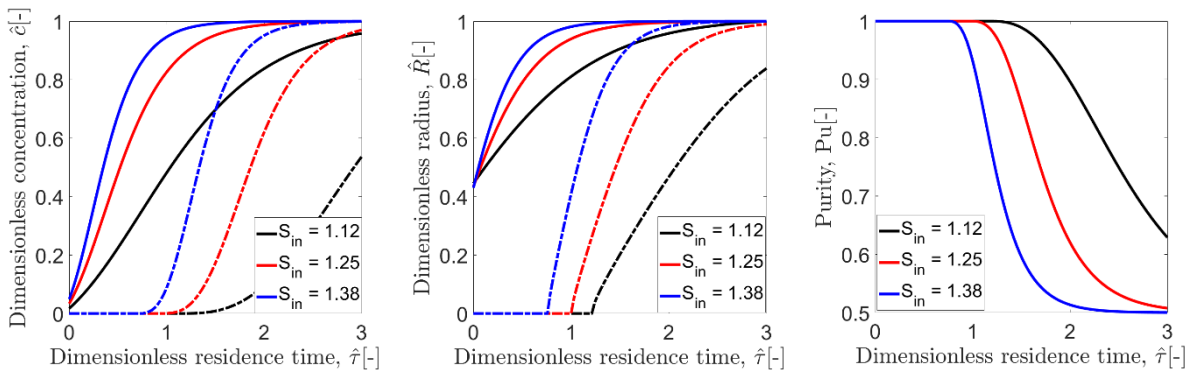


**Figure 6.12**: Dimensionless concentration ($\hat{c}$), radii ($\hat{R}$) and purity ($Pu$) is estimated using SCM as a function of Damköhler for different initial supersaturation. Black curve: $S_{in} = 1.12$ ($t_{stop} = 2.1\ h$). Red curve: $S_{in} = 1.25$ ($t_{stop} = 1.7\ h$). Blue curve: $S_{in} = 1.38$ ($t_{stop} = 1.3\ h$). Solid curve: Preferred enantiomer. Dashed curve: Counter enantiomer.

### 6.2.2.5. Study "$\widehat{M}_{seeds}$": Effect of relative seed masses

In the Preferential Crystallization (PC) process, the mass flux of seed crystals, particularly of the desired enantiomers is a pivotal parameter. The study focused on three scenarios with varying normalized initial seed masses $\widehat{M}_{seeds}$. The baseline or reference case set $\widehat{M}_{seeds}$ at 0.1, representing 10% of the maximum theoretical product mass as per eq. 4.34. The other two scenarios examined $\widehat{M}_{seeds}$ values of 0.05 and 0.15, respectively. While other parameters remained constant, the radius of the seeded enantiomers particles was adjusted to modify the seed mass while maintaining the number of seed particles constant ($\hat{R}_{1,\text{in}}$= 0.35, 0.45, 0.5).

The study reveals that higher initial seed masses increase the surface area available for the target enantiomers to grow, thereby increasing the overall crystallization rate. This relationship is clearly illustrated in figure 6.13. Consequently, operating with higher initial seed masses is generally advantageous for enhancing productivity in the PC process.

However, this approach has a significant trade-off. An increase in the initial seed mass leads to a more rapid growth in the particle radii of the unwanted enantiomers. This phenomenon is observed in the middle section of figure 6.13 and is associated with a faster decline in the purity of the product. Essentially, while a higher seed mass can boost the crystallization rate and productivity, it also increases the risk of contamination by the unwanted enantiomers, impacting the overall purity of the final product.

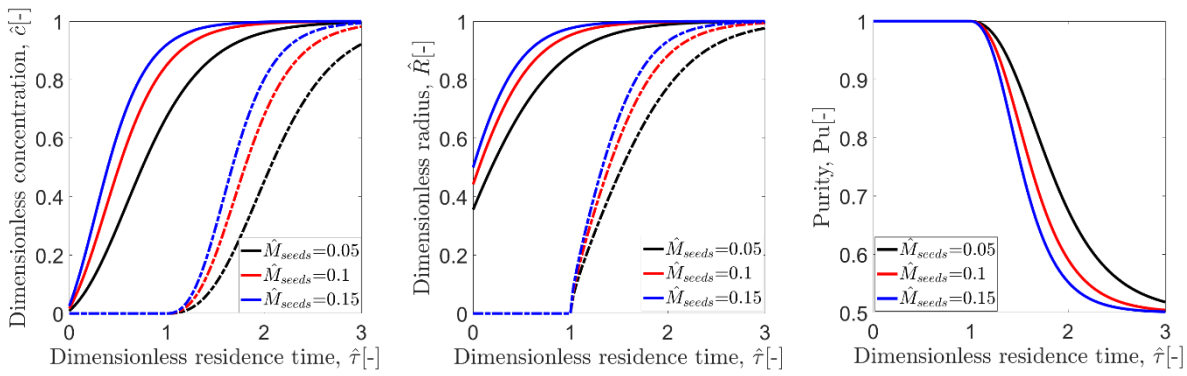


**Figure 6.13**. Dimensionless concentration ($\hat{c}$) and purity ($Pu$) is estimated using SCM as a function of Damköhler for different initial seed mass. Black curve: initial seed mass = 5% of the maximum theoretical product mass (eq. 4.34 and 4.35). Red curve: initial seed mass = 10%. Blue curve: initial seed mass = 15%. Solid curve: Preferred enantiomer. Dashed curve: Counter enantiomer.

### 6.2.2.6. Study "Back-mixing": Effect of dispersion in solid and liquid phase

The study investigates the impact of back-mixing in both the liquid and solid phases of continuous PC by incorporating dispersion effects into the model. Figures 6.14 and 6.15 present the predicted dimensionless concentrations and purities over the Damköhler number ($Da_1$), which is proportional to residence time, thereby serving as the third crucial dimensionless number in the SCM.

In Figure 6.14, four scenarios are depicted, each differing in the liquid phase Bodenstein number ($Bo_{i,L}$, eq. 4.52), which quantifies the extent of back-mixing in the liquid phase. In three of these scenarios, parallel solid phase back-mixing is represented with a constant Bodenstein number in the solid phase ($Bo_{1,S}$ = 100, eq. 4.58). The fourth scenario considers no back-mixing in either phase ($Bo_{1,S} = Bo_{i,L} = \infty$, bold line), representing the ideal PFTC scenario.

The results indicate that increased liquid phase dispersion leads to slower depletion in the liquid phase and subsequently slower growth of the target particles. This trend is analogous to findings in CRE, where, for positive reaction orders and identical residence times, conversion in a PFTR is higher than in a CSTR.

Figure 6.15 illustrates the impact of different solid phase Bodenstein numbers ($Bo_{1,S} = 10$, $100$) while keeping the liquid phase Bodenstein number constant ($Bo_{i,L} = 100$). Additionally, the PFTC scenario from figure 6.14 is repeated in figure 6.15. The observed trends differ from those seen in figure 6.14 due to different driving forces, leading to opposite directions of dispersive mass fluxes. In the liquid phase, dispersion is tied to decreasing liquid phase concentration gradients, whereas in the solid phase, it relates to particle size gradients.

This motivated us to perform two additional sets of calculations using negative solid phase Bodenstein numbers ($Bo_{1,S} = -10, -100$). These negative values illustrated similar trends as seen with positive liquid phase Bodenstein numbers, indicating faster crystallization with increasing negative solid phase Bodenstein numbers.

When both Bodenstein numbers approach infinity, predictions from the more detailed model using eq. 4.53 and eq. 4.59 closely align with those of the PFTC model (eq. 4.41 and 4.46). Notably, some inconsistencies in the counter enantiomer concentration profiles were observed in the liquid phase dispersion model, attributed to numerical challenges with very small initial particle sizes of the dormant counter enantiomers. These issues appear less critical in the solid phase dispersion scenario. In summary, the study highlights the influence of back-mixing in both liquid and solid phases on PC processes. While dispersion can slow down the crystallization rate and affect product purity, understanding and controlling these effects are crucial for optimizing PC processes, particularly when aiming for high-purity products.

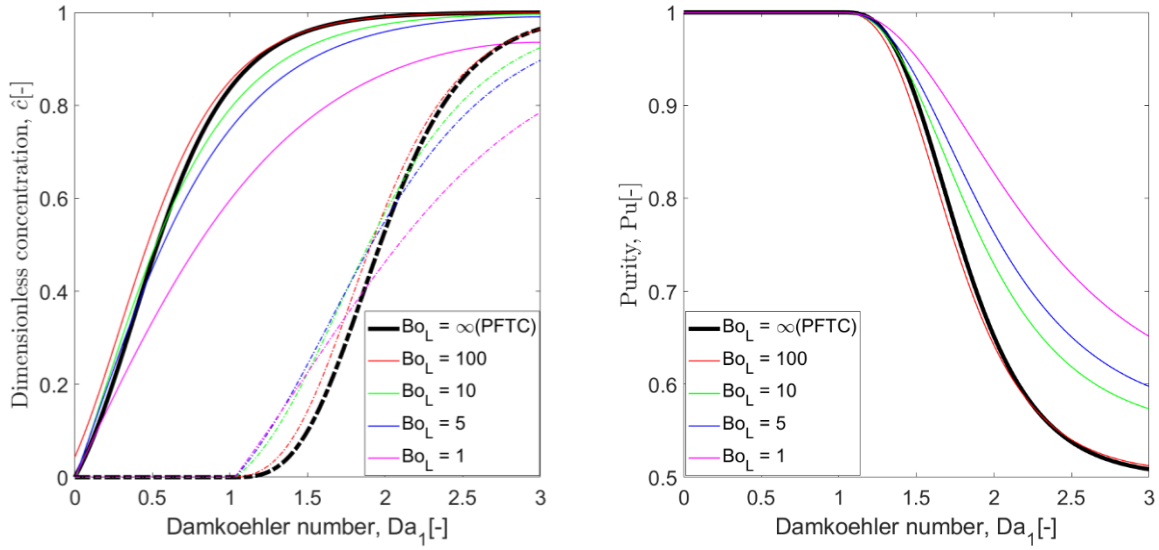


**Figure 6.14**. Predicted dimensionless concentrations ($\hat{c}$) and purities ($Pu$) as a function of Damköhler number for the case of no back-mixing (Ideal PFTC) and for the case of back mixing including five different liquid phase Bodenstein numbers keeping the solid Bodenstein number constant ($Bo_S = 100$). Black: $Bo_L = \infty$ (Ideal PFTC). Red: $Bo_L$ = 100. Green: $Bo_L$ = 10. Blue: $Bo_L$ = 5. Pink: $Bo_L$ = 1. Solid: Preferred enantiomer. Dashed: Counter enantiomer.

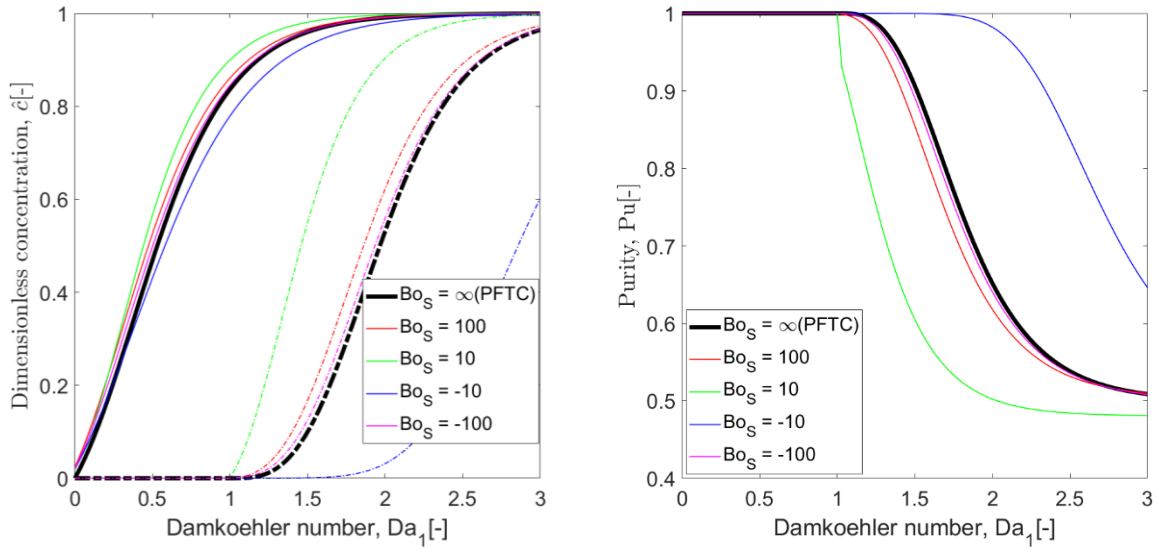


**Figure 6.15**. Predicted dimensionless concentration ($\hat{c}$) and purity ($Pu$) is estimated using SCM as a function of Damköhler number for the case of back mixing including seven different solid phase Bodenstein numbers keeping the liquid Bodenstein number constant ($Bo_L = 100$). Black: $Bo_L = \infty$ (Ideal PFTC). Red: $Bo_S$ = 100. Green: $Bo_S$ = 10. Blue: $Bo_S$ = -10. Pink: $Bo_S$ = -100. Solid: Preferred enantiomer. Dashed: Counter enantiomer.

## 6.3. SCM predictions for batch PC coupled with racemization

In this section, we examined the incorporation of an enzymatic racemization step within the Preferential Crystallization (PC) process, utilizing the Shortcut Model (SCM). The governing equations of the SCM utilized in this study are introduced in section 4.3 of chapter 4. The reference data used in the model is for the crystallization of threonine enantiomers illustrated in Part 1 of Table 5.2 in Chapter 5. The focus is primarily on the amino acid racemase enzymes and their racemization kinetics (described in Table 5.3 of chapter 5), initiating with a comparative evaluation of the efficiency between immobilized and free enzymes in this process. Subsequently, we theoretically assess various methodologies for integrating an enzymatic racemization step into the PC process (Bhandari et al. 2022).

### 6.3.1. Performance of Amino Acid Racemase (AAR)

The activity of the free AAR is influenced by inhibition effects, as illustrated In (Chaplin and Bucke 1990), these effects are quantified by the constant $K_I$ (as shown in Table 5.3). It's worth noting that at higher initial substrate concentrations, the kinetic profile of the free amino acid racemase reaches a maximum reaction rate before decreasing, as illustrated in figure 6.16.

In contrast, when the AAR is immobilized, it exhibits an apparent reduced affinity for the substrate, as evidenced by the increase in the value of $K_M$ (refer to Table 5.3), and there is no

observed effect of substrate inhibition. Both of these outcomes are likely consequences of altered concentration profiles induced by mass transport processes within the porous support, as discussed in (Mateo et al. 2007; Rodrigues et al. 2013). Remarkably, under the highest concentrations and driving forces that were experimentally investigated, the immobilized enzyme (solid red curve in fig. 6.16) even demonstrates faster reaction rates compared to the free preparation (dashed red and dotted blue curves in fig. 6.16).

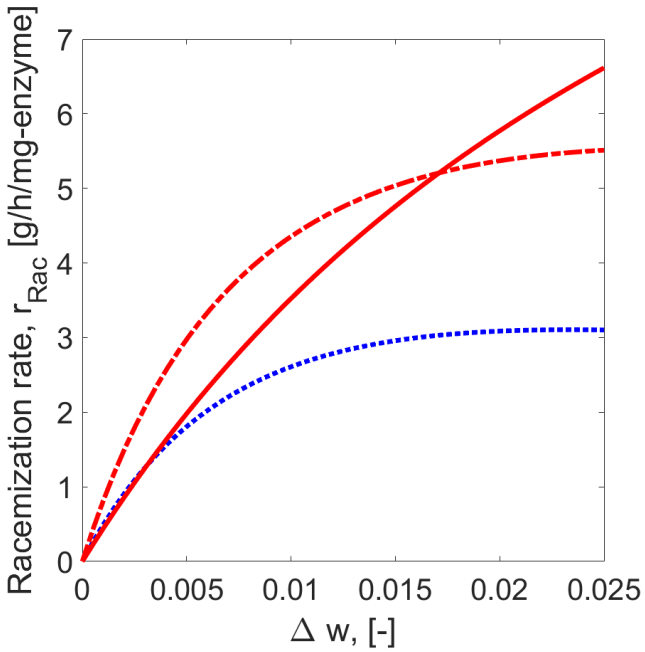


**Figure 6.16**. Racemization rates at 40°C for free (dashed red curve) and immobilized (solid red curve) amino acid racemase, and at 30°C for free racemase (blue dotted curve), plotted against enantiomeric excess.

For the studied amino acid racemase in its free form, it is observed that the presence of high concentrations of the reactant leads to a reduction in the reaction rate, (Carneiro et al. 2020). This effect is incorporated into eq. 4.70 by involving the parameter $K_I$.

## 6.3.2. Comparison between single PC and PC spatially integrated with racemization

In this section, we conducted simulations that compared coupled preferential crystallization and racemization within a same vessel using the free enzyme (depicted in figure 4.8, left) against both experimental data and theoretical outcomes of singular preferential crystallization, as reported in the case study 2 of the first section. Table 5.2 from chapter 5 and table 6.2 provide the relevant process conditions and solubility details used during the experimental and the SCM simulations for single preferential crystallization. The sets of differential eqs. 4.71 to 4.87 described in section 4.3.3 of chapter 4, which correspond to both spatially integrated and spatially segregated separation-reaction systems, were numerically

solved using MATLAB (Mathworks M 2017). Given the presence of distinct time constants associated with the problem, the solver "ODE15s" was employed due to its proficiency in handling stiff sets of equations, ensuring reliable and accurate solutions.

The optical rotation profiles, as illustrated in figure 6.17a, outline the subsequent results. The simulations, represented by the solid blue curve, match well with experimental data (blue circles) until a stop time. After this point, the crystallization of the undesired enantiomer begins, leading to a decrease in the purity of the solid product. Consequently, for a strict requirement of 100% purity, this process is feasible only until the stop time.

To enhance the process performance, we consider adding a racemization step alongside the preferential crystallization process (shown as solid red curves in fig. 6.17). This added reaction reduces the difference in concentrations of the two forms of the molecule in the liquid phase by converting one form into the other. As a result, the maximum optical rotation achieved is lower compared to the process without racemization (fig. 6.17a). Additionally, this combined process keeps the system closer to the lower boundaries of a MZW for a longer period, delaying the formation of the undesired form.

For the sake of theoretical comparison, we use the same stop time for this combined process as we did for single preferential crystallization. However, it's important to note that the inclusion of racemization affects the stop time, allowing for a longer operating period. Thus, using the same stop time represents a conservative limiting case. The performance of the integrated process benefits from this extended operating window, as discussed further below.

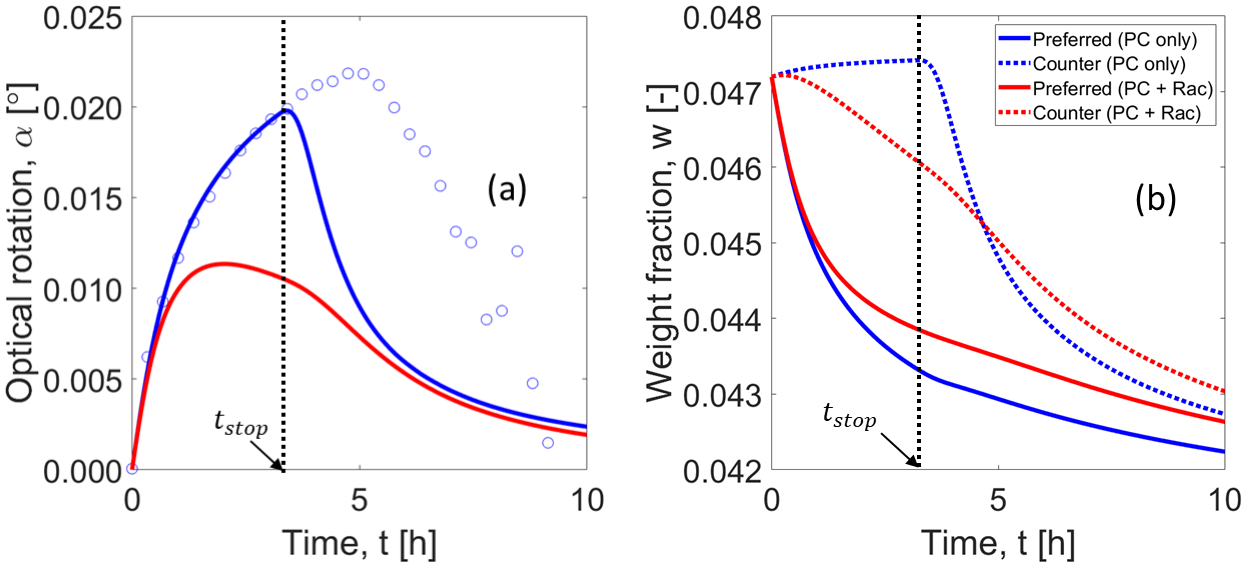


**Figure 6.17**. Comparison of experimental batch PC results and SCM simulations for DL-asparagine monohydrate in water, tracking (a) optical rotation, and (b) weight fractions of desired and opposite enantiomers in the liquid phase. Blue circles show experimental data

per conditions given in Table 5.2. Blue and red lines indicate SCM simulations without and with in situ racemization, respectively. The time $t_{stop}$ = 3.14 h marks the boundary of SCM simulation accuracy.

Figure 6.17b illustrates the predicted depletions in mass fractions of the two enantiomers in the liquid phase. The enantiomer that was initially present in the solution at higher levels crystallizes more rapidly than its counterpart, leading to steeper decline in its concentration. In the coupled process with racemization (depicted by the solid red curves), the racemization reaction initiates a reduction in the concentration of the counter enantiomer even before the stop time, as it is being converted into the desired enantiomer. This effect does not occur in the single batch preferential crystallization (represented by the solid blue curves). Moreover, the overall concentration of the desired enantiomer remains higher in the process involving racemization compared to the process without it. These outcomes suggest that racemization does not completely hinder the increase in enantiomeric excess during crystallization. Nonetheless, there is still a noticeable advantage in utilizing this reaction. It enables the maintenance of elevated levels of supersaturation, which is beneficial to crystal growth and, consequently, enhances the productivity of the process, as outlined in eq. 3.40.

## 6.3.3. Evaluation of variants of spatially segregated process

We conducted simulations using the SCM to study a spatially segregated process. Specifically, we explored two different designs for the external racemization reactor: one with a single stirred tank reactor and another with a cascade of stirred tank reactors, as illustrated in fig. 4.9b and 4.9c, respectively.

### 6.3.3.1. Influence of enzyme preparation

The combination of PC with a single stirred tank racemization reactor was simulated, as elaborated in section 4.3.3.1 of chapter 4. We selected the operating parameters for these simulations based on the scale of our laboratory setup, and these conditions are outlined in Table 6.6.

**Table 6.6**. Operating parameters for the racemization reactor in the spatially segregated process.

| Parameter | Symbols | Value | Unit |
|---|---|---|---|
| Flow rate | $\dot{V}$ | 3.5 | $\mathrm{ml/min}$ |
| Reactor volume | $V_R$ | 2 | $\mathrm{ml}$ |

Figure 6.18 compares the model's predictions for enzymatic reactions occurring in a homogenous (shown in fig. 4.9a) versus those happening in a heterogeneous medium (fig. 4.9b). The model's predictions for optical rotation when using free soluble enzymes and

immobilized enzymes are indicated by dashed and solid curves, respectively. The same dosage of enzyme, represented by $D_C$, was used in both setups, as specified in Table 5.3. When using the immobilized enzyme, the peak in optical rotation was much lower. This suggests faster racemization of the counter enantiomer, preventing large concentration differences between the two enantiomer forms. It's worth noting that the rate of enzyme-catalyzed reactions can change when the enzyme is immobilized. For AAR enzymes we studied, immobilization had effects on mass transfer but allowed it to react faster at high concentrations of the reactant, as shown in fig. 5.1. Unlike the free amino acid racemase, the immobilized preparations did not show inhibition effects under the high substrate concentration. Thus, for this particular setup, the free enzyme led to a slower racemization compared to when the enzyme was immobilized, as evident in fig. 6.18.

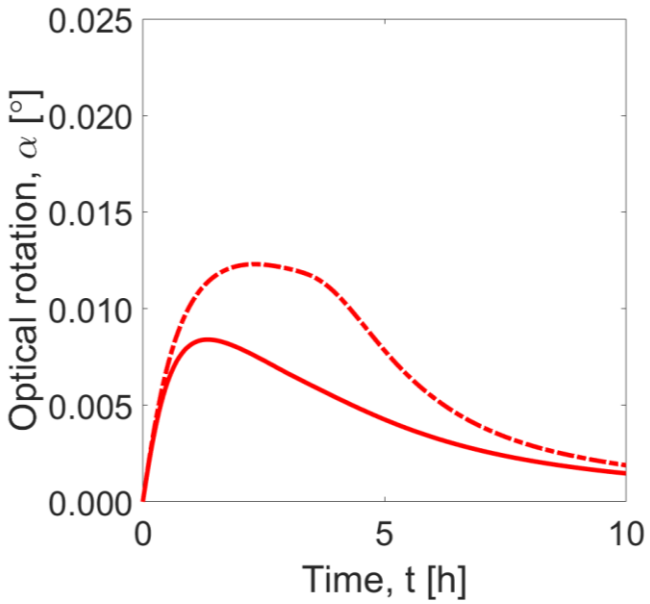


**Figure 6.18**. Depiction of simulated optical rotation patterns in a batch crystallization system linked to an enzymatic reactor with stirring, employing free (represented by a dashed line) and immobilized (shown with a solid line) enzyme.

Therefore, immobilized amino acid racemase (eq. 4.70, Table 5.3) is taken into consideration in the subsequent process design calculations due to its improved performance.

### 6.3.3.2. Influence of size of enzymatic reactor and flow rate

We conducted a study to assess the impact of different mean residence times of the liquid phase on the productivity of the process depicted in fig. 4.9b. We considered a range of reactor volumes $V_R$ from 0 to 5 ml and flow rates $\dot{V}$ from 0 to 5 ml/min, which are typical conditions for laboratory-scale investigations. The residence time ($\tau$) was calculated using eq. 6.3:

$$\tau = \frac{V_R}{\dot{V}} \qquad 6.3$$

The effect of these parameters on productivity is illustrated in fig. 6.19. When there is no flow between the units ($\dot{V} = 0$), which represents PC without racemization, the productivity remains constant at 0.96 g/h/l, as previously reported in section 6.1.2.3.

As the flow rate increases, there is more mother liquor and, consequently, more reactant available for racemization at any given time. This leads to an increase in the reaction rate and, consequently, higher productivities. However, there is a limit to this improvement. For a fixed residence time, increasing the flow rate doesn't significantly enhance productivity. In the extreme case when the flow rate becomes very high (i.e., $\dot{V} \to \infty$) the process's behaviour transitions from “spatially segregated” to “spatially integrated”.

The plot in fig. 6.19 highlight that increasing the residence time of the liquid in the reactor results in higher productivities. To achieve a longer residence time while keeping the volumetric flow rate constant, one can use a larger reactor volume. However, it's important to note that larger reactors can only enhance the resolution process up to a certain point. Increasing the reactor volume also means using a larger amount of enzyme, which accelerates the conversion of the counter enantiomer. Consequently, the productivity profiles reach limiting values at a constant flow rate.

In the case of immobilized enzymes, the relationship between reactor volume and catalyst dosage is influenced by the characteristics of the packed reactor. In our study, the amino acid racemase was immobilized at a load of 35 mg-enzyme/g-support, and a 2.1 ml column reactor was packed with 0.9 g-support/ml (as detailed in Table 5.3 of chapter 5). It's worth mentioning that lower amounts of immobilized support per unit volume are acceptable when the enzyme carrier is dispersed in the liquid phase. However, using higher amounts of support can lead to compression of the packing, which may compromise enzymatic activity.

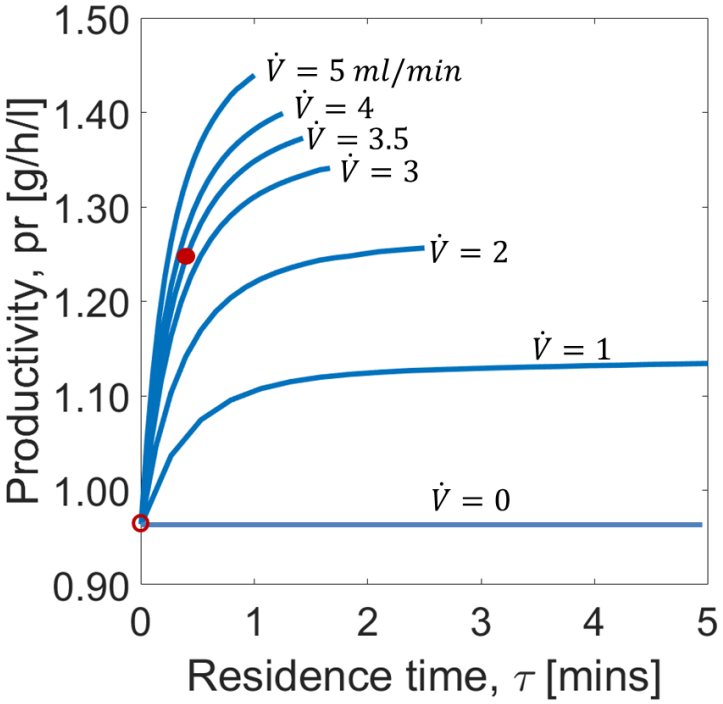


**Figure 6.19**. Influence of residence time (from eq. 6.3) on the productivity (from eq. 3.40) of preferential crystallization (PC) combined with heterogeneous enzymatic racemization in a single stirred tank reactor. The red dot indicates productivity at a flow rate $\dot{V}$= 3.5 ml/min and reactor volume $V_R$ = 2 ml (refer to Table 6.6). The red circle denotes productivity outcomes for PC without the racemization process (refer to section 6.1.2.3).

#### 6.3.3.3. Racemization in a cascade of tank reactors

In this setup, we conducted SCM simulations using a series of stirred tank reactors (STRs) connected in a cascade configuration with the crystallizer, as illustrated in fig. 4.9c. All the reactors in this setup have the same volume and residence time, and the total volume equals that of a single STR as discussed previously (refer to Table 6.6).

To assess how the number of reactors in the cascade affects the process performance, we estimated productivity for a range of values of '$n$'. The outcomes are depicted in fig. 6.20 As the reaction progresses through each reactor in the cascade, racemization decreases the concentration difference between the enantiomers. Consequently, the driving force available for the $j^{th}$ reactor is lower than that for the subsequent ones. Hence, the productivity profile eventually reaches a plateau at a relatively high number of reactors. In this range, any further increase in productivity may not justify the additional cost of incorporating more reactors. Although a detailed investigation to determine the optimal value of '$n$' for the spatially segregated process was not the primary goal here, we selected a reasonable value of '$n$ = 3' based on the plot's characteristics. Maintaining a constant total reactor volume, transitioning from a single reactor to a cascade of three equally sized reactors results in an almost 3% gain in productivity.

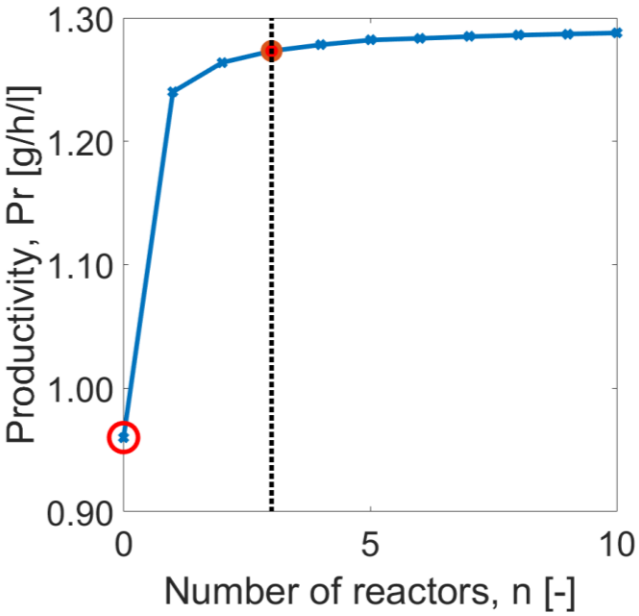


**Figure 6.20**. Effect of the quantity '$n$' of stirred tank reactors (STRs) on the productivity (as per eq 3.40) of a crystallizer integrated with a series of STRs. A red dot shows the productivity when '$n$' equals 3, which is utilized for subsequent computations. A red circle represents the productivity for PC conducted without racemization (refer to section 6.1.2.3).

#### 6.3.3.4. Influence of stop time on productivity

Determining the right time to stop a batch is very crucial to maintain the product purity. Previously, we defined it in the shortcut model as the time until which the crystallization of the counter enantiomer is insignificant. This parameter has traditionally been estimated based on stringent chiral purity requirements in the case of single PC. However, to improve productivity, it's essential to investigate the optimal stopping point for the process. Altering the stop time directly influences the yield of the process, making it vital to assess the overall yield.

In coupling PC with racemization, it's clear that the applicable stop time can be extended. In this section, we study the effects of various stop times on both productivity and yield. As defined earlier, for a constant volume, productivity (as per eq. 3.40) is directly related to the mass of the product harvested and inversely related to the stop time. It increases as more product mass is collected, reaches a maximum, and then declines with an increase in the stop time. Yield (as per eq. 3.41) represents the ratio of the total product mass to the maximum theoretical product mass achievable. It rises with increased product mass collected and becomes flat at equilibrium.

The red curve in fig. 6.21 illustrates the process without racemization. At the reference stop time determined with the requirement for 100% purity based on experimental data (i.e.,

$t_{stop}^{ref,exp}$ = 3.14 hours), the estimated productivity was 0.96 g/h/l, as previously mentioned. However, simulations indicated that the maximum productivity occurs at an earlier process time, $t_{stop,PC}^{opt}$ = 1 hour. If the process is halted at this point, an improvement of approximately 30% in productivity can be achieved (as shown in fig. 6.21a). Nevertheless, the yield decreases by roughly 35% due to stopping the process earlier (fig. 6.21b).

The blue curve in fig. 6.21 represents the simulation of a spatially segregated process with 3 stirred tank reactors (as shown in schematic of fig. 4.9c). It also demonstrates an optimal productivity value and corresponding yield value before the stop time determined for PC without racemization. By running the coupled process until the earlier time at $t_{stop,(PC+rac)}^{opt}$ = 1.4 hours, productivity can be improved by approximately 10%. However, this approach reduces the overall yield by about 30%. This result is intriguing because the racemization step prevents the crystallization of the counter enantiomer and makes the process more robust for a longer period.

In summary, compared to single PC without racemization, a shorter stop time and the integration of racemization can improve productivity by 45% while slightly reducing overall yield by 10%.

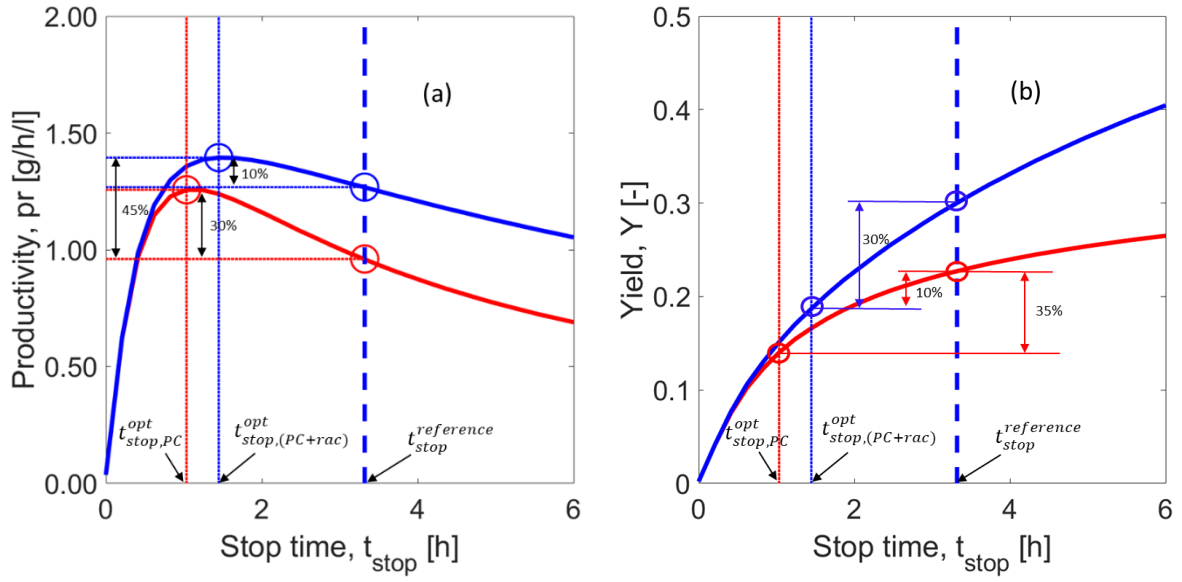


**Figure 6.21**. The figure assesses productivity and yield, and examines how the chosen stop time affects these KPIs. The red curve shows the productivity of a single batch preferential crystallization (PC) without any racemization process involved. The blue curve represents a spatially divided process that includes racemization within a series of three stirred tank reactors. The dashed line indicates the stop time based on experimental data from Table 5.2, noted as $t_{stop}^{ref,exp}$ = 3.14 hours. By implementing the process at the optimal stop times of $t_{stop,PC}^{opt}$ = 1 hour for single PC and $t_{stop,(PC+rac)}^{opt}$ = 1.4 hours for the combined process,

productivity is seen to rise by approximately 30% and 10%, while yield decreases by 35% and 30% for the single PC and spatially segregated coupling, respectively. When compared to the reference case, there's an overall increase in productivity by 45% and a decrease in yield by 10%. The conditions for these simulations are detailed in Tables 5.2 and 6.6

## 6.4. Summarizing the three applications of the SCM

Preferential Crystallization is a simple and effective kinetic driven technique for separating enantiomers, commonly used in industry for the production of optically active pure substance. In recent years, the application of mathematical models became increasingly important in industrial settings to design corresponding crystallization processes. This shift is partly due to the availability of commercial software (Process System Enterprise 2018) and a better understanding of the underlying mathematics. However, there are still challenge in measuring and describing the kinetic and thermodynamics information for a specific substance. The incorporation of this knowledge is crucial for applying the mathematical models to real-world problems. There are various methods to measure this, each with its own strengths and weaknesses, but they are often tailored to specific scenarios. The difficult parametrization and subsequent application of PBM's which describe in detail the particle size distribution of the solid phase is often not needed for early-stage process evaluations. Therefore, in initial process design phases, it is attractive to use simplified or "shortcut" models (SCM). These models reduce the complexity and number of experiments required to parametrize them and they offer quicker estimation of important Key Performance Indicators (KPIs).

In the first part of this chapter, we have utilized the SCM introduced in section 4.1 for rapidly evaluating the efficiency of batch isothermal preferential crystallization processes. We outlined a possible method for estimating the model parameters using a limited amount of experimental data. We presented the model's effectiveness through case studies devoted to resolve enantiomers of two chiral compounds: D-/L-Threonine and D-/L-Asparagine monohydrate. For the first compound we exploited theoretically predicated simulated transients using a population balance model. For the second case study we used available experimental data. Both cases studies highlight the SCM's capability in predicting the productivity of different processes based on exploiting preferential crystallization. The objective of this first part was the development and validation of SCM (Carneiro et al. 2019).

In a second part, we used the SCM equations derived in section 4.2 further to describe the continuous steady-state regime of PC performed in a tubular crystallizer. In this part we applied principles and analogies of chemical reaction engineering (CRE). The extension transferred the model from batch to continuous operations using dimensionless numbers, which facilitate understanding and broader applicability. We employed two prominent dimensionless numbers, namely the Damköhler number (Damköhler 1936; Inger 2001;

Rehage and Kind 2021) and the Bodenstein number (Westerterp et al. 1984). In our study of a tubular crystallizer two scenarios have been investigated: an idealized model without back-mixing (ideal plug flow), and a more realistic model considering back-mixing in both phases, which closely aligns with practical PC applications (Bhandari, Lorenz, and Seidel-Morgenstern 2024).

In the last part, we evaluated the extended SCM for batch PC complemented by different strategies of integrating an enzymatic racemization step. The underlying equations were derived in section 4.3. This analysis focussed on separating the enantiomers of an amino acid based on independently determined available racemization kinetics. This included comparing the efficacies of immobilized and free enzymes. Our findings suggest that for the specific case studied the immobilized enzymes are more effective at higher substrate concentrations. Furthermore, we highlighted the SCM's adaptability in incorporating a cascade of tank crystallizers, which offer a significant advancement compared to conventional single-tank operation. We emphasized the importance of determining the optimal stop time, which marks the limit of applicability of the SCM, to enhance the productivity of the PC process (Bhandari et al. 2022).

## 6.5. Workflow to apply SCM in designing a PC process

As outlined above, rationally designing a preferential crystallization process involves navigating through a series of complex and interrelated decisions. The use of a workflow in this context helps in methodically dissecting this complexity into several sequential steps. This approach provides a structured way for experimentation and decision-making. Such a strategy is in particular vital in developing preferential crystallization, where the operating conditions significantly influence the outcome.

We suggest applying the workflow illustrated in fig. 6.22, which summarizes important steps up to possible pilot plant PC operation. A preliminary version was described in (Bhandari et al. 2024).

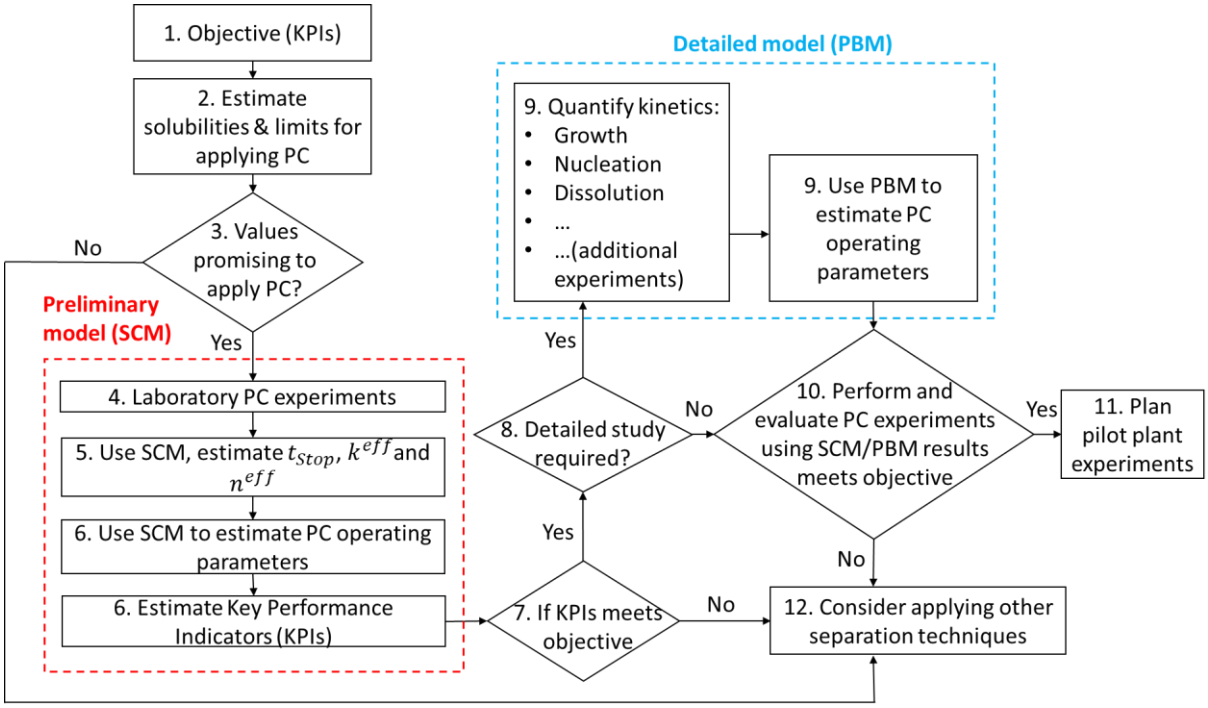


**Figure 6.22**. Iterative framework for optimizing Preferential Crystallization (PC) processes (Bhandari et al. 2024)

Here's a step-by-step explanation of the flowchart shown in fig. 6.22:

1. **Objective**: Defining the objective(s) at the outset is essential in PC because the goals can vary widely based on the specific chiral compound considered, from achieving a specific enantiomeric excess to maximizing yield, productivity or purity.

2. **Estimate solubility & limits for applying PC**: Having quantitative understanding of solubilities and the metastable zone widths (MZW) is critical in PC. Solubility data provide information that are crucial in critical decision making such as the selection of solvents and suitable temperature conditions. The MZW have an influence on the supersaturation levels, which directly affect nucleation rates and the quality and purity of the resulting crystals. Details can be found in chapter 2.

3. **Values of step 2 promising to apply PC:** After estimating the solubility and metastable zone width (MZW) in step 2, it is crucial to assess whether these values are suitable to proceed with the preferential crystallization process. If the solubility and MZW values are sufficiently high, the process can continue to the next steps. However, if the values do not allow an economically attractive separation, the PC process is not suitable to solve the given problem. In such a case, it is advisable to move directly to step 12 and to consider alternative separation techniques. This step serves as an early decision point to avoid investing resources in a process that may not be viable.

4. **Design and perform preliminary experiments**: This step involves designing and performing nucleation-onset and preferential crystallization (PC) experiments to estimate the Shortcut Model (SCM) parameters for the system under investigation. To ensure accurate estimation, at least three experiments should be conducted under isothermal conditions at a fixed supersaturation level. A potential set of experiments is described and applied in chapter 5.

5. **Estimate $t_{stop}$, $k^{eff}$, and $n^{eff}$**: The empirical equations eq. 4.18 and 4.19 are provided in section 4.1.4.3 of chapter 4 as a function of initial supersaturation ($S^0$). Detailed explanation on estimating and correlating each of these SCM parameters is given in section 6.1.1.1.

6. **Use the SCM**: With the parametrized simple SCM, the Key Performance Indicators (KPIs) can be calculated for various operating regimes and conditions (see section 6.1.1.3).

7. **Process performance (KPI) check**: This step is crucial to decide if the performance of the PC process using KPI estimated by SCM is meeting our initially set objective(s) or not. In case of poor performance, we should give up PC and consider applying another technique to separate the given enantiomers (step 12). In case of sufficient performance, we go to the step 8.

8. **Decision regarding more detailed study:** A decision point to assess if more in-depth investigations are still necessary before performing detailed laboratory PC experiments. If the answer is “Yes” then we go the next step 9. If the answer is “no” we go the step 10.

9. **Detailed study using PBM**: Use PBM to perform the detailed study of the PC process. This step involves performing experiments about various aspects of the PC process to estimate nucleation rates and to reevaluate crystal growth rates depending on the various specific mechanisms affecting the process. Then use the results of these experiments to estimate the kinetic parameters of PBM.

10. **Perform and evaluate PC experiments using the SCM/PBM results**: Based on the approach chosen in step 8, we perform detailed laboratory PC experiments based on either SCM (step 6) or PBM (step 9) results. We then assess these results to see if they align with our objective. If the objective is still not achieved, we consider applying alternative separation methods (step 12). If the results are satisfactory, we move forward carrying out final pilot scale PC experiments as a last step prior to possible production scale (step 11).

11. **Plan pilot plant experiments**: Successful laboratory experiments are scaled up to pilot plant experiments. If these are successful, the next step is industrial and commercial application.

12. **Consider applying other separation techniques**: If the objectives are not reached, alternative separation methods should be (re)considered such as enantioselective chromatography or asymmetric synthesis.

This workflow outlines a systematic approach for developing preferential crystallization (PC) processes, integrating both experimental and modelling techniques to evaluate their effectiveness and potential to meet specific objectives. The Shortcut Model (SCM) developed in this study is incorporated into the workflow as a valuable tool for early-stage evaluation of performance parameters. This allows for informed decision-making on whether to advance to the more detailed, yet complex and challenging Population Balance Models (PBM).

# 7. Conclusion and outlook

This dissertation describes the development and application of a Shortcut Model (SCM) for Preferential Crystallization (PC) of conglomerate forming chiral compounds, as a technique pivotal for the provision of optically active substances. The thesis supports a current shift towards broader application of mathematical modelling for crystallization process design in industrial settings (particularly population balance equations, PBEs). This trend is due to advancements in commercial software and a deeper theoretical understanding within the crystallization community. Despite these advancements, there are severe hurdles in determining in particular the various kinetic parameters relevant to characterize the crystallization behaviour of a specific compound. This limitation is especially pronounced in designing more advanced process regimes, such as for the conversion of batch processes to continuous ones or the integration of racemization reactions with PC.

Addressing these challenges, the thesis proposes the SCM which aims at reducing complexity and experimental requirements, thereby offering a more efficient and straightforward preliminary rough analysis of Key Performance Indicators (KPIs). The SCM is based on overall mass balances and metastable solubilities derived from Ternary Phase Diagrams (TPD). It allows for rapidly evaluating the efficiency of isothermal batch PC processes. Besides elucidating the key assumptions of the SCM also methods for parameter estimation using minimal experimental data are suggested.

After discussing batch-wise carried out PC, the thesis expanded the SCM to continuous steady-state PC, employing principles and analogies borrowed from chemical reaction engineering (CRE). By utilizing dimensionless numbers, such as the Damköhler and Bodenstein numbers, the thesis refines the SCM for qualitative analysis of continuous PC processes in a tubular crystallizer. Furthermore, the SCM was finally extended to integrate an enzymatic racemization step into the batch PC. This allows eliminating losses due to unwanted enantiomers and increases process yields. The concept was studied employing various strategies of applying enzyme (racemases).

The case studies presented in this thesis were instrumental in demonstrating the effectiveness of the SCM for isothermal PC of conglomerate forming systems. These cases utilize the SCM across various PC variants, including batch and continuous processes, along with integration of racemization processes. The results presented offer crucial insights into how different operational and thermodynamic parameters influence separation efficiency. This approach deepens the general understanding the PC processes.

While the SCM provides valuable insights, the predictions provided are of course specific just for the studied examples. Due to the diversity of nucleation and growth rates, as well as enzyme-specific racemization rates, generalizing the results obtained remains challenging.

Nevertheless, the SCM's conceptual approach is seen as very versatile and adaptable to various crystallization and racemization process configurations, for applying both batch and continuous operation principles.

Finally, to clarify the role of the SCM in a broader framework of optimizing PC a multi-step workflow was developed.

In conclusion, this research work contributes to fill a gap in initial process design of PC by introducing a shortcut model. The model outlined and expanded in this thesis has proven to be a powerful tool for designing, optimizing, and potentially controlling PC processes. Its adaptability to different scenarios and configurations, along with its ability for rapid and efficient estimation of productivities and yields makes it a valuable asset in the field of industrial crystallization and process design.

**Outlook**

The SCM has potential for broader application across a range of related complex crystallization-based separation processes, particularly where detailed models such as the PBM face challenges due to the extensive experimental work required to estimate kinetics accurately.

The SCM could be further adapted to include, for instance, isolating the enantiomers for racemic compound forming systems, which represent a large fraction of the chiral molecules. The expansion of SCM to non-isothermal processes would also be beneficial, allowing for a better understanding and exploitation of temperature effects in crystallization. Additionally, applying SCM to antisolvent crystallization could offer new insights and improvements (Mack et al. 2022). It is imperative to note that incorporating further complexities into the SCM to describe such varied processes requires additional preliminary experimental information to apply the model appropriately.

# Appendix

## A1. Discretization to solve non-linear algebraic equation

In chapter 4, eqs. 4.53 and 4.59 combined with the Dankwert's boundary conditions are a set of non-linear algebraic equations. To solve it, we discretized the length coordinate into $n$ equal segments as shown in figure A1.

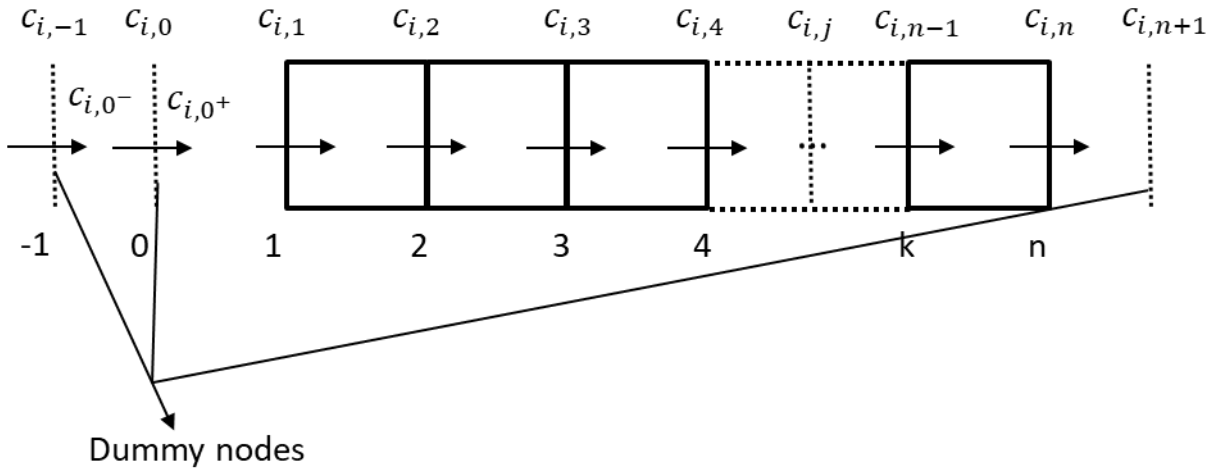


**Figure A1**: Discretization of the length coordinate into $n$ equal segments

Using second order central difference approximation in eq. 4.53 gives:

$$\frac{\hat{c}_{i,2}-\hat{c}_{i,0}}{2\Delta\hat{z}}=\frac{1}{Bo_{i,L}}\left(\frac{\hat{c}_{i,IN}-2\hat{c}_{i,1}+\hat{c}_{i,2}}{\Delta\hat{z}^2}\right)+Da\hat{R}_{i,1}^2(1-\hat{c}_{i,1})^{n^{eff}} \qquad \text{A1.1}$$

Substituting boundary condition from eq 4.62:

$$\frac{\hat{c}_{i,2}-\left(\hat{c}_{i,IN}+\frac{1}{Bo_{i,L}}\left(\frac{d\hat{c}_i}{d\hat{z}}\right)_{\hat{z}=0}\right)}{2\Delta\hat{z}} = \frac{1}{Bo_{i,L}}\left(\frac{\left(\hat{c}_{i,IN}+\frac{1}{Bo_{i,L}}\left(\frac{d\hat{c}_i}{d\hat{z}}\right)_{\hat{z}=0}\right)-2\hat{c}_{i,1}+\hat{c}_{i,2}}{\Delta\hat{z}^2}\right) + Da\hat{R}_{i,1}^2(1-\hat{c}_{i,1})^{n^{eff}} \qquad \text{A1.2}$$

By second order approximation (central difference method):

$$\frac{d\hat{c}_i}{d\hat{z}}=\frac{\hat{c}_{i,1}-\hat{c}_{i,-1}}{2\Delta\hat{z}} \qquad \text{A1.3}$$

and $\hat{c}_{i,-1}$ is a dummy node with values equal to $\hat{c}_{i,IN}$

$$\frac{\hat{c}_{i,2} - \left(\hat{c}_{i,0} + \frac{1}{Bo_{i,L}}\left(\frac{\hat{c}_{i,1} - \hat{c}_{i,IN}}{2\Delta\hat{z}}\right)\right)}{2\Delta\hat{z}} = \frac{1}{Bo_{i,L}}\left(\frac{\left(\hat{c}_{i,0} + \frac{1}{Bo_{i,L}}\left(\frac{\hat{c}_{i,1} - \hat{c}_{i,IN}}{2\Delta\hat{z}}\right)\right) - 2\hat{c}_{i,1} + \hat{c}_{i,2}}{\Delta\hat{z}^2}\right) + Da\hat{R}_{i,1}^2(1 - \hat{c}_{i,1})^{n^{eff}} \quad \text{A1.4}$$

For $n = 1$

$$\hat{c}_{i,1}\left(\frac{2}{\Delta\hat{z}^2 Bo_{i,L}} - \frac{1}{2Bo_{i,L}^2\Delta\hat{z}^3} - \frac{1}{4Bo_{i,L}\Delta\hat{z}^2}\right) + \hat{c}_{i,2}\left(\frac{1}{2\Delta\hat{z}} - \frac{1}{\Delta\hat{z}^2 Bo_{i,L}}\right) + \hat{c}_{i,IN}\left(\frac{-1}{2\Delta\hat{z}} - \frac{1}{\Delta\hat{z}^2 Bo_{i,L}} + \frac{1}{2Bo_{i,L}^2\Delta\hat{z}^3} + \frac{1}{4Bo_{i,L}\Delta\hat{z}^2}\right) - Da\hat{R}_{i,1}^2(1 - \hat{c}_{i,1})^{n^{eff}} = 0 \quad \text{A1.5}$$

For $n = j$

$$\hat{c}_{i,j-1}\left(\frac{-1}{2\Delta\hat{z}} - \frac{1}{\Delta\hat{z}^2 Bo_{i,L}}\right) + \hat{c}_{i,j}\left(\frac{2}{\Delta\hat{z}^2 Bo_{i,L}}\right) + \hat{c}_{i,j+1}\left(\frac{1}{2\Delta\hat{z}} - \frac{1}{\Delta\hat{z}^2 Bo_{i,L}}\right) - Da\hat{R}_{i,j}^2(1 - \hat{c}_{i,j})^{n^{eff}} = 0 \quad \text{A1.6}$$

For $n = n$, from boundary condition in eq 4.62

$$\hat{c}_{i,n+1} = \hat{c}_{i,n-1}$$

$$-\frac{1}{Bo_{i,L}}\left(\frac{2\hat{c}_{i,n-1} - 2\hat{c}_{i,n}}{\Delta\hat{z}^2}\right) - Da\hat{R}_{i,n}^2(1 - \hat{c}_{i,n})^{n^{eff}} = 0 \quad \text{A1.7}$$

For solid phase, from eq. 4.59:

$$\frac{d\hat{R}_i}{d\hat{z}} = K_S Da\left(\frac{Bo_{i,S}\hat{R}_i}{Bo_{i,S}\hat{R}_i - 2}\right)(1 - \hat{c}_i(z))^{n^{eff}} \quad \text{A1.8}$$

Using backward finite difference approximation:

$$\frac{\hat{R}_{i,1} - \hat{R}_{i,0}}{\Delta\hat{z}} = K_S Da\left(\frac{Bo_{i,S}\hat{R}_i}{Bo_{i,S}\hat{R}_i - 2}\right)(1 - \hat{c}_{i,n})^{n^{eff}} \quad \text{A1.9}$$

Substituting boundary condition from eq 4.65:

For $n = 1$

$$\frac{\widehat{R}_{i,1} - \left(\widehat{R}_{i,IN}^3 + \frac{6\widehat{R}_{i,0}}{Bo_{i,S}}\left(\frac{d\widehat{R}_i}{d\hat{z}}\right)_{\hat{z}=0}\right)^{1/3}}{\Delta\hat{z}} = K_S Da\left(\frac{Bo_{i,S}\widehat{R}_i}{Bo_{i,S}\widehat{R}_i - 2}\right)(1-\hat{c}_{i,n})^{n^{eff}} \quad \text{A1.10}$$

For $n = j$

$$\frac{\widehat{R}_{i,j} - \widehat{R}_{i,j-1}}{\Delta\hat{z}} = K_S Da\left(\frac{Bo_{i,S}\widehat{R}_i}{Bo_{i,S}\widehat{R}_i - 2}\right)(1-\hat{c}_{i,n})^{n^{eff}} \quad \text{A1.11}$$

For $n = n$

$$\frac{1 - \widehat{R}_{i,n-1}}{\Delta\hat{z}} = K_S Da\left(\frac{Bo_{i,S}\widehat{R}_i}{Bo_{i,S}\widehat{R}_i - 2}\right)(1-\hat{c}_{i,n})^{n^{eff}} \quad \text{A1.12}$$

# Nomenclature

| **Abbreviations** | |
|---|---|
| AAR | Amino Acid Racemace |
| BCF | Burton Cabrera Frank |
| BPD | Binary Phase Diagram |
| CRE | Chemical Reaction Engineering |
| CSP | Chiral Stationary Phase |
| CNT | Classical Nucleation Theory |
| CSTR | Continuous Stirred Tank Reactors |
| KPI | Key Performance Indicators |
| MSMPR | Mixed Suspension Mixed Product Removal |
| MZW | Metastable Zone Width |
| MZ | Metastable Zone |
| MOM | Method of Moments |
| MOC | Method of Characteristics |
| ODE | Ordinary Differential Equation |
| PC | Preferential Crystallization |
| PBM | Population Balance Model |
| PBE | Population Balance Equation |
| PFTC | Plug Flow Tubular Crystallizer |
| PFTR | Plug Flow Tubular Reactor |
| SCM | Shortcut Model |
| SOAT | Second Order Asymmetric Transformation |
| SLE | Solid Liquid Equilibrium |
| STR | Stirred Tank Reactors |
| TPD | Ternary Phase Diagrams |
| | |
| **Latin letters** | |
| $A_C$ | cross-sectional area of a tubular crystallizer, [$cm^2$] |
| $A_{prim}$ | PBM coefficient of heterogeneous contribution (prim. nucleation), [$m^{-2n_{\mu 2}}$] |
| $a_k$ | parameter of correlation of $k^{eff}(S^0)$, [g $h^{-1}$ $cm^{-2}$] |
| $a_{k,T}$ | parameter of correlation of $k^{eff}(S^0, T)$, [g $h^{-1}$ $cm^{-2}$] |

| | |
|---|---|
| $a_t$ | parameter of correlation of $t_{stop}$, [h] |
| $Bo_L$ | Bodenstein number for the liquid phase, [-] |
| $Bo_S$ | Bodenstein number for the solid phase, [-] |
| $B$ | PBM nucleation rate, [# $h^{-1}$] |
| $b_k$ | parameter of correlation of $k^{eff}(S^0)$, [-] |
| $b_{k,T}$ | parameter of correlation of $k^{eff}(S^0,T)$, [-] |
| $b_{sec}$ | PBM power law exponent (sec. nucleation), [-] |
| $b_t$ | parameter of correlation of $t_{stop}$, [-] |
| $c_k$ | parameter of correlation of $k^{eff}(S^0)$, [-] |
| $c_{k,T}$ | parameter of correlation of $k^{eff}(S^0,T)$, [-] |
| $c_i$ | concentration of a component $i$, [g $cm^{-3}$] |
| $c_{i,sat}$ | saturation concentration of a component $i$, [g $cm^{-3}$] |
| $c_{i,in}$ | initial concentration of a component $i$, [g $cm^{-3}$] |
| $\hat{c}_i$ | dimensionless concentration of a component $i$, [-] |
| $\hat{c}_{i,in}$ | initial dimensionless concentration of a component $i$, [-] |
| $D$ | dissolution rate in PBM, [cm $h^{-1}$] |
| $D_{ax,L}$ | dispersion in liquid phase, [$cm^2$ $h^{-1}$] |
| $D_{ax,S}$ | dispersion in solid phase, [$cm^2$ $h^{-1}$] |
| $Da_i$ | Damköhler number of a component $i$, [-] |
| $D_C$ | Dosage or concentration of catalyst, [mg-enzyme $L^{-1}$] |
| $ee_S$ | enantiomeric excess of solid phase, [-] |
| $ee_L$ | enantiomeric excess of liquid phase, [-] |
| $ee$ | enantiomeric excess, [-] |
| $E_{Ag}$ | PBM activation energy of growth kinetics, [J $mol^{-1}$] |
| $E^{eff}$ | effective activation energy, [kJ $mol^{-1}$] |
| $F_2$ | counter enantiomer contamination, activates at $t = t_{stop}$, [-] |
| $f$ | number density function, [# $cm^{-1}$] |
| $g$ | PBM power law exponent of growth kinetics, [-] |
| $G_i^{eff}$ | crystallization kinetic rate law, [g $h^{-1}$ $cm^{-2}$] |
| $G$ | PBM growth rate, [cm $h^{-1}$] |
| $\overline{GB}^{eff}$ | effective overall mass transfer rate, [g $h^{-1}$] |
| $k_{bprim1}$ | PBM pre-exponential coefficient (prim. nucleation), [$h^{-1}$ $K^{-1}$ $m^7$ $kg^{-7/3}$] |

| | |
|---|---|
| $k_{bprim2}$ | PBM exponential coefficient (prim. nucleation), [-] |
| $k_{bsec,0}$ | PBM pre-exponential coefficient (sec. nucleation), [$h^{-1}$ $m^{-3n_{\mu 3}}$] |
| $k^{eff}$ | effective crystallization rate constant, parameter of SCM, [g $h^{-1}$ $cm^{-2}$] |
| $k^{char}$ | characteristic crystallization rate constant, parameter of SCM, [$h^{-1}$ $cm^{-2}$] |
| $k_{\alpha}$ | calibration parameter of polarimeter, [g $g^{-1}$ $deg^{-1}$] |
| $k_0^{eff}$ | parameter of correlation of $k^{eff}(S^0, T)$, [g $h^{-1}$ $cm^{-2}$] |
| $k_{g,0}$ | PBM pre-exponential coefficient (growth), [m $h^{-1}$ $h^{ng}$] |
| $K_M$ | kinetic parameter of enzymes, [g $ml^{-1}$] |
| $K_I$ | kinetic parameter of enzymes, [g $ml^{-1}$] |
| $L$ | length of a tubular crystallizer, [cm] |
| $L^*$ | given length of a tubular crystallizer, [cm] |
| $M_{Solvate}$ | molar mass of solid solvate, [g $mol^{-1}$] |
| $M_i$ | molar mass of non-solvated enantiomers, [g $mol^{-1}$] |
| $M_S$ | molar mass of solid phase, [g $mol^{-1}$] |
| $M_3$ | molar mass of solvent, [g $mol^{-1}$] |
| $m_{L,i}$ | mass of component $i$ in liquid phase in crystallizer, [g] |
| $m_{S,i}$ | mass of component $i$ in solid phase in crystallizer, [g] |
| $m_{tot}$ | total mass of liquid phase, [g] |
| $m_i$ | mass of a component, [g] |
| $\dot{m}_i$ | mass flow rate of a component, [g $h^{-1}$] |
| $\dot{m}_{L,i,conv}$ | mass flow rate due to convection in liquid phase, [g $h^{-1}$] |
| $\dot{m}_{L,i,disp}$ | mass flow rate due to dispersion in liquid phase, [g $h^{-1}$] |
| $\dot{m}_{L,i,cryst}$ | mass flow rate due to crystallization in liquid phase, [g $h^{-1}$] |
| $\dot{m}_{S,i,conv}$ | mass flow rate due to convection in solid phase, [g $h^{-1}$] |
| $\dot{m}_{S,i,disp}$ | mass flow rate due to dispersion in solid phase, [g $h^{-1}$] |
| $\dot{m}_{S,i,cryst}$ | mass flow rate due to crystallization in solid phase, [g $h^{-1}$] |
| $\dot{m}_{seeds}$ | mass of seeds per unit time, [g $h^{-1}$] |
| $m_{seeds}$ | mass of seeds, [g] |
| $\widehat{M}_{seeds}$ | normalized seed mass, [-] |
| $\dot{m}_{max}$ | maximum theoretical product mass per unit time, [g $h^{-1}$] |
| $m_{\max}^0$ | maximum theoretical product mass, [g] |
| $m_{i,C}$ | mass of liquid phase in crystallizer, [g] |

| | |
|---|---|
| $m_{i,R}$ | mass of liquid phase in reactor, [g] |
| $m_{i,C}^{S}$ | mass of solid phase in crystallizer, [g] |
| $m_{i}^{S,0}$ | initial mass of solid phase, [g] |
| $m^{0}$ | initial mass of liquid phase, [g] |
| $m_{S}^{0}$ | initial mass of solid phase, [g] |
| $N_i$ | number of particles, [-] |
| $\dot{N}_i$ | flux of particles, [$h^{-1}$] |
| $n_{i,S}$ | particle number density, [$cm^{-3}$] |
| $n^{eff}$ | effective order of crystallization kinetics, [-] |
| $n_g$ | PBM exponent of stirrer speed correlation (growth), [-] |
| $n_{\mu 2}$ | PBM exponent of second moment in correlation for primary nucleation, [-] |
| $n_{\mu 3}$ | PBM exponent of third moment in correlation for secondary nucleation, [-] |
| $OF$ | Objective function |
| $pr$ | Productivity, [g $h^{-1}$ $L^{-1}$] |
| $pu$ | Purity, [-] |
| $R_i$ | radius of particles, [cm] |
| $R^{0}$ | initial radius of particles, [cm] |
| $R_{i,eq}$ | equilibrium radius of particles, [cm] |
| $\hat{R}_i$ | dimensionless radius of a component, [-] |
| $\hat{R}_{i,in}$ | initial dimensionless radius of a component, [-] |
| $R_g$ | universal gas constant, [J $mol^{-1}$ $K^{-1}$] |
| $r_{Rac}$ | rate of racemization, [g $h^{-1}$ $cm^3$] |
| $S_{m,i}$ | mass-fraction based supersaturation, [-] |
| $S_i$ | concentration-based supersaturation, [-] |
| $S^{0}$ | initial supersaturation, [-] |
| $T_{cryst}$ | crystallization temperature, [°C] |
| $t$ | time, [h] |
| $t_{PFTC}$ | residence time of the plug flow tube crystallizer, [h] |
| $t_{dead}$ | dead time or idle time during PC process, [h] |
| $t_{stop}$ | stop time, parameter of SCM, [h] |
| $T$ | Temperature, [°C] |
| $T_{cryst}$ | crystallization temperature, [°C] |

| | |
|---|---|
| $T_{sat}$ | saturation temperature, [°C] |
| $u_L$ | velocity of liquid phase, [cm h$^{-1}$] |
| $u_S$ | velocity of solid phase, [cm h$^{-1}$] |
| $u$ | velocity of both phases ($u_L = u_S$), [cm h$^{-1}$] |
| $u^*$ | given velocity of both phases, [cm h$^{-1}$] |
| $u_{stop}$ | stop velocity, [cm h$^{-1}$] |
| $\dot{V}_L$ | volumetric flow rate of liquid phase, [cm$^3$ h$^{-1}$] |
| $\dot{V}_S$ | volumetric flow rate of solid phase, [cm$^3$ h$^{-1}$] |
| $\dot{V}$ | volumetric flow rate, [cm³ h$^{-1}$] |
| $V_C$ | volume of crystallizer, [cm³] |
| $V_R$ | volume of reactor, [cm³] |
| $V_L$ | volume of liquid phase, [cm³] |
| $V_S$ | volume of solid phase, [cm³] |
| $\hat{V}_{max}$ | maximum solid volume ratio, [-] |
| $w_i$ | mass fraction, [g g $^{-1}$] |
| $w^0$ | initial mass fraction, [g g $^{-1}$] |
| $w_{sat,i}$ | saturation mass fraction, [g g $^{-1}$] |
| $w_{sat}^0$ | initial saturation mass fraction, [g g $^{-1}$] |
| $w_{rac}$ | saturation mass fraction of racemate, [g g $^{-1}$] |
| $w_{ratio}$ | solubility ratio, [-] |
| $X$ | cartesian coordinate, [-] |
| $X_\alpha$ | fraction of $\alpha_{max}$ for estimation of $t_{stop}$, [%] |
| $Y$ | cartesian coordinate, [-] |
| $yi$ | yield, [-] |
| $z$ | spatial coordinate of a tubular crystallizer, [cm] |
| $\hat{z}$ | dimensionless spatial coordinate, [-] |
| $\hat{z}^{stop}$ | dimensionless stop spatial coordinate, [-] |
| **Greek symbols** | |
| $\alpha$ | optical rotation, [deg] |
| $\alpha_{exp}$ | experimental values of optical rotation, [deg] |
| $\alpha_{max}$ | maximum optical rotation reached during batch PC, [deg] |
| $\alpha_{theo}$ | theoretical values of optical rotation simulated with SCM, [deg] |

| | |
|---|---|
| $\rho_S$ | density of solid phase, [g cm$^{-3}$] |
| $\rho_L$ | density of liquid phase, [g cm$^{-3}$] |
| $\rho_{water}$ | density of water, [g cm$^{-3}$] |
| $\hat{\tau}^{stop}$ | dimensionless stop residence time, [-] |
| $\hat{\tau}$ | dimensionless residence time, [-] |
| $\tau$ | residence time, [h] |
| $v_{max}$ | maximum rate achieved by the system, [g h$^{-1}$ mg-enzyme$^{-1}$] |
| **Subscripts** | |
| $i$ | Index for target enantiomer (1), counter enantiomers (2) or solvent (3) |
| $j$ | Index of iteration of number of crystallizers in a cascade |
| $J$ | Number of guesses of $k^{eff}$ for optimization |

# References

Afonso, Carlos A. M., and João G. Crespo. 2004. “Recent Advances in Chiral Resolution through Membrane-Based Approaches.” *Angewandte Chemie International Edition* 43(40):5293–95.

Becker, R., and W. Döring. 1935. “Kinetische Behandlung Der Keimbildung in Übersättigten Dämpfen.” *Annalen Der Physik* 416(8):719–52.

Beckett, A. H. 1991. “Chirality and Its Importance in Drug Development: What Are the Issues?” Pp. 443–46 in *Biochemical Society Transactions*. Vol. 19. Portland Press.

Bhandari, Shashank, Thiane Carneiro, Heike Lorenz, and Andreas Seidel-Morgenstern. 2022. “Shortcut Model for Batch Preferential Crystallization Coupled with Racemization for Conglomerate-Forming Chiral Systems.” *Crystal Growth and Design* 22(7):4094–4104.

Bhandari, Shashank, Heike Lorenz, and Andreas Seidel-Morgenstern. 2024. “Shortcut Model to Evaluate the Performance of Continuous Preferential Crystallization for Conglomerates Forming Chiral Systems.” *Chemical Engineering Science* 299:120539.

Bhushan, Ravi., and Jurgen. Martens. 2010. “Amino Acids : Chromatographic Separation and Enantioresolution.” 322.

Blackmond, Donna G. 2010. “The Origin of Biological Homochirality.” *Cold Spring Harbor Perspectives in Biology* 2(5):a002147.

Bonner, William A. 1995. *CHIRALITY AND LIFE*. Vol. 25. Kluwer Academic Publishers.

Botsaris, Gregory D. 1976. “Secondary Nucleation — A Review.” *Industrial Crystallization* 3–22.

Burton, W. K., N. Cabrera, and F. Frank. 1951. “The Growth of Crystals and the Equilibrium Structure of Their Surfaces.” *Philosophical Transactions of the Royal Society of London. Series A: Mathematical and Physical Sciences* 243(866):299–358.

Cameli, Fabio, Joop H. ter Horst, René R. E. Steendam, Christos Xiouras, and Georgios D. Stefanidis. 2020. “On the Effect of Secondary Nucleation on Deracemization through Temperature Cycles.” *Chemistry – A European Journal* 26(6):1344–54.

Caner, Hava, Efrat Groner, Liron Levy, and Israel Agranat. 2004. “Trends in the Development of Chiral Drugs.” *Drug Discovery Today* 9(3):105–10.

Carneiro, Thiane. 2021. “Advances in Enantioselective Resolution Applying Preferential Crystallization and Enzymantic Racemization.”

Carneiro, Thiane, Shashank Bhandari, Erik Temmel, Heike Lorenz, and Andreas Seidel-

Morgenstern. 2019. “Shortcut Model for Describing Isothermal Batch Preferential Crystallization of Conglomerates and Estimating the Productivity.” *Crystal Growth & Design* 19(9):5189–5203.

Carneiro, Thiane, Katarzyna Wrzosek, Katja Bettenbrock, Heike Lorenz, and Andreas Seidel-Morgenstern. 2020. “Immobilization of an Amino Acid Racemase for Application in Crystallization-based Chiral Resolutions of Asparagine Monohydrate.” *Engineering in Life Sciences* elsc.202000029.

Cascella, Francesca. 2021. “Resolution of Enantiomers of Chiral Compounds Using Crystallization Processes : From Fundamental Studies to Process Development.”

Chaaban, Joussef Hussein, Kim Dam-Johansen, Tommy Skovby, and Søren Kiil. 2013. “Separation of Enantiomers by Continuous Preferential Crystallization: Experimental Realization Using a Coupled Crystallizer Configuration.” *Organic Process Research and Development* 17(8):1010–20.

Chaplin, M. F. (Martin F. .., and C. Bucke. 1990. *Enzyme Technology*. Cambridge [etc.]: Cambridge University Press.

Chen, Jie, Bipul Sarma, James M. B. Evans, and Allan S. Myerson. 2011. “Pharmaceutical Crystallization.” 11:887–95.

Chernov, A. A. 1961. “THE SPIRAL GROWTH OF CRYSTALS.” *Soviet Physics Uspekhi* 4(1):116.

Cintas, Pedro. 2002. “Chirality of Living Systems: A Helping Hand from Crystals and Oligopeptides.” *Angewandte Chemie International Edition* 41(7):1139–45.

collet, André, Marie josèphe Brienne, and Jean Jacques. 1980. “Optical Resolution by Direct Crystallization of Enantiomer Mixtures.” *Chemical Reviews* 80(3):215–30.

Coquerel, Gerard. 2015. “Solubility of Chiral Species as Function of the Enantiomeric Excess.” *Journal of Pharmacy and Pharmacology* 67(6):869–78.

Coquerel, Gérard. 2007. “Preferential Crystallization.” *Topics in Current Chemistry* 269:1–51.

Cox, Geoffrey J. 2005. “Preparative Enantioselective Chromatography.” 330.

Damköhler, Gerhard. 1936. “Einflüsse Der Strömung, Diffusion Und Des Wärmeüberganges Auf Die Leistung von Reaktionsöfen.: I. Allgemeine Gesichtspunkte Für Die Übertragung Eines Chemischen Prozesses Aus Dem Kleinen Ins Große.” *Zeitschrift Für Elektrochemie Und Angewandte Physikalische Chemie* 42(12):846–62.

Danckwerts, P. V. 1953. “Continuous Flow Systems: Distribution of Residence Times.” *Chemical Engineering Science* 2(1):1–13.

Eicke, Matthias. 2016. *Process Strategies for Batch Preferential Crystallization*. Shaker Verlag

Aachen.

Elsner, Martin Peter, Grzegorz Ziomek, and Andreas Seidel-Morgenstern. 2007. “Simultaneous Preferential Crystallization in a Coupled, Batch Operation Mode-Part I: Theoretical Analysis and Optimization.” *Chemical Engineering Science* 62(17):4760–69.

Elsner, Martin Peter, Grzegorz Ziomek, and Andreas Seidel-Morgenstern. 2011. “Simultaneous Preferential Crystallization in a Coupled Batch Operation Mode. Part II: Experimental Study and Model Refinement.” *Chemical Engineering Science* 66(6):1269–84.

Farkas, L. 1927. “Keimbildungsgeschwindigkeit in Übersättigten Dämpfen.” *Zeitschrift Für Physikalische Chemie* 125U(1):236–42.

Fogler, H. Scott. 2006. *Elements of Chemical Reaction Engineering / H. Scott Fogler.* 4th ed. Boston: Prentice Hall PTR.

Frenkel, J. 1939. “A General Theory of Heterophase Fluctuations and Pretransition Phenomena.” *The Journal of Chemical Physics* 7(7):538–47.

Galan, Kamila, Matthias J. Eicke, Martin P. Elsner, Heike Lorenz, and Andreas Seidel-Morgenstern. 2015. “Continuous Preferential Crystallization of Chiral Molecules in Single and Coupled Mixed-Suspension Mixed-Product-Removal Crystallizers.” *Crystal Growth and Design* 15(4):1808–18.

Garside, J., and Tavare N.S. 1984. “Crystallization As Chemical Reaction Engineering.” Pp. 767–83 in. Institute of Chemical Engineers.

Gunawan, Rudiyanto, Irene Fusman, and Richard D. Braatz. 2004. “High Resolution Algorithms for Multidimensional Population Balance Equations.” *AIChE Journal* 50(11):2738–49.

Harriehausen, Isabel, Jonas Bollmann, Thiane Carneiro, Katja Bettenbrock, and Andreas Seidel-Morgenstern. 2021. “Characterization of an Immobilized Amino Acid Racemase for Potential Application in Enantioselective Chromatographic Resolution Processes.” *Catalysts 2021, Vol. 11, Page 726* 11(6):726.

Hein, Jason E., Blessing Huynh Cao, Maarten W. Van Der Meijden, Michel Leeman, and Richard M. Kellogg. 2013. “Resolution of Omeprazole Using Coupled Preferential Crystallization: Efficient Separation of a Nonracemizable Conglomerate Salt under near-Equilibrium Conditions.” *Organic Process Research and Development* 17(6):946–50.

Horn, Annett, Shefali Kumar, Andreas Liese, and Udo Kragl. 2008. “Reactions on Immobilized Biocatalysts.” *Handbook of Heterogeneous Catalysis* 3831–65.

ter Horst, Joop H., Christiane Schmidt, and Joachim Ulrich. 2015. “Fundamentals of Industrial Crystallization.” *Handbook of Crystal Growth: Bulk Crystal Growth: Second Edition* 2:1317–49.

Hulburt, H. M., and S. Katz. 1964. “Some Problems in Particle Technology: A Statistical Mechanical Formulation.” *Chemical Engineering Science* 19(8):555–74.

Inger, George R. 2001. “Scaling Nonequilibrium-Reacting Flows: The Legacy of Gerhard Damköhler.” *Journal of Spacecraft and Rockets* 38(2):185–90.

Intaraboonrod, Kritsada, Isabel Harriehausen, Thiane Carneiro, Andreas Seidel-Morgenstern, Heike Lorenz, and Adrian E. Flood. 2020. “Temperature Cycling Induced Deracemization of Dl-Asparagine Monohydrate with Immobilized Amino Acid Racemase.” *Crystal Growth & Design* 21(1):306–13.

Intaraboonrod, Kritsada, Tharit Lerdwiriyanupap, Marine Hoquante, Gerard Coquerel, and Adrian E. Flood. 2020. “Temperature Cycle Induced Deracemization.” *Mendeleev Communications* 30(4):395–405.

Ishikawa, Hiroki, Kazuma Ban, Naohiro Uemura, Yasushi Yoshida, Takashi Mino, Yoshio Kasashima, and Masami Sakamoto. 2020. “Attrition-Enhanced Deracemization of Axially Chiral Nicotinamides.” *European Journal of Organic Chemistry* 2020(8):1001–5.

J.K. Aronson. 2010. “Meyler’s Side Effects of Analgesics and Anti- Inflammatory Drugs.” *ELSEVIER* 1st Editio:310.

Jacques, Jean., André. Collet, and Samuel H. Wilen. 1994. *Enantiomers, Racemates, and Resolutions*. Malabar FL: Krieger Pub. Co.

Jones, A. G., Jerzy Budz, and J. W. Mullin. 1986. “Crystallization Kinetics of Potassium Sulfate in an MSMPR Agitated Vessel.” *AIChE Journal* 32(12):2002–9.

Jones, Christopher M., and Maurice A. Larson. 1999. “Characterizing Growth-Rate Dispersion of NaNO3 Secondary Nuclei.” *AIChE Journal* 45(10):2128–35.

Juza, M., M. Mazzotti, and M. Morbidelli. 2000. “Simulated Moving-Bed Chromatography and Its Application to Chirotechnology.” *Trends in Biotechnology* 18(3):108–18.

Kadam, Somnath S., Herman J. M. Kramer, and Joop H. Ter Horst. 2011. “Combination of a Single Primary Nucleation Event and Secondary Nucleation in Crystallization Processes.” *Crystal Growth and Design* 11(4):1271–77.

Kashchiev, Dimo. 2000. *Nucleation : Basic Theory with Applications*. Oxford SE - XX-529 p. : ill. ; 24 cm: Butterworth Heinemann Oxford.

Kaspereit, Malte, Subramanian Swernath, and Achim Kienle. 2011. “Evaluation of Competing Process Concepts for the Production of Pure Enantiomers.” *Organic Process Research and Development* 16(2):353–63.

Köllges, Till, and Thomas Vetter. 2018. “Design and Performance Assessment of Continuous

Crystallization Processes Resolving Racemic Conglomerates." *Crystal Growth and Design* 18(3):1686–96.

Koren, B. 1993. "A Robust Upwind Discretization Method for Advection, Diffusion and Source Terms." 117–38.

Kumar, Sanjeev, and D. Ramkrishna. 1997. "On the Solution of Population Balance Equations by Discretization—III. Nucleation, Growth and Aggregation of Particles." *Chemical Engineering Science* 52(24):4659–79.

Kuvadia, Zubin B., and Michael F. Doherty. 2013. "Effect of Structurally Similar Additives on Crystal Habit of Organic Molecular Crystals at Low Supersaturation." *Crystal Growth and Design* 13(4):1412–28.

Von Langermann, Jan, Malte Kaspereit, Mozaffar Shakeri, Heike Lorenz, Martin Hedberg, Matthew J. Jones, Kerstin Larson, Björn Herschend, Robert Arnell, Erik Temmel, Jan Erling Bäckvall, Achim Kienle, and Andreas Seidel-Morgenstern. 2012. "Design of an Integrated Process of Chromatography, Crystallization and Racemization for the Resolution of 2',6'-Pipecoloxylidide (PPX)." *Organic Process Research and Development* 16(2):343–52.

van Leer, B., van Leer, and B. 1985. "Upwind-Difference Methods for Aerodynamic Problems Governed by the Euler Equations." *Ams* 327–36.

Levenspiel, Octave. 1998. *Chemical Reaction Engineering, 3rd Edition | Wiley*.

Levenspiel, Octave. 1999. "Chemical Reaction Engineering." *Industrial & Engineering Chemistry Research* 38(11):4140–43.

LeVeque, Randall J. 2002. "Finite Volume Methods for Hyperbolic Problems." *Finite Volume Methods for Hyperbolic Problems*.

Levilain, Guillaume, and Gérard Coquerel. 2010. "Pitfalls and Rewards of Preferential Crystallization." *CrystEngComm* 12(7):1983–92.

Levilain, Guillaume, Matthias J. Eicke, and Andreas Seidel-Morgenstern. 2012. "Efficient Resolution of Enantiomers by Coupling Preferential Crystallization and Dissolution. Part 1: Experimental Proof of Principle." *Crystal Growth and Design* 12(11):5396–5401.

Li, Wei W., Laura Spix, Saskia C. A. De Reus, Hugo Meekes, Herman J. M. Kramer, Elias Vlieg, and Joop H. Ter Horst. 2016. "Deracemization of a Racemic Compound via Its Conglomerate-Forming Salt Using Temperature Cycling." *Crystal Growth and Design* 16(9):5563–70.

Lim, Young Il, Jean Marc Le Lann, Xuan Mi Meyer, Xavier Joulia, Gibaek Lee, and En Sup Yoon. 2002. "On the Solution of Population Balance Equations (PBE) with Accurate Front Tracking Methods in Practical Crystallization Processes." *Chemical Engineering Science* 57(17):3715–32.

Lorenz, Heike. 2013. “Solubility and Solution Equilibria in Crystallization.” *Crystallization: Basic Concepts and Industrial Applications* 35–74.

Lorenz, Heike, Anett Perlberg, Dragomir Sapoundjiev, Martin P. Elsner, and Andreas Seidel-Morgenstern. 2006. “Crystallization of Enantiomers.” *Chemical Engineering and Processing: Process Intensification* 45(10):863–73.

Lorenz, Heike, Daniel Polenske, and Andreas Seidel-Morgenstern. 2006. “Application of Preferential Crystallization to Resolve Racemic Compounds in a Hybrid Process.” *Chirality* 18(10):828–40.

Lorenz, Heike, and Andreas Seidel-Morgenstern. 2014. “Processes To Separate Enantiomers.” *Angewandte Chemie International Edition* 53(5):1218–50.

Lorenz, Heike, Patrick Sheehan, and Andreas Seidel-Morgenstern. 2001. “Coupling of Simulated Moving Bed Chromatography and Fractional Crystallisation for Efficient Enantioseparation.” *Journal of Chromatography A* 908(1–2):201–14.

Ma, David L., Danesh K. Tafti, and Richard D. Braatz. 2002. “High-Resolution Simulation of Multidimensional Crystal Growth.” *Industrial and Engineering Chemistry Research* 41(25):6217–23.

Mack, C ;, J ; Hoffmann, J ; Sefcik, Horst Ter, J. H. Phase, Gómez Morales, Corin Mack, Johannes Hoffmann, Jan Sefcik, and Joop H. Ter Horst. 2022. “Phase Diagram Determination and Process Development for Continuous Antisolvent Crystallizations.” *Crystals 2022, Vol. 12, Page 1102* 12(8):1102.

Majumder, Aniruddha, and Zoltan K. Nagy. 2017. “A Comparative Study of Coupled Preferential Crystallizers for the Efficient Resolution of Conglomerate-Forming Enantiomers.” *Pharmaceutics* 9(4).

Mateo, Cesar, Jose M. Palomo, Gloria Fernandez-Lorente, Jose M. Guisan, and Roberto Fernandez-Lafuente. 2007. “Improvement of Enzyme Activity, Stability and Selectivity via Immobilization Techniques.” *Enzyme and Microbial Technology* 40(6):1451–63.

Mathworks M. 2017. “MATLAB and Statistics Toolbox Release.”

Meierhenrich, Uwe. 2008a. *Amino Acids and the Asymmetry of Life*. Berlin, Heidelberg: Springer Berlin Heidelberg.

Meierhenrich, Uwe. 2008b. “Origin of Life. Chemical Approach. Edited by Piet Herdewijn and M. Volkan Kisakürek.” *Angewandte Chemie International Edition* 47(44):8342–8342.

Mersmann, Alfons. 2001. *Crystallization Technology Handbook*. Marcel Dekker.

Mueansichai, T., A. E. Flood, T. Stelzer, and J. Ulrich. 2013. “Rate of Sodium Chloride Attrition

Fragment Generation in a Mixed-Suspension Crystallizer." *Crystal Research and Technology* 48(1):38–50.

Mullin, J. W. 2001. "Crystallization: Chpater 5- Nucleation." Pp. 181–215 in *Crystallization*.

Murakami, Hisamichi. 2006. "From Racemates to Single Enantiomers - Chiral Synthetic Drugs over the Last 20 Years." *Topics in Current Chemistry* 269:273–99.

Mwamwitwa, Kissa W., Raphael M. Kaibere, Adam M. Fimbo, Wilber Sabitii, Nyanda E. Ntinginya, Blandina T. Mmbaga, Danstan H. Shewiyo, Morven C. Shearer, Andrew D. Smith, and Eliangiringa A. Kaale. 2020. "A Retrospective Cross-Sectional Study to Determine Chirality Status of Registered Medicines in Tanzania." *Scientific Reports* 10(1):1–11.

Myerson, Allan S. 2002. *Handbook of Industrial Crystallization*. Butterworth-Heinemann.

Negawa, Masakazu, and Fumihiko Shoji. 1992. "Optical Resolution by Simulated Moving-Bed Adsorption Technology." *Journal of Chromatography A* 590(1):113–17.

Nyvlt, Jaroslav, Otakar Sohnel, Marie Matuchova, and Miroslav Broul. 1985. "KINETICS OF INDUSTRIAL CRYSTLLIZATION." *Kinet of Ind Cyst*.

Nyvlt, Jaroslav, and Joachim Ulrich. 1995. *Admixtures in Crystallization*. VCH.

Ohara, Makoto. 1973. *Modeling Crystal Growth Rates from Solution*. edited by R. C. Reid. Englewood Cliffs, N.J: Englewood Cliffs, N.J : Prentice-Hall.

Oketani, Ryusei, Marine Hoquante, Clément Brandel, Pascal Cardinael, and Gérard Coquerel. 2019a. "Resolution of an Atropisomeric Naphthamide by Second-Order Asymmetric Transformation: A Highly Productive Technique." *Organic Process Research and Development* 23(6):1197–1203.

Oketani, Ryusei, Marine Hoquante, Clément Brandel, Pascal Cardinael, and Gérard Coquerel. 2019b. "Resolution of an Atropisomeric Naphthamide by Second-Order Asymmetric Transformation: A Highly Productive Technique." *Organic Process Research and Development* 23(6):1197–1203.

Pasteur, L. 1848. "Mémoire Sur La Relation Qui Peut Exister Entre La Forme Cristalline et La Composition Chimique et Sur La Cause de La Polarisation Rotatoire." *Comptes Rendus Hebdomadaires Des Seances de l' Academie Des Sciences* 26:535–38.

Petruševska-Seebach, Katerina. 2012. *Overcoming Yield Limitations When Resolving Racemates by Combination of Crystallization and, or Chromatography with Racemization*. Docupoint-Verl.

Petruševska-Seebach, Katerina, Andreas Seidel-Morgenstern, and Martin Peter Elsner. 2011. "Preferential Crystallization of l -Asparagine in Water." *Crystal Growth and Design*

11(6):2149–63.

Plumb, Keith. 2005. “Continuous Processing in the Pharmaceutical Industry: Changing the Mind Set.” *Chemical Engineering Research and Design* 83(6):730–38.

Process System Enterprise, Siemens. 2018. “GPROMS.”

Qamar, S., A. Ashfaq, I. Angelov, M. P. Elsner, G. Warnecke, and A. Seidel-Morgenstern. 2008. “Numerical Solutions of Population Balance Models in Preferential Crystallization.” *Chemical Engineering Science* 63(5):1342–52.

Qamar, S., A. Ashfaq, G. Warnecke, I. Angelov, M. P. Elsner, and A. Seidel-Morgenstern. 2007. “Adaptive High-Resolution Schemes for Multidimensional Population Balances in Crystallization Processes.” *Computers & Chemical Engineering* 31(10):1296–1311.

Qamar, S., M. P. Elsner, I. A. Angelov, G. Warnecke, and A. Seidel-Morgenstern. 2006. “A Comparative Study of High Resolution Schemes for Solving Population Balances in Crystallization.” *Computers and Chemical Engineering* 30(6–7):1119–31.

Ramkrishna, Doraiswami. 1985. “The Status of Population Balances.” *Reviews in Chemical Engineering* 3(1):49–95.

Ramkrishna, Doraiswami. 2000. *Population Balances : Theory and Applications to Particulate Systems in Engineering*. Academic Press.

Randolph, Alan D., and Maurice A. Larson. 1988. *Theory of Particulate Processes : Analysis and Techniques of Continuous Crystallization*. Academic Press.

Rauls, M., K. Bartosch, M. Kind, St Kuch, R. Lacmann, and A. Mersmann. 2000. “The Influence of Impurities on Crystallization Kinetics – a Case Study on Ammonium Sulfate.” *Journal of Crystal Growth* 213(1–2):116–28.

Rehage, Hendrik, and Matthias Kind. 2021. “The First Damköhler Number and Its Importance for Characterizing the Influence of Mixing on Competitive Chemical Reactions.” *Chemical Engineering Science* 229:116007.

Rodrigues, Rafael C., Claudia Ortiz, Ángel Berenguer-Murcia, Rodrigo Torres, and Roberto Fernández-Lafuente. 2013. “Modifying Enzyme Activity and Selectivity by Immobilization.” *Chemical Society Reviews* 42(15):6290–6307.

Roozeboom, H. W. Bakhuis. 1899. “Löslichkeit Und Schmelzpunkt Als Kriterien Für Racemische Verbindungen, Pseudoracemische Mischkrystalle Und Inaktive Konglomerate.” *Zeitschrift Für Physikalische Chemie* 28U(1):494–517.

Sangwal, Keshra. 2007. “Additives and Crystallization Processes: From Fundamentals to Applications.” *Additives and Crystallization Processes: From Fundamentals to Applications* 1–435.

Sapoundjiev, Dragomir, Heike Lorenz, and Andreas Seidel-Morgenstern. 2006. “Solubility of Chiral Threonine Species in Water/Ethanol Mixtures.” *Journal of Chemical and Engineering Data* 51(5):1562–66.

Segel, Irwin H. 1975. *Enzyme Kinetics : Behavior and Analysis of Rapid Equilibrium and Steady State Enzyme Systems*. Wiley Classics Library.

Shimura, Toshiaki, and Anthony I. S. Kemp. 2015. “Tetrahedral Plot Diagram: A Geometrical Solution for Quaternary Systems.” *American Mineralogist* 100(11–12):2545–47.

Simon, Melba, Barbara Wood, Steven Ferguson, Brian Glennon, and Roderick C. Jones. 2019. “Diastereomeric Salt Crystallization of Chiral Molecules via Sequential Coupled-Batch Operation.” *AIChE Journal* 65(2):604–16.

Sögütoglu, Leyla Cann, René R. E. Steendam, Hugo Meekes, Elias Vlieg, and Floris P. J. T. Rutjes. 2015. “Viedma Ripening: A Reliable Crystallisation Method to Reach Single Chirality.” *Chemical Society Reviews* 44(19):6723–32.

Srimahaprom, Watcharakarn, and Adrian E. Flood. 2013. “Crystal Growth Rates and Optical Resolution of Dl-Methionine Hydrochloride by Preferential Crystallization from Aqueous Solution.” *Journal of Crystal Growth* 362(1):88–92.

Srisanga, Sukanya, Adrian E. Flood, Shaun C. Galbraith, Supagorn Rugmai, Siriwat Soontaranon, and Joachim Ulrich. 2015. “Crystal Growth Rate Dispersion versus Size-Dependent Crystal Growth: Appropriate Modeling for Crystallization Processes.” *Crystal Growth and Design* 15(5):2330–36.

Steendam, René R. E., and Joop H. Ter Horst. 2017. “Continuous Total Spontaneous Resolution.” *Crystal Growth and Design* 17(8):4428–36.

Steendam, René R. E., and Joop H. Ter Horst. 2018. “Scaling Up Temperature Cycling-Induced Deracemization by Suppressing Nonstereoselective Processes.” *Crystal Growth and Design* 18(5):3008–15.

Subramanian, Ganapathy. 2007. “Chiral Separation Techniques: A Practical Approach.” *Chiral Separation Techniques: A Practical Approach, Third Edition* 1–618.

Suwannasang, K., A. E. Flood, C. Rougeot, and G. Coquerel. 2013. “Using Programmed Heating-Cooling Cycles with Racemization in Solution for Complete Symmetry Breaking of a Conglomerate Forming System.” *Crystal Growth and Design* 13(8):3498–3504.

Temmel, Erik, Matthias J. Eicke, Francesca Cascella, Andreas Seidel-Morgenstern, and Heike Lorenz. 2019. “Resolution of Racemic Guaifenesin Applying a Coupled Preferential Crystallization-Selective Dissolution Process: Rational Process Development.” *Crystal Growth and Design* 19(6):3148–57.

Temmel, Erik, Jonathan Gänsch, Heike Lorenz, and Andreas Seidel-Morgenstern. 2018. "Measurement and Evaluation of the Crystallization Kinetics of l -Asparagine Monohydrate in the Ternary l -/ d -Asparagine/Water System." *Crystal Growth and Design* 18(12):7504–17.

Temmel, Erik, Uwe Müller, Detlef Grawe, Robert Eilers, Heike Lorenz, and Andreas Seidel-Morgenstern. 2012. "Equilibrium Model of a Continuous Crystallization Process for Separation of Substances Exhibiting Solid Solutions." *Chemical Engineering & Technology* 35(6):980–85.

Vetter, Thomas, Christopher L. Burcham, and Michael F. Doherty. 2015. "Separation of Conglomerate Forming Enantiomers Using a Novel Continuous Preferential Crystallization Process." *AIChE Journal* 61(9):2810–23.

Viedma, Cristobal. 2005. "Chiral Symmetry Breaking during Crystallization: Complete Chiral Purity Induced by Nonlinear Autocatalysis and Recycling." *Physical Review Letters* 94(6):065504.

Volmer, M., and A. Weber. 1926. "Keimbildung in Übersättigten Gebilden." *Zeitschrift Für Physikalische Chemie* 119U(1):277–301.

Weller, SOL W. 1994. "Langmuir as Chemical Engineer." *Chemical Engineering Education* 262–64.

Westerterp, K. R., W. P. M. van. Swaaij, A. A. C. M. Beenackers, and H. Kramers. 1984. "Chemical Reactor Design and Operation." 767.

Wood, Barbara, Kevin P. Girard, Christopher S. Polster, and Denise M. Croker. 2019. "Progress to Date in the Design and Operation of Continuous Crystallization Processes for Pharmaceutical Applications." *Organic Process Research and Development* 23(2):122–44.

Wrzosek, Katarzyna, Mariel A. Garcí. Rivera, Katja Bettenbrock, and Andreas Seidel-Morgenstern. 2016. "Racemization of Undesired Enantiomers: Immobilization of Mandelate Racemase and Application in a Fixed Bed Reactor." *Biotechnology Journal* 11(4):453–63.

Würges, Kerstin, Katerina Petruševska-Seebach, Martin P. Elsner, and Stephan Lütz. 2009. "Enzyme-Assisted Physicochemical Enantioseparation Processes-Part III: Overcoming Yield Limitations by Dynamic Kinetic Resolution of Asparagine via Preferential Crystallization and Enzymatic Racemization." *Biotechnology and Bioengineering* 104(6):1235–39.

Xie, Rui, Liang Yin Chu, and Jin Gen Deng. 2008. "Membranes and Membrane Processes for Chiral Resolution." *Chemical Society Reviews* 37(6):1243–63.

Xiouras, Christos, Giuseppe Belletti, Raghunath Venkatramanan, Alison Nordon, Hugo

Meekes, Elias Vlieg, Georgios D. Stefanidis, and Joop H. Ter Horst. 2019. “Toward Continuous Deracemization via Racemic Crystal Transformation Monitored by in Situ Raman Spectroscopy.” *Crystal Growth and Design* 19(10):5858–68.

Xiouras, Christos, Joop H. Ter Horst, Tom Van Gerven, and Georgios D. Stefanidis. 2017. “Coupling Viedma Ripening with Racemic Crystal Transformations: Mechanism of Deracemization.” *Crystal Growth and Design* 17(9):4965–76.

Yagishita, Fumitoshi, Hiroki Ishikawa, Tatsuo Onuki, Shoko Hachiya, Takashi Mino, and Masami Sakamoto. 2012. “Total Spontaneous Resolution by Deracemization of Isoindolinones.” *Angewandte Chemie International Edition* 51(52):13023–25.

Yoshikawa, Masakazu, and Akon Higuchi. 2013. “Enantioselective Membranes.” *Encyclopedia of Membrane Science and Technology* 1–22.

Yoshioka, Ryuzo. 2006. “Racemization, Optical Resolution and Crystallization-Induced Asymmetric Transformation of Amino Acids and Pharmaceutical Intermediates.” *Topics in Current Chemistry* 269:83–132.

Zlokarnik, Marko. 2006. *Scale-Up in Chemical Engineering: Second, Completely Revised and Extended Edition*. Wiley-VCH.